DENSITY DIAGNOSTICS AND INHOMOGENEOUS NON-ISOTHERMAL PLASMAS

BY

YASSEEN MOHAMMED ALMLEAKY

Thesis
submitted to the
University of Glasgow
for the degree of
Ph.D.

Department of Physics and Astronomy,
The University of Glasgow,
Glasgow G12 8QQ.

Sept. 1990

CONTENTS Page

ACKNOWLEDGEMENTS

The work of this thesis was carried out while the author was a research student in the Department of Physics and Astronomy, University of Glasgow. I deeply express my thanks to the staff and students of this department, past and present, who have made the period of my research both interesting and enjoyable. I would also like to thank them for their friendly co-operation, and for making this such a pleasing and warm department in which to work. In particular, of course, I would like to thank my supervisor, John Brown, for his excellent supervision of this research. I am indebted to him for his guidance, friendship, encouragement and invaluable suggestions throughout the course of this work. I also wish to thank him for his help in supporting me with the necessary funds to attend some conferences and summer schools.

It is my pleasure to acknowledge generous cooperation of other members of the Department. I am very much grateful to the 'Prof.' (Prof. P.A.Sweet) for his long and helpful discussions, which assisted me in my understanding of both the general and the specific physics relevant to the work contained herein; his encouragement was also much appreciated; I would like to thank my colleagues Dr David Alexander and Mr. Yan Chao Ge with whom I shared a multi-cultural and Multilingual office, for their support and friendship; I am greatly obliged to David, particularly for his unlimited help in correcting my English, his careful reading of this thesis and for many useful suggestions and comments; Yan Chao is much appreciated for allowing me to play badminton, and for teaching me some of the less common Chinese words; to Dr. Bhola Dwivedi (of the Banaras Hindu University, India) for his helpful comments and suggestions. I would also like to thank him for his careful reading of this thesis; Mr. Mahroos Yasseen (Strathclyde University) for helping me to understand some aspects of laboratory plasmas and for the many beneficial discussions regarding plasma spectroscopy; Mr. Hassan Basurah for discussions and suggestions; Drs. Alec MacKinnon, Alan Thompson, and Abdulah A. Abdulah (Department of Mathematics) for their comments and useful prescriptions for handling the computer system and to making it a more useful and enjoyable machine; to

Dr. John Simmons who introduced me to the trials and tribulations of statistics.

I would like to thank the Saudi Educational Bureau (London) for their continuous care and support during my stay in Scotland, and to King Abdul Aziz University (K.A.A.U), Jeddah, Saudia Arabia for providing the necessary funding.

Finally, thanks to my family; to my sons Alla, Hamzah, and Ahmed who, unintentionally, used to wake me in the middle of the night to do some typing (after answering their needs), and for their tolerance for me not spending as much time as I would have liked with them in their most important games; to my wife Amal whose care, support, help in typing some parts of this thesis and taking care of the children and cooking made this thesis possible.

YASSEEN ALMLEAKY

Summary

Many astrophysical plasmas, such as are found in the sun, nebulae and, supernova remnants etc are often analysed spectroscopically assuming in a first approximation that they are homogeneous in nature. However, when several different diagnostics are applied, different plasma parameters, e.g. electron density and temperature, are usually inferred from each diagnostic. This is consistent with imaged observations of the solar atmosphere, for instance, which show that it is, in fact, highly inhomogeneous, and of non-isothermal structure, so that a range of temperatures and densities contribute to the line intensities used in the spectroscopy. Such inhomogeneity can severely affect accurate determination of plasma parameters, such as electron densities.

In this thesis, Chapters 1 and 2 are designed to introduce and review the relevant topics considered in the later Chapters. Chapter 1 considers the use of solar plasma spectroscopy for the determination of the electron temperature and density in the solar atmosphere, discussing the different techniques developed for this purpose. Our discussion is restricted to plasma diagnostics inferred from the high temperature solar spectrum, which produces lines mainly in the UV, EUV, and X-ray regions of the electromagnetic spectrum. The necessary atomic physics involved, which is closely related to solar physics diagnostics, is also discussed in detail. In Chapter 2 we review the present status of observational knowledge of the solar atmosphere at UV, EUV and X-ray wavelengths, paying special attention to plasma electron density inhomogeneities.

The main body of this thesis is contained in Chapters 3-6. In Chapter 3, we present a simple, but accurate, analytical, representation which describes line ratios as a function of electron density. This representation is found to lead to an extremely good representation of actual line ratio curves, obtained by numerical methods that require much theoretical effort and very accurate atomic data. This representation is shown to be an excellent method for electron density determination in solar plasmas, and to provide a more flexible treatment of the effect of plasma inhomogeneities on density sensitive line

ratios.

Chapter 4 discusses the problem of interpreting density sensitive line strengths from an isothermal plasma of inhomogeneous density. We show that the problem can be expressed in terms of deriving an emission measure function $\zeta(n_e)$ per unit density from a set of line strengths and that any particular line ratio yields a spectroscopic 'mean density' $\langle n_e \rangle$. The value of $\langle n_e \rangle$ will differ for different line pairs, and differ from both the volumetric mean $\bar{n}$ and emissivity mean $\tilde{n}$ unless the plasma is homogeneous. For a single line ratio and total emission measure, the homogeneous solution $n_e(\underline{r})=\langle n_e \rangle$ yields the minimum possible plasma volume which is found to fall below the true plasma volume to an extent which increases with the inhomogeneity of the real plasma. This result, explains, in terms of plasma inhomogeneity, the small filling factors commonly found when emitting volumes, inferred using $\langle n_e \rangle$ together with the total emission measure, are compared with spatially resolved total volumes.

In Chapter 5 the problem of interpreting densities in inhomogeneous non-isothermal plasmas from density sensitive line ratios is discussed. It is shown how the concepts of emission measure differential in density $\zeta(n_e)$ and emission measure differential in temperature $\xi(T)$ can be generalised to analyse arbitrary plasmas. In the special case (pressure stratification) where surfaces of constant temperature S_T and of constant density S_n coincide it is proven that it is possible in principle, if $\xi(T)$ is known from resonance lines, to derive information about the density (or pressure) distribution as a function of temperature, i.e. $n_e(T)$, using density sensitive lines.

It is then investigated whether and when the predicted line strengths of a set of sources with different $n_e(T)$ but with the same $\xi(T)$ would in practice be distinguishable using measurements of density sensitive lines, for the empirical model $n_e(T) \propto n_0 T^{-\delta}$. It is found that the inferred value of δ and of the base density n_0 from two density sensitive line ratios is sensitive to the data, thus demonstrating the possibility of deducing $n_e(T)$ for the plasma in question. The approach is tested on data from an emission region observed above the limb of the quiet sun, using the only two line ratios for ions in a temperature

range $2x10^5$-$1.6x10^6$ K for which the atomic parameters were available. The values of δ and the electron pressure (base density) obtained were in a good agreement with the theoretical model of the quiet sun transition region. This technique can be extended, and the model form for $n_e(T)$ tested, by comparing for consistency the value of δ and n_0 obtained from three or more ratios.

In Chapter 6 we discuss another reason for deducing incorrect electron densities in the solar atmosphere, namely the noise in the observed line intensities and in the atomic data. The resultant bias in the estimated densities, as well as the confidence interval, is determined for some examples. A fairly brief discussion is given of how the noise on line ratios can affect the estimated densities and, therefore, the required accuracy for obtaining reasonable values of n_e.

Finally, Chapter 7 discusses possible future work inspired by, or related to, the considerations of this thesis. In particular, the investigation of the effect of the plasma inhomogeneity on different models of the solar atmosphere as well as on different solar phenomena is considered. In addition, the effect of noise on the different atomic parameters present in our representation (Chapter 3), and a comparison with that of the line ratio's are shown to be important.

Some parts of this thesis have already been published or submitted for publication and others have appeared in different conferences. The contents of Chapter 3 and 4 have been published in the Astronomy and Astrophysics (1989), Chapter 5 has been submitted to the above journal, as well as appeared in the Royal Astronomical Society meeting at the University of Glasgow, 1990 April 4-6 and in the COSPAR Symposium No. 9 at The Hague, Netherlands, 27-29 June 1990. Chapter 6 is currently being developed for publication .

CHAPTER 1

SOLAR PLASMA SPECTROSCOPIC DIAGNOSTICS

1.1 Solar Spectroscopy

1.1.1 Introduction

Solar spectroscopy is a field of study that covers a wide area, of physics including investigations of atomic structure and basic plasma physics diagnostics as well as the physics of the sun itself. During the first quarter of this century, solar spectroscopy occupied a central role in physical research. The high quality of this field improved dramatically after World War II, with the advent of space research, and some of the most interesting spectroscopic and plasma diagnostic results were achieved in the 1950's and 60's. In this chapter we will review some spectroscopic concepts and atomic results which are closely related to solar physics plasma diagnostics. The discussion will deal merely with the final results of the extensive work carried out on the theoretical determinations of energy levels, transition probabilities, and calculations of excitation and ionisation rate coefficients. In other words we shall discuss line intensities, their formations and interpretations and their changes as a result of the properties of the emitting plasma. Different kinds of spectral lines observed in the sun will be mentioned and defined later in the glossary.

A large amount of literature exists on solar spectroscopy and plasma diagnostics. Recent examples include Gabriel and Jordan (1969, 1972), Culhane and Acton (1974), Dupree (1978), McWhirter (1978), Jordan (1979), Dere and Mason (1981), Feldman (1981), Gabriel and Mason (1982), McWhirer and Summers (1984), and Doschek (1985, 1988)

A wealth of information, providing diagnostic tools for determining physical parameters, crucial to the understanding of the physics of the solar atmosphere, is obtained by investigating the radiation emitted. The radiation, emitted from different temperature regimes (or different depths for a stratified structure) in the solar atmosphere, has various forms which may be distinguished according to their wavelength (or energy). The spectrum ranges from radio waves of very long wavelength (low energy) to X-ray

and gamma rays at very short wavelengths (high energy). In between fall infrared (IR), visible UV and EUV (Extreme Ultraviolet) light. Table 1.1 summarises the different wavelengths and energies available for observations. Although we shall be concerned mainly with the solar plasma, the results may also be applied to other types of plasma with a similar temperature and density, and for which the processes of ionization, recombination, excitation and deexcitation are similar.

In this thesis we shall restrict our discussion to the interpretation of optically thin spectral line intensities obtained from the so-called high temperature solar spectrum (HTSS), this spectrum being produced in the upper part of the chromosphere, the transition region and the corona. These regions span a temperature range from 2×10^4 K to about 10×10^6 K. The high temperature regions of the solar atmosphere produce interesting spectra mostly at wavelengths shorter than visible, i.e. UV, EUV, and X-ray wavelengths. These spectra are usually absorbed by the atmosphere of the earth making it difficult to study from ground based instruments, and the investigation of these spectra could not begin in earnest before the advent of solar space research. Since the early to mid 1960s X-ray and UV spectrometers and spectrographs have been flown on rockets and unmanned and manned spacecraft, obtaining a large amount of data and providing interesting spectroscopic and plasma diagnostic results. High temperature solar spectroscopy is, therefore, a relatively young field. Because of its proximity, the high temperature solar atmosphere is the only astrophysical plasma source that can be studied in great detail both because it can be to some extent spatially resolved, and because the high photon flux allows very high spectral resolution. The main source for our understanding of stellar atmospheres and even of low density collisionally excited plasmas, such as supernovae, and their remnants is based on our knowledge concerning the plasma radiation processes in the solar atmosphere. Although some of these processes can be studied by high resolution images of the atmosphere, much of our knowledge concerning temperature, density and dynamics of different regions of the solar atmosphere is obtainable through the technique of high resolution spectroscopy in UV, EUV, and X-ray spectral regions. In addition, this part of the solar spectrum has shed

Table 1 The Spectrum ranges

Band	Wavelength range (Å)	Energy range (eV)
Radio	$\lambda \geq 10^7$Å	0.00124 eV $\geq$ E
Infrared (IR)	10^6Å > $\lambda \geq$7500Å	1.65eV $\geq$ E > 0.00124eV
Visible	7500Å > $\lambda \geq$3000Å	4.13 eV $\geq$ E > 1.65 eV
UV	3000Å > $\lambda \geq$1500Å	8.24 eV $\geq$ E > 4.13 eV
EUV	1500Å > $\lambda \geq$100Å	.124 keV $\geq$ E > 8.24 eV
Soft X-ray	100Å > $\lambda \geq$1Å	12.4 keV $\geq$ E > 0.124 keV
Hard X-ray	1Å > $\lambda \geq$0.025Å	500 keV $\geq$ E > 12.4 keV
Gamma-ray	.025Å > λ	E > 500 keV

light on certain problems of atomic physics and has been useful in understanding laboratory plasma spectra, such as those obtained from laser produced and tokamak plasmas.

1.1.2 The UV, EUV, and X-ray spectrum

It is well known that visible spectroscopy is very important for optical astronomy. However, it is obvious that the much larger spectral range covered by the UV down to X-rays should be far more fruitful for diagnosing High Temperature Plasmas (HTP) simply because of the much larger spectral range involved. Most of the plasma diagnostics for these different spectral regions have been determined over the last three decades, with solar spectra providing the primary data base. The application of these diagnostics to non-solar spectra is enormous, and already considerable work has been done with spectra from the International Ultraviolet Explorer (IUE). By only considering short wavelengths, we will be restricted to data obtained from space observations. In what follows we will divide the spectral range into several sections according to the typical wavelength ranges covered by different spectrometers. Due to properties of materials used in the construction of short wavelength instruments and other similar considerations, the same wavelength divisions will be approximately maintained in future space experiments. Therefore, it is preferable to find lines that fall in one or another of these ranges because of the problems involved in applying diagnostics to spectra obtained from different instruments.

The spectral range between 2000-3000 Å contains many lines, formed mostly in the photosphere and cooler parts of the chromosphere. Some of the more important lines for both solar and stellar atmospheres are the Mg II h and k lines near 2800 Å. These lines have been investigated in detail by Doschek (1985) and Feldman and Doschek (1977). This wavelength range also contains other interesting chromospheric lines such as the C II lines and the Si II lines near 2325 Å and 2340 Å respectively which have been used to determine electron density in stars with atmospheres less dense than that of the Sun (Stencel et al 1981). A small number of ions which are of particular interest to high

temperature plasma diagnostics are the coronal forbidden lines such as Fe IX , Fe XI-Fe XIII, Ni XIII-Ni XV and some silicon lines. Atomic data have been calculated for Fe XII by Flower (1977) showing that the lines of this ion can be used as an electron density diagnostic.

The spectral range between 1100-2000 Å have been investigated in great detail since the start of space-borne observations particularly since the data from Skylab became available, after 1973. This range is very important for the lower transition region plasma and also for certain astrophysical sources. Several wavelength lists whithin this range have been published by many authors such as Burton and Ridgely (1970) who published the first extensive wavelength list with sufficient accuracy obtained from the Sun; the list included a number of new identifications of intersystem and forbidden transitions, Doschek et al (1976), Sandlin et al (1977), Feldman and Doschek (1977) who published lists of lines recorded above an active region, and a list of lines recorded during a flare have been published by Cohen et al (1978). The most outstanding lines in this region are the 1548 and 1550 Å lines of C IV. There are also a number of strong lines that appear with significant intensity such as N V, AL III and Si IV. These lines show a special importance in determining the differential emission measure (cf section 1.5) in temperature in the lower transition region where they have been formed (Feldman 1981). A number of intersystem lines which are important for the lower density plasma diagnostics (10^8 - 10^{13} cm^{-3}), e.g. N III, N IV, O III, Si III, S IV and S V have been identified in this range. Ions of Beryllium isoelectronic sequences, in particular, C III and O V, have also proved to be a rich resource for studying this region. C III has been extensively studied in the quiet sun and active regions. Work on this ion has been reviewed by Gabriel and Jordan (1972), Dupree (1978) and Jordan (1979), and Doschek (1985). The other ion in the Beryllium isoelectronic sequence that is useful for density diagnostics is OV. Atomic calculations for this ion have been carried out by Malinovsky (1975). However, more recently, interest has focused on O IV transitions that fall around 1401 Å, a more detailed explanation concerning this ion and its utilities in electron density diagnostics will be discussed later in Chapter 3. The intensity ratio of the spectral lines of

this ion within the multiplet or the ratio of one of these lines to an allowed line, are very useful as a density diagnostic tool, as will be seen shortly.

The importance of many of these lines arises because of the small radiative decay rate (cf. next section). Some of these lines can be utilised in one of two ways: (i) by taking the strongest intersystem line and comparing it with an allowed line formed at a similar temperature, e.g. O IV and S IV can be compared to one of the Si IV lines (this method can serve as a useful technique for the electron density determination Feldman et al (1977), and will be discussed in Section 2.3.2). (ii) by comparing lines within each multiplet (Flower and Nussbaumer 1975c), since the intensity ratios within the multiplet are sensitive to a relatively narrow range of densities. The range 1100-2000 Å also contains some coronal forbidden lines such as Si VIII, Fe IX-Fe XIII. In addition to these lines, some forbidden high temperature flare ion lines, Fe XVII, Fe XIX and Fe XXI, are located in this wavelength range.

The wavelength range 170-1100 Å contains very important lines for the HTP diagnostics. This region contains intense spectral lines spanning a very wide range of temperatures from the lower transition region, e.g., the resonance lines He II (304 Å), O IV (554 Å), O V (629 Å) and Ne VII (465 Å), up to flare temperatures, e.g., the lithium like lines of Fe XXIV at 192 and 225 Å, the intersystem line Fe XXIII (263 Å), the Ca XVII (193 Å), and Ca XVI at (209 Å) and (225 Å). There also exist many other strong lines that are useful for coronal diagnostics in this range, e.g., Mg IX (368 Å), Fe XV (284 Å) and Fe XVI (365 Å). The outstanding chromospheric line in this range is He I (584 Å). Many authors have published different lists of emission lines in this region. Behring et al (1976) have published one of the most accurate emission line lists obtained in the 160-770 Å range, while Dere et al (1979) have carried out an extensive study for the range 170-630 Å; this study includes a group of very strong coronal lines due to Fe VIII-Fe XIII, Ni XI-Ni XVII and other different lines of the beryllium, boron, carbon, and nitrogen isoelectronic sequences. There are many other lists of interesting lines in this range, but because of space limitation they will not be considered in detail here.

The spectral range 30-170 Å contains lines important for flare physics. This EUV region has so far been insufficiently explored with high spectral resolution instrumentation. This very interesting group of resonance lines are due to Fe XVIII-Fe XXIII, the Fe XVIII lines appearing with a significant intensity during solar activity (Behring et al 1972-it should be mentioned that this reference also contains the most accurate wavelengths). There are also weaker lines from Ca and Ni ions, with similar transitions to iron's. Extensive theoretical work has been done in calculating collision strengths and radiative decay rates for the above mentioned ions. Calculating the spectra is now possible, with a fair degree of accuracy.

Finally we discuss the wavelength range between about 1.5-30 Å. This range is dominated by two types of lines. One of them includes transitions that occur in He-like ions, which are a good density diagnostic for solar plasmas (Gabriel and Jordan 1969) as will be shown in section 2.4.2., H-like ions, and ions in lower ionisation stages, which are very important for the determination of plasma properties. The second type include transitions in Ca, Fe and Ni ions. The most intense lines of this type belong to Fe ions particularly for lines which fall between 10-20 Å. These lines can also be used for the determination of plasma properties such as emission measures. They are not very useful for the electron density determination in solar plasmas.

1.2 Theory of Spectral Line Formation.

The main aim of spectroscopists is to determine characteristics of and physical conditions within an emitting plasma. Different parameters may be inferred from line intensities. These include the chemical abundance of the elements, the density, temperature and velocity fields and size of the emitting volume in the gas. Such parameters must be evaluated in order to understand fully the mass flow and energy balance in the solar atmosphere. To interpret the spectrum of the emission lines in the solar UV, EUV and X-ray, it is necessary to combine both theoretical atomic physics, the production of analogous spectra in laboratory experiments, and an understanding of the physical conditions likely to be present in the solar atmosphere. In this chapter we focus

on the determination of temperature (Section 3) and density (Section 4) from line intensity ratios.

The purpose of this Section is to explain the principle of the formation of spectral lines, their properties and how we utilise them to diagnose solar plasmas. It is not designed to be an extensive review, since a complete explanation of different lines formed in different plasmas with the involved atomic data would need a separate chapter, but rather it will concentrate on the main points explaining line formation in certain plasmas with the required atomic data.

The identification of astrophysical spectral lines in the visible region has been dealt with, for most sources, many years ago and most recently the concentration has been on the EUV and X-ray regions or, at the other end of the spectrum, with radio wavelengths. Even below 2000 Å the progress over the past two decades has been so rapid that the strongest lines in solar and stellar spectra have been identified. Most of our discussion will be mainly related to solar emission lines which have clearly become a specialised technique for studying spectra of distinctive parts of the solar atmosphere, such as active regions, sunspots, and flares.

Interpretation of the intensities of emission and absorption lines observed in astrophysical sources require a wide variety of accurate atomic data. Accurate collision strengths, radiative transition probabilities, and wavelengths are needed for allowed and forbidden transitions for almost all the ions under consideration. For some of the solar observations, which are of very high quality, accuracies of 20% or even better in atomic data are desirable. Errors on line ratios and atomic data, and the effect of these noises on the inferred densities will be discussed in Chapter 6. Spontaneous radiative transition probabilities are essential in interpreting the intensities of emission lines. However, their calculation is a fairly simple process and consequently good agreement is usually found with experiment. The cross-section for collisional excitation by electrons is the most important atomic parameter. During the last two decades there has been a dramatic increase in the high quality electron collision excitation data available for astrophysical

applications. This is largely due to the development of sophisticated, computer codes, which have as their objective the calculation of rate coefficients with accuracies better than ±20%, sometimes considerably better. Many theoretical methods used for electron collisional excitation were reviewed by Seaton (1975) and more recently by Henry(1981). We attempt here to show how the atomic data are used to calculate spectral line intensities and how this information is related to properties of the emitting gas, such as temperature, density, and atmospheric structure and dynamics.

It was only during the last few decades that the interpretation of the line intensities, although straightforward to measure, has become well understood.

In our discussion we should note that most of the plasmas depart significantly from local thermodynamic equilibrium (LTE), are often known as non-LTE plasmas. However, it is usually better to refer to them as low density plasmas. Also we consider an optically thin plasma so that photoexcitation and photoionisation are negligible and that the electrons are the only particles capable of collisionally exciting the ions. For most cases discussed here, the dominant line formation process for allowed (electric dipole) and intersystem transitions is electron collisional excitation.

For optically thin plasmas the line emission I_{ij} (ergs cm^{-3} sec^{-1} sr^{-1}) formed in a volume $\Delta V=1$ cm^3 is given by

$$I_{ij} = \frac{1}{4\pi} A_{ji} \, h\nu_{ij} \, n_j \qquad (1.1)$$

$$= \frac{1}{4\pi} A_{ji} \, E_{ij} \, n_j \qquad (1.2)$$

where E_{ij} is the energy of the transition between upper level j and lower level i, A_{ji} is the spontaneous radiative transition probability, n_j is the number density of the upper emitting level. The flux F_{ij} (erg cm^{-2} sec^{-1}) at the earth in an optically thin spectral line is then given by

$$F_{ij} = \frac{E_{ij}}{4\pi R^2} A_{ji} \int_{\Delta V} n_j \, dV \qquad (1.3)$$

where R is the earth-to-object distance and the integral is over the volume of the plasma in which the line is formed. The number density (n_j) can be found by using detailed balance between excitation and radiative processes alone, neglecting ionisation and recombination processes since collisional excitation and radiative decay within an ion is much faster than ionisation and recombination time scale, viz.

$$n_j\left(\sum_{i<j} A_{ji} + n_e \sum_{i>j} C^e_{ji} + n_e \sum_{i<j} C^d_{ji}\right) = n_e \sum_{i<j} n_i C^e_{ij} + n_e \sum_{i>j} n_i C^d_{ij} + \sum_{i>j} n_i A_{ij} \qquad (1.4)$$

where C^e is the collisional excitation and C^d is the collisional deexcitation rate coefficients ($cm^3\ sec^{-1}$) for electron collisions. Collisional excitation and deexcitation rates are related simply, so that if one is known the other can easily be derived from

$$C^d_{ji} = C^e_{ij} \frac{\omega_i}{\omega_j} \exp\left(E_{ij} / kT\right) \qquad (1.5)$$

In equation (1.5) ω_i and ω_j are the statistical weight of the lower and of the upper levels respectively, T is the electron temperature, and k is Boltzmann's constant. The electron collisional excitation rate is obtained by integrating the collision cross section σ_{ij} over a Maxwellian velocity distribution, as will be seen in the glossary. Usually the collisional strength Ω_{ij}, a dimensionless quantity, is used in preference to the cross section

$$\sigma_{ij} = \frac{1}{K_i^2} \frac{\Omega_{ij}}{\omega_i} \pi a_0^2 \qquad (1.6)$$

where a_0 is Bohr radius, and K_i^2 is the energy of the incident electron. Assuming the collision strength to be independent of incident electron energy, the collisional rate is then

$$C^e_{ij} = \kappa \frac{\Omega_{ij}}{T^{1/2}\omega_i} \exp\left(-\frac{E_{ij}}{kT}\right) \qquad (1.7)$$

where κ= constant. When C_{ij} in $cm^3\ sec^{-1}$, E_{ij} in eV, and T is in Kelvin degrees we have $\kappa = 8.6 \times 10^{-6}$.

By considering allowed transitions, we find that the excited levels are populated by electron collisions and depopulated by radiative decay. The populations of the excited levels are negligible compared to that of the ground level. Then the statistical equilibrium equations can be solved as a two-level system for each transition, viz

$$n_e\, n_i\, C^e_{ij} = n_j\, A_{ji} \tag{1.8}$$

and

$$n_i = n_{ion} \tag{1.9}$$

By combining equations (1.3) and (1.8) we get

$$F_{ij} = \frac{E_{ij}}{4\pi R^2} \int_{\Delta V} n_e\, n_{ion}\, C^e_{ij}\, dV \tag{1.10}$$

It is necessary to determine n_j in order to evaluate equation (1.3). This quantity is conveniently expressed as

$$n_j = \frac{n_j}{n_{ion}} \frac{n_{ion}}{n_{el}} \frac{n_{el}}{n_H} \frac{n_H}{n_e}\, n_e \tag{1.11}$$

where n_{ion} is the ion number density under consideration, n_{el} is the element number density, n_H is the hydrogen number density and n_e is the electron number density.

The ratio n_j/n_{ion} is the population of level j relative to the total number density of the ion, and is a function of the electron density and temperature.

The ratio $n_{ion}/n_{el} = f(T)$, the ionisation ratio of the ion, has been calculated by several authors assuming ionisation equilibrium for all abundant elements in the solar atmosphere, e.g., Arnaud et al (1985), Jordan (1969, 1970), Jacobs et al (1977a, 1977b, 1979, and 1980) and it is a function of electron temperature only.

The quantity $n_{el}/n_H = A_H$ is the element abundance relative to the hydrogen. This ratio is well known for most of the abundant elements in the solar atmosphere, and has

been reviewed by many authors, e.g., Pagel (1973), Lambert (1978) and Lambert and Luck (1978).

In regions of the solar atmosphere where hydrogen is mostly ionised, the hydrogen density relative to the electron density, corresponding to a relative helium abundance of 0.1, is $n_H/n_e=0.8$.

For a simple case, with no metastable levels and the ion population almost completely in the ground state, combining equations (1.10) and (1.11) the flux can also be written approximately as,

$$F_{ij} = \frac{0.8}{4\pi R^2} E_{ij} A_H \int_{\Delta V} C^e_{ij} n_e^2 f(T) dV \qquad (1.12)$$

In many analysis of solar and stellar spectra ionisation equilibrium is assumed, and if the volume contains an isothermal plasma then equation (1.12) can be rewritten as

$$F_{ij} = \frac{0.8}{4\pi R^2} E_{ij} A_H C^e_{ij} f(T) \int_{\Delta V} n_e^2 dV \qquad (1.13)$$

Here the square of the density integrated over the volume, is called the volume emission measure which is a property of the solar atmosphere. For optically thin lines it is desirable to determine this property from spectral line intensities. However, the emission measure is not a physical quantity in itself, and it is thus desirable also to determine independently either the density or the volume of the plasma. By determining one of these quantities, the emission measure then gives the other. This property will be investigated further in Section 1.5.

Implicit in the above discussion is the assumption that the emitting volume is homogeneous and isothermal. This assumption is not realistic for most of the plasmas of interest. We will discuss this in more detail in chapters 4 and 5.

1.3.Electron Temperature Determination

Before we explain the basic method of electron temperature determination one should keep in mind that most often the plasma along the line of sight is inhomogeneous

and non-isothermal. Therefore the contribution to line intensities come from a range of temperatures and densities. In addition, determining temperature in a particular solar region is meaningless unless the problem has been defined more precisely. For example, consider the case of temperature in a flaring regions. It is well known from observations that flaring regions are bright in almost any spectral line emitted from the first degree of ionisation up to and including helium-like iron (Fe XXV), the highest degree of ionisation observed with significant intensity. A better way of stating the problem is to define the temperature distribution as a function of emission measure (Craig and Brown 1976 and 1986). The scope of this problem will be the main thrust of Chapter 5. However, we will consider firstly the commonly used methods for determining plasma electron temperature in an isothermal plasma.

The most commonly used method for the determination of electron temperature in a plasma is by using two optically thin allowed lines from the same ion with significantly different excitation energies. Consider an isothermal plasma of electron density n_e and volume V. The flux ratio of two lines originating in level 3 and 2 and decaying to the lower level 1, is given by

$$\frac{F_{13}}{F_{12}} = \frac{E_{13}}{E_{12}} \cdot \frac{C^e_{13}}{C^e_{12}} \qquad (1.\ 14)$$

where the quantities have been detailed above. Using the expressions for the collisional excitation rate (Equation 1.7), we obtain

$$\frac{F_{13}}{F_{12}} = \frac{E_{13}}{E_{12}} \frac{\Omega_{13}}{\Omega_{12}} \exp\left(\frac{E_{13} - E_{12}}{kT}\right) \qquad (1.\ 15)$$

It is clear from this equation that the flux ratio is density independent, and that the temperature dependence is almost entirely given by the exponential term, particularly when $(E_{13} - E_{12})/kT >> 1$. In deriving Equation (1.15) we assumed an isothermal plasma of homogeneous density. However, in most physically realistic situations, the solar atmosphere is inhomogeneous in density and multithermal. For this reason the excitation rate inside the integral of equation (1.10) cannot be removed, and the flux ratio depends

on the atmospheric structure in addition to the temperature. A disadvantage of this method is that the large wavelength separation of these lines, a consequence of the requirement $(E_{13} - E_{12})/kT >> 1$, makes temperature determination very difficult in practice. A further drawback is that most of the ions produce lines in EUV that are formed over a narrow range of temperature.

A second and rather elegant method for electron temperature determination in low-density high temperature plasmas was developed by different authors, e.g. Gabriel and Jordan (1972). This method uses the ratios of satellite lines, formed only by dielectronic recombination, to resonance lines of helium-like and hydrogen-like ions, formed by electron collisional excitation. These lines are important features in X-ray spectra of flares, and they fall in the wavelength region between 1.6 and 30 Å. The flux ratio of the dielectronic line (F_D) to the resonance line (F_R) is given by

$$\frac{F_D}{F_R} = \frac{E_D}{E_R}\frac{\alpha_D^d}{C_R^e} \qquad (1.16)$$

where α_D^d ($cm^3\ s^{-1}$) is the dielectronic rate coefficient, and E_D and E_R are the energies of the dielectronic and the resonance lines. In X-ray regions, these energies are usually almost equal in value. However, the flux ratio is proportional to the ratio of the dielectronic recombination rate to the electron collisional excitation rate. By using the expressions for α_D^d and C_R^e given by Gabriel and Jordan (1972) , Equation (1.16) can be rewritten as

$$\frac{F_D}{F_R} = \mu\frac{\{\exp(E_R - E_{nj})/kT\}}{T} \qquad (1.17)$$

where μ is a constant containing atomic factors. It is clear from this equation that the flux ratio is primarily sensitive to electron temperature, proportional to 1/T. It has been shown that this technique is very useful for flare plasmas. Different authors have extended the theory to include different satellites, e.g. Bely-Dubau et al 1979. Doschek et al (1981) used dielectronic recombination and innershell excitation for Fe XXII and Fe XXI for the derivation of electron temperature in flare plasmas.

1.4 Electron Density Diagnostics

The electron density is an essential parameter in theoretical models that describe solar phenomena. The emission measure (cf. Chapter 1.5) can be utilised in deriving electron density, by assuming an emitting volume. This volume is estimated from spatially resolved images. This assumption is questionable even with high resolution images, as we will see in Section 1.4.2. The importance of determining electron densities has led to the development of electron density techniques that are independent of assumptions about the size of the emitting region. The different methods of electron density determination are discussed below in more detail with some specific examples.

1.4.1 The effect of metastable levels:-

Because the upper levels of some intersystem and forbidden lines are metastable levels, in which the collisional deexcitation processes are comparable to the radiative decay rates or long lifetime levels, then the population of these levels become comparable with that of the ground level. The essence of the metastable level is that it begin to build up to a much higher population than similar levels with an allowed decay, and thus provides a density diagnostic line ratio. In more physical terms, these levels having an excess population begins to transfer to other excited states rather than decaying to the ground level, and this affects their populations. The intensities of transitions from the metastable level become weak compared to the intensities from other levels in the excited configurations.

Emission lines can be classified into three groups, according to the way in which their upper level is populated (Dere and Mason 1981):

(a) Allowed lines that are collisionally excited from the ground level. The emissivities of these lines are proportional to n_e^2.

(b) Forbidden or intersystem lines that originate from metastable levels. The radiative decay rates of these lines are so small that the electron collisions compete as a

depopulating mechanism. The population of the metastable levels from which these lines originate and their intensity behaviour fall into three stages, depending on the electron density. For low electron density, the radiative decay dominates and the intensity of the line has a similar behaviour to that of an allowed line ($\alpha\ n_e^2$). For intermediate electron densities, the collisional deexcitation processes are comparable with the radiative processes. The population of the metastable level becomes significant, and the intensity of the line is proportional to n_e^{δ} ($1<\delta<2$). For high electron densities, collisional processes dominate, and the metastable level is in Boltzmann equilibrium. In this stage the line intensity varies as n_e. These ranges of electron densities are dependent on atomic parameters and differ for individual ions and transitions.

(C) Allowed lines that are excited from metastable levels. Their intensities are dependent on the population of the metastable level from which they are excited. When these levels attain a non-negligible population, but not its Boltzmann value, the line intensity will vary as n_e^{δ} ($2<\delta<3$). When the metastable levels reach a Boltzmann equilibrium, the intensities of these lines vary as n_e^2.

The ratio of lines with different electron density dependence has been extensively used as an electron density diagnostic for the solar atmosphere. Ideally, lines from the same ions should be used, and their ratio should be independent of electron temperature. Unfortunately, this situation cannot always be achieved, and additional uncertainties are introduced into the analysis. Line intensity ratios can be classified into three categories: (1)There is the ratio of two allowed lines, in which one of them arises from a metastable level, such as in beryllium, boron and aluminium sequences. The high density limit is reached when the metastable level reaches pseudo-Boltzmann equilibrium; the intensity ratio is then proportional to the ratio of the collisional excitation rates. Since the two lines are allowed lines, this ratio can be calculated reasonably accurately.

(2)The second category is the ratio of intersystem to allowed lines. The intensity behaviour for the low, intermediate, and high density regions was discussed above. The uncertainty in the low density limit is due to uncertainties in the collisional excitation

rates. Meanwhile, in the high density limit, the uncertainties will reflect inaccuracies in the radiative transition probability as well as in the collisional excitation rate. The greatest uncertainties in these atomic parameters is likely to be the electron collisional excitation rate for the intersystem line.

(3) The final category of line intensity ratio is the ratio of two intersystem lines from the same ion. In the low density limit, the intensity ratio is proportional to the the ratio of the collision rates, and in the high density limit it is proportional to the transition probabilities. Examples in this category includes the intersystem transitions for N III (Nussbaumer and Storey, 1979) and O IV (Flower and Nussbaumer, 1975c).

1.4.2 Electron density determination

There are two different mechanisms in which electron densities can affect spectral lines . Firstly, they can influence ionic populations of the various levels within the ion and thus influence the intensity of the line relative to other line intensities. These other lines can be emitted by the same ion, or by other different ions. This is the case which will be mostly considered in this thesis. Secondly, the widths of the lines can be affected by electron densities as a result of the Stark effect. The latter will not be discussed here, and for further details other references should be consulted e.g. Feldman (1981), Kurochka (1969) and Kurochka and Maslennikova 1975.

The determination of electron density utilising line intensities is not a new subject and has been used by many astronomers working in the optical spectral region for some time (e.g. Aller et al 1949), this method of electron density diagnostics will be mainly considered in this thesis. The familiar density diagnostic used by many optical astronomers is that of the O II lines at 3726 and 3729 Å, which is one of nitrogen isoelectronic sequences (Osterbrock 1974). The density sensitivity to the intensity ratio of O II lines arises because at nebular densities (10^3 cm^{-3}) the upper levels of the lines begin to be depopulated by electron collisions as well as spontaneous radiative decay. It is possible to find density sensitive line ratios formed at higher temperatures and densities, that emit lines at UV, EUV, and X-ray wavelengths. This can be achieved by

exploring the density sensitive properties of particular atomic configurations along an isoelectronic sequence. For example the above O II transitions in the visible occur at 1196 Å and 1213 Å for S X, which are useful as coronal electron density diagnostics.

Electron densities can thus be determined by various methods: A commonly used method is to divide the emission measure, $\int n_e^2 \, \Delta V$, by the derived volume, from spatially resolved images. This technique assumes that the observed features are fully resolved spatially. However, this is not necessarily true in many plasmas of interest which exist in different sources (Chap.2) and so this technique is fairly unreliable, since for many plasmas, such as X-ray flares in which their exact shape is not known, all estimates of the volume V in the corona are only rough approximations. In addition, even if it was possible to estimate the total V from X-ray pictures considering the fact that most of these plasmas are highly inhomogeneous, there still may exist unresolved condensations within this volume with n_e much higher than the volumetric density, $\overline{n_e} = (\frac{1}{V} \int n_e^2 \, dV)^{1/2}$. The effect of the inhomogeneity of plasmas will be discussed in more detail in Chapters 4 and 5.

The most straightforward method for electron density determination utilising line intensities is through the use of appropriately chosen line ratios from the same ion although this may not always be possible as mentioned earlier. If lines from the same ion are available, the uncertainties in the abundance of the ion species are eliminated, and the problem is reduced to a determination of the ratio of population densities in two levels.

Most density sensitive line ratios fall into one of the two general cases discussed below (cf. Doschek 1985). The principle behind these two cases is the presence of the metastable levels which makes the relative level population density dependent, as discussed in the previous section, so that the intensity ratio of two collisionally excited lines become a function of density.

The first case is a three level hypothetical atom. Figure 1.1 shows an illustration of this case as well as a schematic representation of the line ratio against electron density.

We consider level 3 as a metastable level, and level 1 as the ground level. The two transitions to be considered are $3 \rightarrow 1$ and $2 \rightarrow 1$. The transition $3 \rightarrow 1$ might typically be an intersystem line, while the transition $2 \rightarrow 1$ might be an allowed one. At all electron densities of interest, collisional excitation and deexcitation out of level 2 can be neglected compared with the radiative decay A_{21} (cf. category 2 in Sec 2.3.1). At low densities, the ion is mostly in the ground level, and levels 2 and 3 are excited by electron collisions from level 1. Every upward excitation is followed by a downward radiative decay. The line ratio $(3 \rightarrow 1)/(2 \rightarrow 1)$, in this situation, is roughly proportional to the statistical weights of the upper levels which is of order unity. As the electron density is increased, the metastable level 3 begins to be depopulated by collisional deexcitation into either level 1 or 2 because of its small decay rates A_{31} and A_{32} (i.e. $n_e(C^d_{32} + C^d_{31}) \approx A_{31}$). This results in decreasing the intensity ratio $(3 \rightarrow 1)/(2 \rightarrow 1)$. At very high densities, where collisional excitation and deexcitation out of level 2 are larger than A_{21}, the relative populations of levels 3 and 2 are in the ratio of their statistical wieghts, and the line ratio $(3 \rightarrow 1)/(2 \rightarrow 1)$ is nearly proportional to A_{31}/A_{21}, which is $<<1$. An example similar to the three level case can be found in beryllium isoelectronic sequences.

The above discussion concerning the three level case can be explained more quantitatively in order to see the behaviour of the line ratio against the electron densities of interest, assuming an isothermal plasma. By using the detailed balance equation (Equation 1.4) to calculate the two population densities n_2 and n_3 we can obtain

$$n_3 = n_1 \frac{n_e C^e_{13}}{A_{32} + A_{31} + n_e C^d_{32} + n_e C^d_{31}} \qquad (1.18)$$

and

$$n_2 = \frac{n_e n_1 c^e_{12} + \dfrac{n_1 n_e^2 c^e_{13} c^d_{32} + n_1 n_e c^e_{13} A_{32}}{A_{32} + A_{31} + n_e c^d_{32} + n c^d_{31}}}{A_{21}} \qquad (1.19)$$

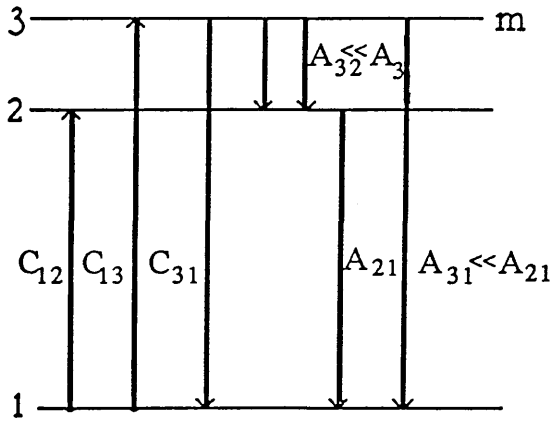

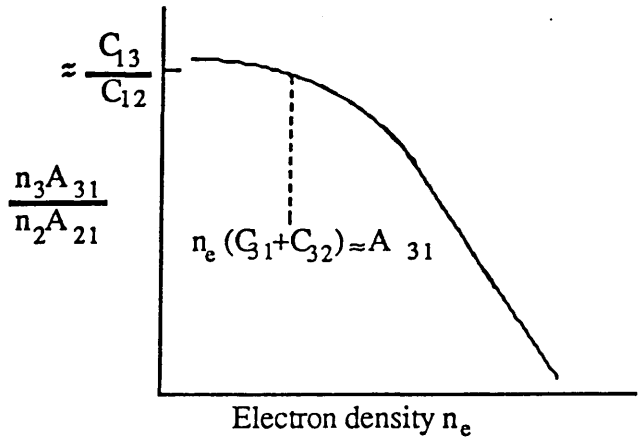

Fig. 1.1 Schematic energy level diagrams illustrating electron density plasma diagnostics (the three level hypothetical atom) Doschek 1985.

Hence using Equation (1.3) and considering the following assumptions $A_{21} >> n_e C^d_{21}$ and $n_e C^e_{23}$, $A_{31} << A_{21}$, and also $\Delta E_{12} \simeq \Delta E_{13}$ and $\Delta E_{23} / kT << 1$, we have

$$\frac{F_{31}}{F_{21}} = \frac{A_{31}}{A_{32}(1+\frac{C^e_{12}}{C^e_{13}}) + A_{31}(\frac{C^e_{12}}{C^e_{13}}) + n_e C^d_{32}(1+\frac{C^e_{12}}{C^e_{13}}) + n_e(\frac{C^d_{31}C^e_{12}}{C^e_{13}})} \qquad (1.20)$$

For the case when $n_e \rightarrow 0$, with the additional condition $A_{32} << A_{31}$, Equation (1.7) becomes

$$\frac{F_{31}}{F_{21}} \rightarrow \frac{C^e_{13}}{C^e_{12}} \qquad (1.21)$$

For large values of electron density n_e, in which A_{31} and A_{32} are much smaller than the collisional processes considered, but not as large as $A_{21} \leq n_e C^d_{21}$ and C^e_{23}, then Equation (1.20) becomes

$$\frac{F_{31}}{F_{21}} = \frac{A_{31}\,\omega_3 T^{1/2}}{\kappa n_e\left[\Omega_{23}(1+\frac{\Omega_{12}}{\Omega_{13}}) + \Omega_{12}\right]} \qquad (1.22)$$

It is clear from this equation that F_{31}/F_{21} depends only weakly on electron temperature, and is inversely proportional to the electron density.

The second case is that of the four level hypothetical atom which is illustrated in Figure 1.2. Here, level 2 is the metastable level, and we neglect collisional processes, which, for the electron densities of interest, are unimportant relative to the radiative decay in depopulating levels 3 and 4. In this situation , level 3 is easily excited from level 1. However , the excitation rate from level 1 to level 4 is much less than that from level $1 \rightarrow 3$. The intensity ratio $(4\rightarrow2)/(3\rightarrow1)$ is proportional to the collisional excitation rates from the ground level 1 into both levels 3 and 4, i.e.α C^e_{14}/C^e_{13}, which is of the order 1/10. As the density increases, the collisional mixing between the ground and the metastable level results in level 2 attaining a non-negligible population. Therefore the excitation rate $2\rightarrow4$, becomes strong and comparable to, or even greater than , $1\rightarrow3$, resulting in the increase of the line ratio $(4\rightarrow2)/(3\rightarrow1)$. At very high densities, level 1 and

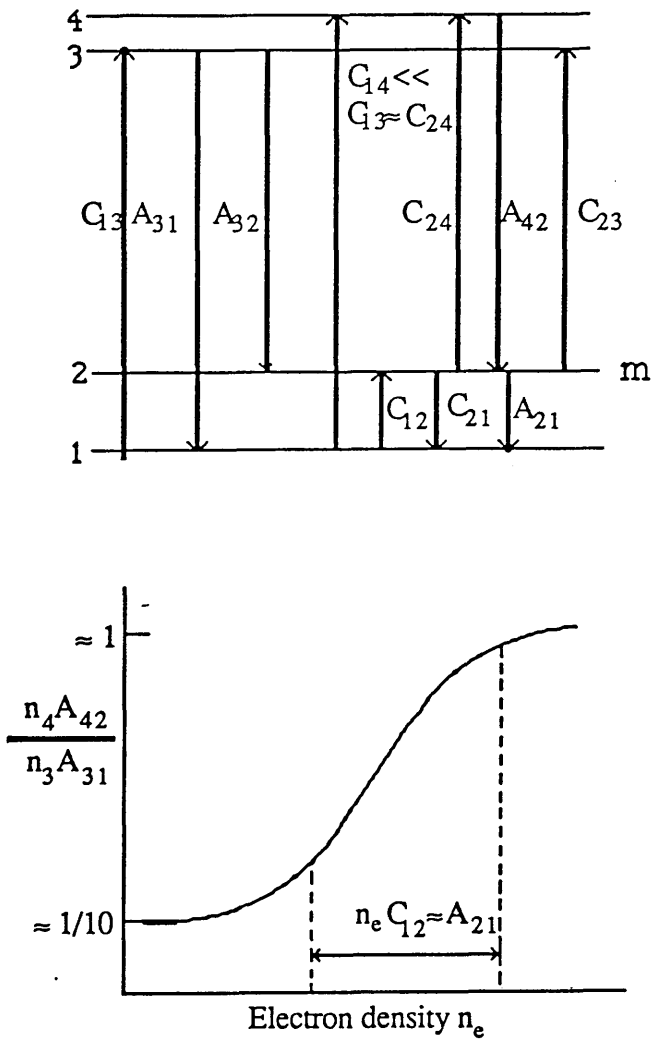

Fig. 1.2 Schematic energy level diagrams illustrating electron density plasma diagnostics (the four level hypothetical atom). Doschek 1985.

level 2 reach a statistical population distribution and the ratio 4→2/3→1 is no longer sensitive to the electron density. We should mention that the most useful density sensitivity region is roughly where $n_e C^e_{12} = A_{21}$.

As far as the above discussion is concerned, the four level case can also be explained more quantitatively. In order to calculate the relative populations in the four levels, we use the detailed balance equation (Equation 1.4),.and obtain:

$$n_4 = \frac{n_e(n_1 C^e_{14} + n_2 C^e_{24})}{A_{42}} \tag{1.23}$$

for level 3

$$n_3 = \frac{n_e(n_1 C^e_{13} + n_2 C^e_{23})}{A_{31} + A_{32}} \tag{1.24}$$

and for level 2

$$n_1 n_e C^e_{12} + n_3 A_{32} + n_4 A_{42} = n_2 n_e C^d_{21} + n_2 A_{21} + n_2 n_e C^e_{23} + n_2 n_e C^e_{24} \tag{1.25}$$

From equations (1.23)-(1.25), the quantity n_2/n_1 can be obtained, viz

$$\frac{n_2}{n_1} = \frac{C^e_{12} + C^e_{13}\dfrac{A_{32}}{A_{31}+A_{32}} + C^e_{14}}{\dfrac{A_{21}}{n_e} + C^d_{21} + C^e_{23}\dfrac{A_{31}}{A_{31}+A_{32}} + \dfrac{C^e_{24}}{A_{42}}} \tag{1.26}$$

Therefore the flux ratio for the two lines F_{42}/F_{31} can be written as

$$\frac{F_{42}}{F_{31}} = \frac{(n_e n_1 C^e_{14} + n_e n_2 C^e_{24})}{B_{31}(n_e n_1 C^e_{13} + n_e n_2 C^e_{23})} \tag{1.27}$$

where

$$B_{31} = \frac{A_{31}}{A_{31} + A_{32}} \tag{1.28}$$

Equation (1.27) can also be written in the form

$$\frac{F_{42}}{F_{31}} = \frac{(C^e_{14} + (\frac{n_2}{n_1}) C^e_{24})}{B_{31} C^e_{13} + (\frac{n_2}{n_1}) C^e_{23})} \qquad (1.29)$$

from which it is clear that as $n_e \rightarrow 0$ the flux ratio becomes

$$\frac{F_{42}}{F_{31}} = \frac{C^e_{14}}{B_{31} C^e_{13}} \qquad (1.30)$$

since $A_{31} >> A_{32}$, from equation (1.28), $B_{31} \approx 1$. Therefore equation (1.30) , as $n_e \rightarrow 0$, approaches

$$\frac{F_{42}}{F_{31}} = \frac{C^e_{14}}{C^e_{13}} \qquad (1.31)$$

For large electron densities, F_{42}/F_{31} becomes independent of n_e, since A_{21}/n_e Equation (1.26) becomes very small compared to the other terms in the denominator.

It should be mentioned that if the density at the temperature of the line formation is either much below or above the range of optimal density sensitivity, the line ratios will not be useful density indicators.

The two general cases discussed above can be summarised in a simpler way. In both cases the sensitivity arises when the collisional processes can compete with the radiative decay in determining the metastable level population. The first case can be considered as the one in which the metastable level is in the ground configuration and the second where the metastable level arises in an excited configuration. The intensity of a line which is excited from a lower metastable level increases relative to a line unaffected by collisional processes. The second case is where the intensity of a line arising from a metastable level decreases relative to the intensity of a line that arises from a level unaffected by collisional depopulation. If there are several metastable levels with different decay rates, the ratios of lines arising from these different levels are also density sensitive.

Another line ratio technique for determining electron densities has been developed by Feldman et al (1977). In this technique the electron densities are determined by calculating the ratio of an intersystem line to an allowed line of another ion, formed at the same temperature. In this method there is no upper limit in density, and therefore it is particularly useful for active regions and flares, where the density tends to have higher values. A summary of this technique can be described simply by considering a hypothetical two-level atom in which the excited level (level 2) is metastable. The statistical equilibrium equation (Equation 1.4) reduces to

$$n_1 n_e C^e_{12} = n_2 A_{21} + n_2 C^d_{21} n_e \qquad (1.32)$$

By using the expression for C^d_{21}, and writing $n_1+n_2=n_{ion}$, Equation (1.32) can be reexpressed as

$$\frac{n_2}{n_e n_{ion}} = \frac{C^e_{12}}{A_{21} + n_e C^e_{12}(1 + \frac{\omega_1}{\omega_2} \exp(E_{12}/kT)} \qquad (1.33)$$

when $n_e \rightarrow 0$, $\frac{n_2}{n_e n_{1on}} \rightarrow \frac{C^e_{12}}{A_{21}}$ which is proportional to $\frac{\exp(-E_{21}/kT)}{T^{1/2}}$, see Equation (1.7), and this quantity is temperature dependent only. As the density becomes very high $\frac{n_2}{n_e n_{1on}} \propto \frac{1}{n_e}$ as in Fig. 1.3. In this Figure the ratio is plotted of the population of the metastable levels to the product of the electron density and the density of the ion in which the line arises, as a function of electron density. The above discussion showed the density sensitivity to some excited levels of ions that can be utilised in the 1100-2000 Å region and lower transition region. The quantity $n_2/n_e\, n_{ion}$ is proportional to the flux ratio of the intersystem line to an allowed line formed at the same temperature. This can be seen clearly, following Equation (1.3) for the expression of the flux in the intersystem line, assuming a two-level ion,viz

$$F^I_{12} \propto n^I_2 \, \Delta V \qquad (1.34)$$

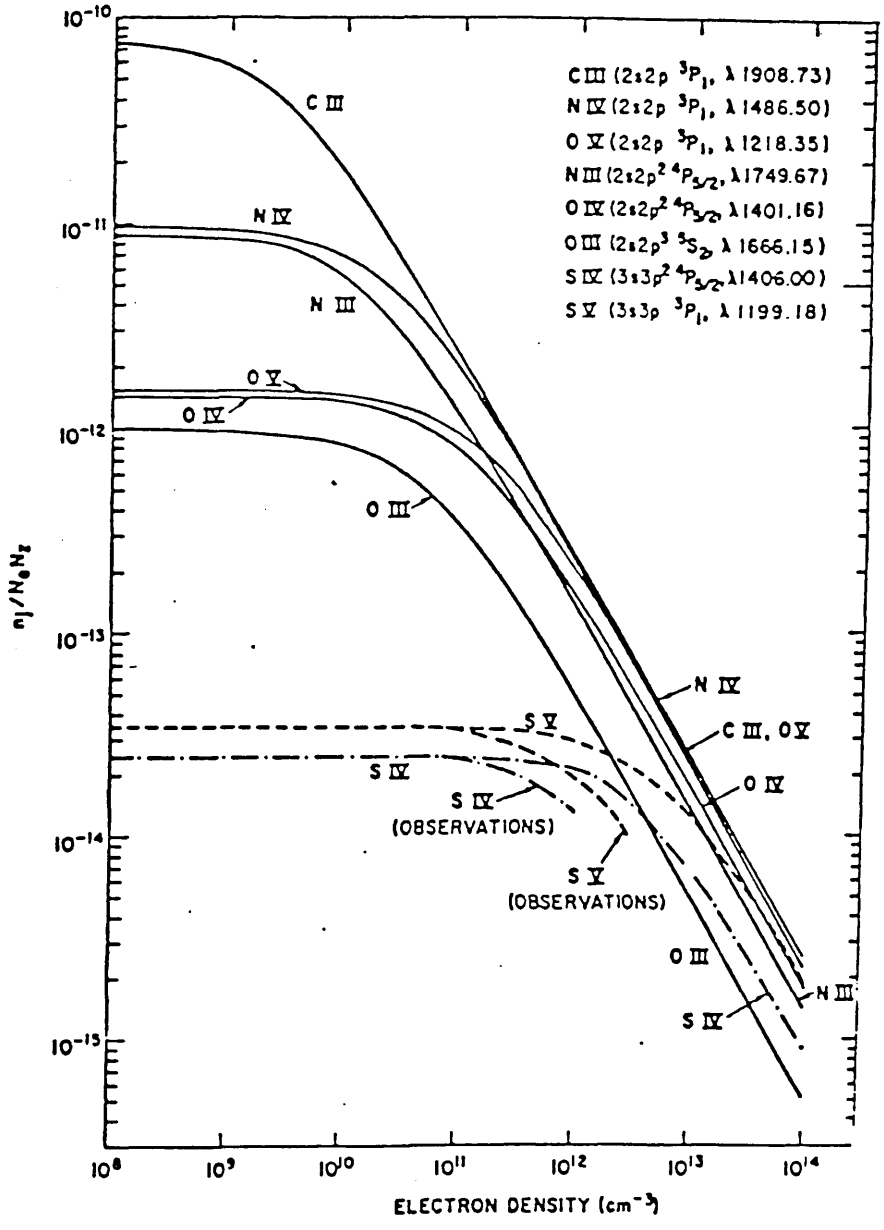

Fig. 1.3 Populations of levels and ions indicated as a function of electron density.(Doschek 1985)

and the flux in the allowed line can be expressed, via Equation (1.10), viz

$$F_{12}^{A} \propto n_e \, n_{ion}^{A} \, \Delta V \qquad (1.35)$$

If ionisation equilibrium is assumed , the ion abundance n_{ion}^{A} can be related to the intersystem's ion abundance n_{ion}^{I} by a factor β, which is a constant containing the relative abundance factors, i.e. $n_{ion}^{A} = \beta \, n_{ion}^{I}$. By taking the ratio of the intersystem line to the allowed line we get

$$R = \frac{F_{12}^{I}}{F_{12}^{A}} \propto \frac{1}{\beta} \frac{n_2^{I}}{n_e \, n_{ion}^{I}} \qquad (1.36)$$

It is clear from the above equation that the line ratio, which is a function of electron density, can be obtained if n_2/n_{ion} is known for a particular ion and β is determined from a suitable allowed line. This technique has the advantage of being strongly sensitive to the density as well as its relative insensitivity to errors in atomic data.

The upper limit of the electron density that can be obtained by this technique is determined by the instrument sensitivity. As an example for this technique, O IV line (1401 Å) can be used as the intersystem line, and C IV and N V lines at 1550 Å and 1238 Å respectively can be used as the allowed lines.

It should be mentioned that because of the limited spectral range of the instrument, it was not possible to observe simultaneously an allowed line of the same ion in order to determine the emission measure. Therefore, the appropriate emission measure for O IV was taken as the average of C IV and N V emission measures. The advantage of this here is that the ratios using these kinds of lines are much more sensitive to electron density than other line ratios involving only intersystem lines, and in some cases such lines provide the only available diagnostics. Fig. 1.3 includes a summary of some of the useful density sensitive lines in the 1100-2000 Å range and lower transition region.

Another technique which is very useful for plasma diagnostic purposes at X-ray wavelengths (<25 Å) has been developed by Gabriel and Jordan (1969), who were the first to explore the X-ray region for plasma diagnostics useful for solar applications.

At high temperatures (>5x10^6 K) most of the light elements are ionised to their He-like and H-like ionisation stages. Fig.1.4 shows the term diagram for the relevant transitions in the He-like ions in which, for elements such as Ca and Fe, four lines can be seen. These lines are the resonance line (W), the quadrupole line (X), the intersystem line (Y) and the forbidden line (Z). For light elements, such as O, the quadrupole line (X) is too weak to be observed. Gabriel and Jordan were also the first to recognize, an important property of the He-like ions; that the ratio of the forbidden line to the intersystem line, Z/Y, is density dependent. They expressed the line ratio, of the forbidden line to the intersystem line, in the form

$$R = R_\alpha \frac{A_{21}}{(1+F)C^e n_e + A_{21}} \qquad (1.37)$$

where A_{21} is $^3S_1$-$^1S_0$ the transition probability and C^e is the collisional excitation rate of ^3S-^3P. F is the ratio of the collisional excitation rates, namely

$$F = \frac{C^e(^1S - ^3S)}{C^e(^1S - ^3P)} \qquad (1.38)$$

and

$$R_\alpha = \left[\frac{(1+F)}{b}\right] - 1 \qquad (1.39)$$

where b is the effective branching ratio, which is a function of the transition probabilities from the ^3P state to the ground state.

At low electron densities, when (1+F) C_e n_e << A_{21}, R in Equation (1.37) is approximately equal to R_α. As the electron density is increased the excitation rate becomes comparable to A_{21}, and the ratio decreases. Fig.1.5 shows the line ratio against the electron density for three He-like ions, O VII, Ne IX and Mg XI. The heaviest ion

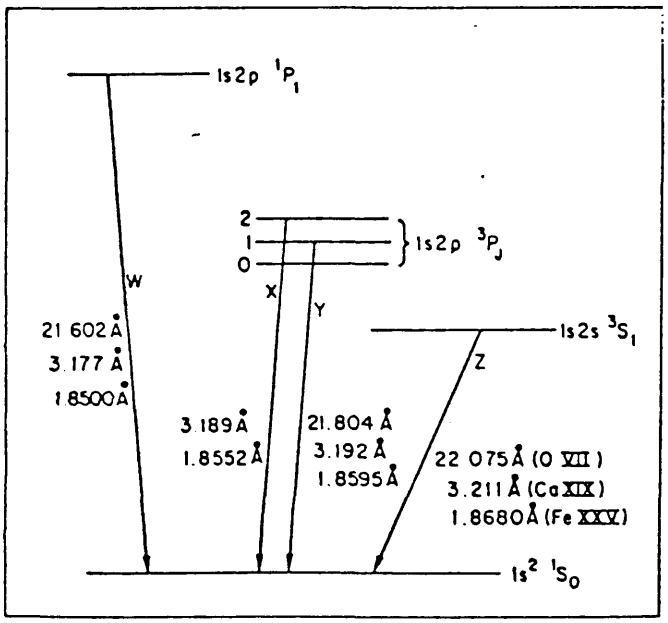

Fig. 1.4 Energy level diagram for ions of the He isoelectronic sequence.

Mg XI provides useful diagnostics for solar flare densities which, as far as we know, do not exceed about 10^{13} cm^{-3}.

Many useful reviews and discussions for solar atmosphere diagnostics can be found, e.g. Feldman (1981), Doschek (1985), Dere and Mason (1981), Feldman et al (1978), Dere et al (1979), Jordan (1979), Gabriel and Jordan (1972), and Feldman et al (1977). Some of the useful electron density diagnostics in the UV wavelength region have been summarized by Dere and Mason (1981), shown in Fig.6, also in Table 2 Doschek (1985), in which the densities are expressed in terms of the electron pressure.

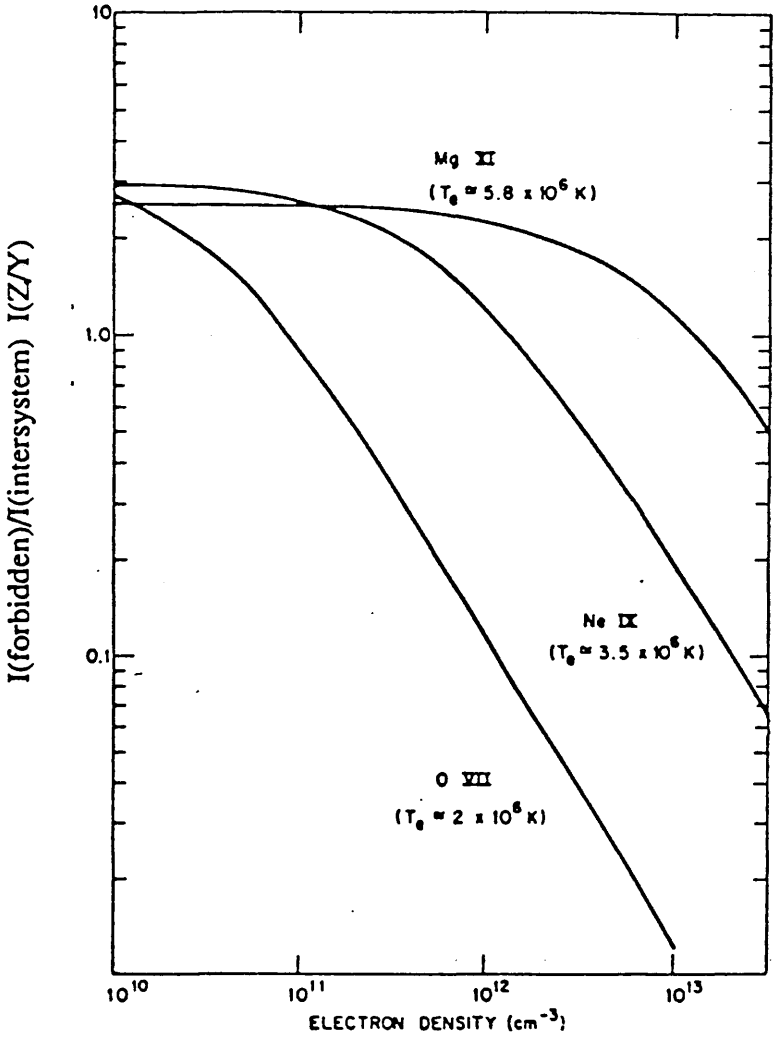

Fig. 1.5 Ratio of forbidden to the intersystem line for three ions of the He isoelectronic sequence.

Table 1.2

Electron pressures

Region	Log(n_e(cm^{-3})T(K))
Quiet sun (chromosphere)	15.2
Quiet sun (transition region)	15.1
Quiet sun (corona)	15.0(h>20 arc-sec)
Coronal hole (transition region)	15.1 (14.8)
Active region (chromosphere)	15.2
Active region (transition region)	15.9
Active region (corona)	15.2-16.0
Prominence (transition region)	14.9
Sunspot (transition region)	15.0
Surges (flare-related activity)	
(transition region)	15.0-16.2
Flares (transition region)	16.0-18.0
Flares (coronas, 10^6K<T<6x10^6)	16.8-18.7

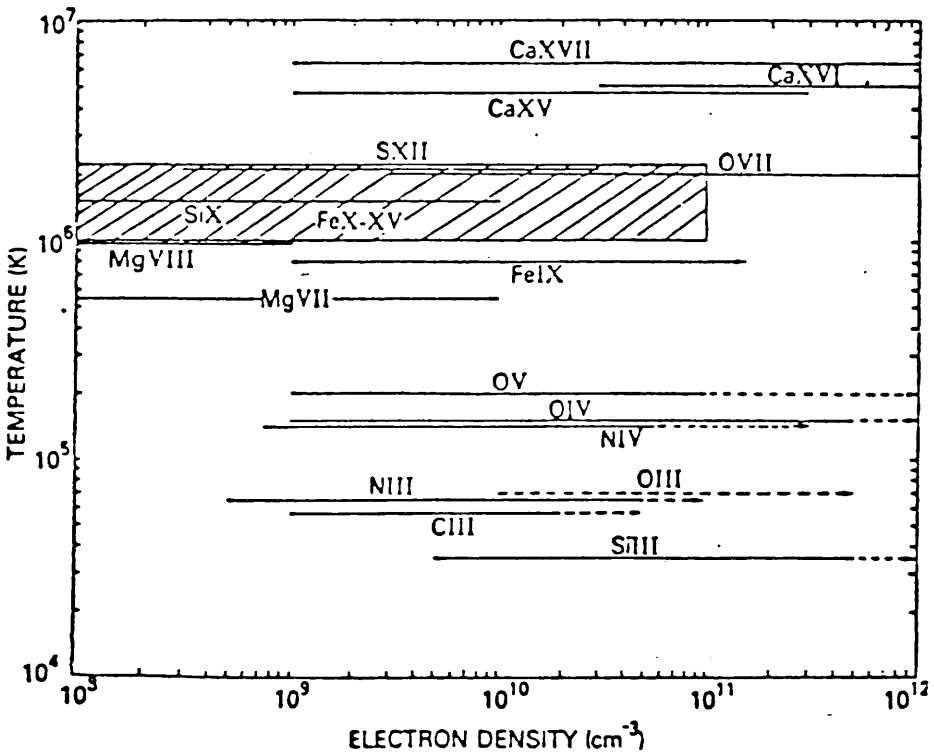

Fig. 1.6 Range of density sensitivity of ions formed at different temperatures, Dere and Mason (1981).

1.5. Emission Measure Analysis

It is clear from the previous sections (section 2.3 and section 2.4) that the spectral diagnostic techniques require only relative line intensities, namely line ratios. However, the absolute line intensity of a spectral line contains very important information concerning the emitting region, namely, the quantity of the plasma present that is in the appropriate physical state for emitting that line.

Following equation (1.12), in which the flux of a spectral line can be obtained, and by utilizing the expression of C^{e}_{ij} we find

$$F_{ij} = \frac{0.8}{4\pi R^2} E_{ij} A_H \int_{\Delta V} \kappa \frac{\Omega_{ij}}{\omega_i T^{-1/2}} \exp\left(\frac{E_{ij}}{KT}\right) f(T)\, n_e^2\, dV \qquad (1.41)$$

$$F_{ij} = \frac{0.8}{4\pi R^2} E_{ij} A_H \kappa \frac{\Omega_{ij}}{\omega_i} \int_{\Delta V} \frac{\exp\left(\frac{E_{ij}}{KT}\right)}{T^{1/2}} f(T)\, n_e^2\, dV \qquad (1.42)$$

$$= \beta_{\cdot} \int_{\Delta V} G(T)\, n_e^2\, dV \qquad (1.43)$$

where the dependence on density and temperature is explicit, and the integral is carried out over the plasma volume falling within the field of view of the spectrometer. It should be mentioned that however good the spatial resolution of the telescope/spectrometer system, the observations will always be unable to resolve along the line of sight direction. Therefore the integral will in general include a range of different plasma conditions. In equation (1.43) the function G(T) contains all the temperature dependent terms of the line considered, and has been defined by Pottash (1963) and is strongly peaked in temperature. This function is often referred to as the contribution function. If the volume contains isothermal plasma at temperature T, the observed flux becomes

$$F_{ij} = \beta_{\cdot}\, G(T) \int_{\Delta V} n_e^2\, dV \qquad (1.44)$$

If the temperature T is known, then the emission measure $\int_{\Delta V} n_e^2 \, dV$ can be derived from the observed line. For sharply peaked G functions, the temperature is often assumed to be that which maximizes G which will be denoted here as T_m. It is possible, therefore to obtain "isothermal" emission measures as a function of temperature from a set of observed line intensities.

It is clear, Equation (1.44), that the emission measure may be defined as the square of the electron density integrated over the volume of the emitting plasma. However, the simple assumption of an emitting plasma of a single temperature is often inadequate, and a concept of a collection of sources with different temperatures and emission measures must be introduced. Craig and Brown (1976), by assuming a continous distribution of source temperatures, have introduced the concept of a differential emission measure. This is done by converting the integral over volume into an integral over surfaces of constant temperature and an integral over temperature, viz.

$$F_{ij} = \beta_{\cdot} \iiint G(T)\, n_e^2 |\nabla T|^{-1} ds\, dT \qquad (1.45)$$

or

$$F_{ij} = \beta_{\cdot} \int G(T)\, \xi(T)\, dT \qquad (1.46)$$

where $\xi(T)$ is called the differential emission measure and is given by

$$\xi(T) = \iint_{S_T} n_e^2 \, |\nabla T|^{-1} dS \qquad (1.47)$$

and the integration is performed over all surfaces S_T at temperature T.

1.6 Summary

In this Chapter we have considered the importance of solar spectroscopy for the determination of the various parameters in solar plasmas (electron temperature and density) with particular reference to the techniques applied. We concentrated solely on the EUV and X-ray region of the electromagnetic spectrum, and discussed in detail the

atomic physics involved. In what follows we shall see how much we can learn about solar plasma from analysing these wavelengths regions.

CHAPTER 2

SOLAR AND ASTROPHYSICAL PLASMAS

2.1 Introduction

Astrophysical spectroscopy in the UV, EUV, and X-ray spectral regions is a rich and extensive field of study which covers a diverse range of phenomena. Much of the material in the universe exists under highly varied physical conditions and is in a form suitable for study by spectroscopic means. The observable atmospheres of the sun and other stars display a large diversity in temperature and density. For example, transient phenomena such as solar flares may reflect temperatures of the order of $\sim 10^7$ K, while compact sources of hard X-ray emission may produce even higher temperatures. At high temperatures EUV and X-ray emission lines are produced due to the high levels of ionisations and excitations of the atoms. Space observations are, therefore, required to study these regions. By contrast to these discrete sources, interstellar space contains very much cooler and more diffuse material. Information from HTSS radiation, therefore, provides a unique diagnostic tool for the study of stars and interstellar material that is unobtainable in other wavelengths. In particular, the sun, due to its proximity, has been the subject of many investigations and provides an ideal laboratory for spectroscopic studies.

During the past ten years intense activity has been directed toward the determination of electron density in the solar atmosphere using diagnostic line ratios, as shown in the preceeding Chapter. These techniques have contributed to the desired goals of a better understanding of physical conditions in flares, active regions, sunspots, coronal holes, solar winds, and the quiet sun. The use of these techniques has led to some fundamental discoveries about the nature of the solar atmosphere. The transition region was conventionally envisaged as a homogeneous layer between the low temperature chromosphere and the high temperature corona. It is now commonly accepted that it has unknown filamentary structures with very small "filling factors" at low temperatures.

Space observations of the sun have been performed by NASA's Orbiting Solar Observatory (OSO) satellites, during the 1960's and early 1970's, the Apollo Telescope

Mount (ATM) on Skylab during 1972 and 1973, and the Solar Maximum Mission (SMM) during the 1980's. The basis of our current understanding of the outer atmosphere has been obtained through observations made by the OSO's and ATM, while the SMM observations were mainly, restricted to studies of solar flares. Observations in the EUV range are, as yet, inadequate. Skylab, for example, had very limited spectroscopic capabilities at such wavelengths, whilst OSO and SMM lacked any suitable instrumentation. However, Solar Heliospheric Observatory (SOHO), which will be launched in March 1995, is a solar observatory devoted to increasing our understanding of the solar atmosphere and the solar wind. This satellite aims to address three fundamental goals, namely to understand: the acceleration of solar wind, the nature of solar corona, and the interior of the sun.

The main purpose of this chapter is to outline the present status of solar physics of the outer solar atmosphere and to discuss some examples of the commonly used density diagnostics in the different regions of the atmosphere. The limitations and accuracies of various methods used to analyse the X-ray and UV spectra will be mentioned, with particular focus on the effect of the high degree of inhomogeneity found in most plasma structures.

2.2 The Solar Atmosphere and UV, EUV, X-ray observations.

The temperature and density structure of the different solar regions are illustrated in Figure 2.1 which shows a simplified stratified model of the outer layers of the sun, from 1000 km below the visible surface (photosphere) to 3000 km above. It should be emphasised, however, that the different solar regions are better classified in terms of their temperature and density structure than by some arbitrarly determined height above some suitably chosen reference level (see discussion in section 2.2.2.). The photosphere of the sun has a characteristic temperature of around 6000 K, while the corona refers to temperature regions at and above 10^6 K. There exists a very steep temperature gradient in a region between chromospheric temperature and coronal temperatures, known as the transition region. Note also that atmospheric regions with higher temperatures tend on

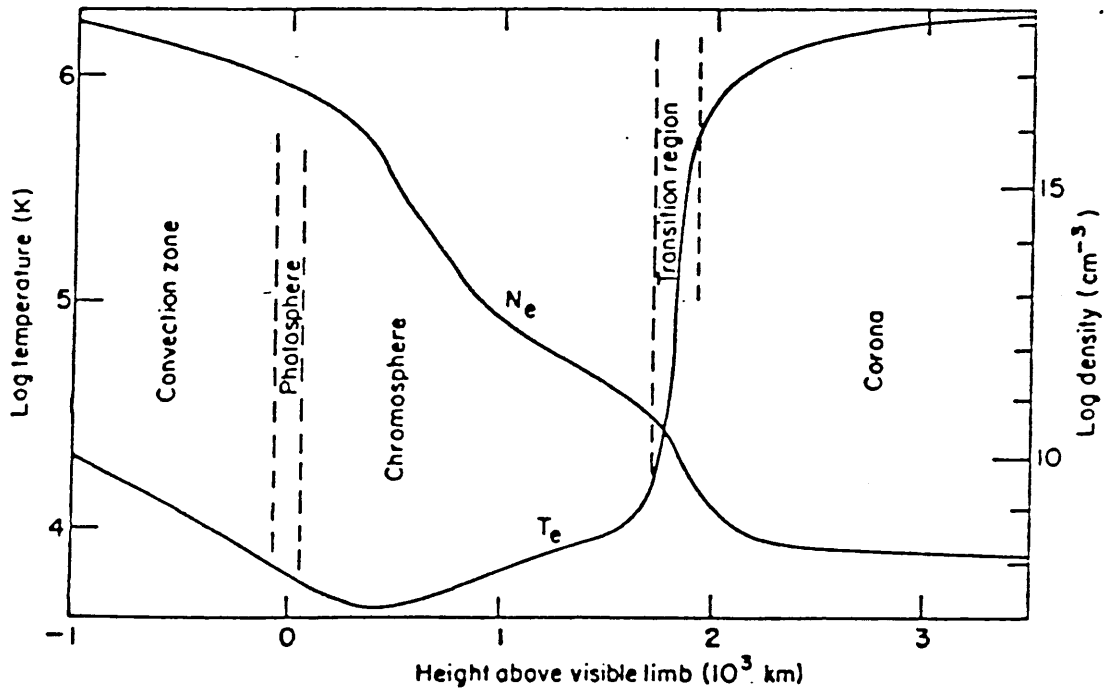

Fig. 2.1 Schematic representation of the variation with height of the mean values of temperature and density in the outer layers of the sun. Gabriel and Mason (1982).

average to have lower densities. In what follows we shall concentrate on the high temperature regions of the solar atmosphere. For a detailed discussion of the photosphere and chromosphere other references should be consulted, e.g. Zirin (1988) and Durrant (1987).

2.2.1.Solar corona

During a total eclipse of the sun, a fascinating view of a white halo appears beyond the edge of the moon, stretching for large distances out into space. The occultation of the sun is very important in order to observe the outer atmosphere, or solar corona, since the visible light from this region is about a million times fainter than the radiation from the solar disc. This may be done artificially using a special telescope known as choronograph. The coronal visible light is actually solar disc radiation scattered towards us by the free electrons in the corona (Thomson scattering) Doschek (1985), and Zirin (1988). These electrons are produced by the high coronal temperature, which under quiet conditions, i.e. no flares or any other activity, is about 1.5×10^6 K. At this temperature, the major constituent of the coronal gas, hydrogen, is almost completely ionised. Other elements present, such as C, O, Si, and Fe, are also highly ionised.

The discovery of very high temperatures in the solar corona was mainly based on the spectroscopic identification of emission lines appearing in the visible spectrum of the solar corona. The existence of a very high temperature in the solar corona means that coronal emission is concentrated in the EUV and X-ray regions of the spectrum. At these wavelengths there is almost no continuous emission from the photosphere and bound-bound transitions in the corona produce line radiation of greater intensity than the continuum. The result is the appearance of bright emission lines rather than the dark absorption lines which exist at visible wavelengths.

The density of the corona can be obtained from coronal observations and is found to be quite low. Unlike the temperature, which rises by approximately 100 times greater than the photosphere's, just where the density drops by nearly an amount of the same

order. The electron density in the low corona ranges between 10^8 and 10^9 cm^{-3} in quiet regions.

Photographs of the corona in visible and X-ray wavelengths are shown in Fig. 2.2. The X-ray photograph has been overlaid on the white light photograph of the outer corona. The X-ray photograph was obtained on 30 June 1973 at 1145 UT using the American Science and Engineering (AS&E) X-ray telescope on Skylab. At about the same time the white light photograph was obtained by the High Altitude Observatory (HAO).

It is clear from these photographs that the nature of the corona is inhomogeneous and highly structured. It is rather difficult to find any region of the corona that could be called typical or average, and furthermore images from Skylab show that the basic structural component of the solar corona is in the form of loops or arches. These loops and arches are the outlines of magnetic field lines. In addition, these structures can be quite small, only a few arc seconds across, or can be very long and extended across a significant fraction of the solar disc.

Loop like structures do not occur uniformly throughout the corona. In coronal hole regions, where the magnetic field is much weaker, the field lines are not closed but open (they close at enormous distances from the sun, but are considered as open near the surface). The X-ray emission from these regions is negligible compared to the closed field regions (cf. the large dark areas in the X-ray image in Fig.2.2). It is now known that the coronal gas temperature is less in the holes than in the closed loops and the density is less than the quiet sun regions (Doschek and Feldman 1977). These differences in physical conditions are the result of the differences in the magnetic structure of loops and holes. The plasma is contained in the loops because the magnetic pressure $B^2/8\pi$ equals or is greater than the gas pressure $2n_ekT$ (B is the magnetic field strength) which can therefore build up, whereas in open field regions material can flow freely along the field lines and escape into the interplanetary medium, where they can be detected streaming past the earth. The high speed solar wind therefore arises almost exclusively

Fig.2.2 Soft X-ray and white light photographs of the sun. The solar disc is dark in X-ray but so bright at visible wavelengths that it must be occulated in order to observe the faint solar corona. Doschek (1985).

from coronal holes.

Opposite in character to the coronal holes are the regions above sunspots, known as active regions. The term "active region" is used to signify an area of enhanced magnetic field. The hot dense plasma regions associated with this intense field may often take the form of a loop or loop segments, i.e. closed field lines. These loops last longer than expected from their known radiative losses, suggesting that a source of local heating is responsible for the observed emissions. (The form of the heating mechanism in such sources is of general interest since it is assumed to be related to the mechanisms producing flares and sustaining the solar corona. It should be mentioned that the exact mechanism of heating the corona is not known and remains one of the fundamental problems of solar physics). We regard an active region as the totality of all phenomena accompanying the birth and early development of a solar magnetic region. Typically, this phase includes the continuous presence of sunspots, plages, and hot coronal plasma as well as the occurrence of those energetic phenomena that give the active region its name (i.e., flares bombs, surges, eruptive prominences, and coronal transients). However, it is interesting to note that these energetic phenomena occupy only part of even the early phase of a magnetic region, and that during intervening times an active region may be relatively quiet. In active regions the chromosphere and the transition region are very bright in UV and X-ray lines, mainly because of the greater electron density. Here the magnetic field can be much stronger and more complex than the quiet sun or coronal holes. It should be noted that when solar activity is near maximum, the coronal holes are nearly absent, and instead we see prominences, a large number of active regions and sunspots, together with a dramatic rise in the number and size of solar flares. In images obtained with the Naval Research Laboratory (NRL) slitless spectrograph on Skylab, active regions can be seen composed of complicated sets of loops at different temperatures. Improvements in the techniques of EUV and X-ray observations with good spatial resolution, e.g. the instruments on the ATM have made it possible to study active regions and associated flares using lines in spectral regions where previously only quiet sun emission had been observed. Although some excellent rocket spectra in the EUV

region have been obtained (e.g., Brown et al. 1986), work in this region has been hampered by low fluxes and the need for high precision in the development of instrumentation. Until recently only the NASA OSO-5 spacecraft had obtained a substantial data set near 100 Å, which included quiet sun, active regions, and flares. However, for this instrument neither the time resolution (on the order of minutes) nor the spectral resolution (~ 0.1 Å) was very high. Thus the wavelength region between about 25 and 150 Å still needs much exploration.

The SOHO mission offers some improvement in the study of active region plasmas having instruments with better spatial and temporal resolution than previous satellites. Measurements will be made by a combination of normal and grazing spectrometers (Solar Ultraviolet Measurements of Emitted Radiation (SUMER), and the Coronal Diagnostics Spectrometer (CDS) which cover a wavelength range in EUV and X-ray, containing a large number of emission lines useful for investigating the desired plasma diagnostics in the chromosphere, transition region and corona. The CDS is designed for observations in EUV region of 150-800 Å, where emission lines of highly stripped ions of characteristic temperature 10^4-$2x10^6$ K may be detected. SUMER has an operational wavelength range of 500-1600 Å corresponding to ions within a temperature range T=10^4-$2x10^6$ K. These instruments will provide information on the plasma diagnostics of the solar atmosphere, with high spatial (~2 arc seconds), spectral (a few $x10^4$), and temporal (down to 1 second) observations of the solar atmosphere. In addition, some fundamental questions about the heating mechanism for the solar corona and the origin of the solar wind will be investigated. Other instruments on board SOHO, such as UV Coronograph Spectrometer (UVCS) and the White Light and Spectrometric Coronograph (LASCO), will investigate the plasma diagnostics of the solar wind and the outer corona from a few solar radii up to 30 solar radii. For more complete details and technical descriptions, the reader should be refered to the papers by Wilhem et al. (1988) and Patchett et al. (1988).

SOHO will cover a temperature range with a maximum of~$2x10^6$ K. However, the coronal temperature in active region loops can be as high as 4-$5x10^6$ K, while in

flares the temperatures reach $25x10^6$ K or even higher. The flux tubes that contain these high temperatures range from a few tens of arcseconds to a few arcminutes in length. The electron density also becomes quite high, reaching values in some cases greater than 10^{12} cm^{-3} and being typically about 10^{11} cm^{-3}. Material at chromospheric temperatures enters the low corona to form long and low, almost horizontal structures, usually with one end rooted to a nearby sunspot. On the solar disc these structures are seen as dark filaments, whereas at the limb they appear as bright prominences extending above the chromosphere. The different appearance is because they emit less visible radiation than the underlying disc but more than the surrounding corona.

Prominences are cool plasmas ($<10^5$ K) of complex magnetic flux loops that can extend fairly high into the corona. They can sometimes explode (eruptive prominences), spraying cold hydrogen into the corona to distances of many solar radii, producing a so called coronal transient. The eruption does not consist only of prominence material but also of the material and field of the coronal active region loops overlaying and enclosing the prominence before it erupts. In addition to prominences, there exist many other active solar phenomena, such as surges, sprays, coronal mass ejections and flares.

2.2.2.The Transition Region

The atmosphere at temperatures between $2x10^4$ K and 10^6 K is known as the transition region. This region separates the warm material of the chromosphere ($T \leq 2x10^4 K$) from the very hot corona ($T \geq 10^6$). The only satisfactory way to study the hotter regions of the sun's atmosphere, the transition region and the corona, is by investigating UV, EUV and X-ray emission lines. Photographs of the sun obtained in spectral lines formed at transition region temperatures reveal highly inhomogeneous structures. However, as yet the detailed physical structure of the transition region is unknown.

During the last few decades models of the solar atmosphere have generally assumed a decomposition into spherically symmetrical layers, proceeding from the cold chromosphere through the transition region and into the hot corona. Such an atmosphere

could be described as one dimensional, with the temperature and density uniquely defined as a function of the solar radius (Athay 1976). Because of the strong temperature dependence of the thermal conduction coefficient ($T^{5/2}$), the transition region is extremely thin in classical models. The region around 10^5 K is predicted to be only a few kilometres thick. In these models energy is conducted from the corona through this extremely thin layer into the chromosphere, from where it radiates away. Observations with improved spectral and spatial resolution indicated that the actual structure of the transition region is very complicated and extremely inhomogeneous (Feldman 1983), and that the classical model is oversimplified. Perhaps the most outstanding observations are images of the sun in spectral lines formed near 10^5 K such as from C IV and He II which indicate that the transition region is composed of extended structures, although with very small filling factors, that appear quite similar to the spicules seen in hydrogen light. In order to overcome such difficulties, the classical plane parallel model had to be modified.

A number of models have been constructed, over many years, with one property common to all. The lower temperature limits of the structure were taken to be about 10^4 K and the upper temperature limit at about 10^6 K. The plasma at 10^5 K is assumed to come from structures in which energy is supplied by thermal conduction, and consequently the transition region between the cold and hot limits is very thin. The width of the layers between 4×10^4 K and 2.2×10^5 K is a very small fraction of 1" (1"≈ 725 Km).

Feldman (1983) discussed the implications of the transition region observations. He suggested that the transition region emission comes from two emitting regions: emission from "classical" transition region between the chromosphere and the corona and emission from unresolved filamentary structures extending into the corona, with properties that are largely unknown at present. For the above reasons, as well as others, the classical model is a gross over simplification, and in particular, the name "transition region" is a misnomer because in many cases transition region plasma does not form a physical region between chromospheric and coronal plasmas. The different atmospheric regions on the sun are defined by the emission lines they produce and an increase in

temperature does not necessarily correspond to an increase in height above the photosphere.

2.2.3.Transition Region Diagnostics

In this thesis we will be concerned mainly with electron density diagnostics, but we will briefly mention some of the temperature sensitive line ratios. The transition region electron density diagnostics which lie in the 1100-2000 Å wavelength range can be divided into two types: the ratio of two intersystem lines from the same ion or the ratio of an intersystem line to an allowed line of different ions formed over a similar temperature range. These two methods have been explained in a more detailed manner in the previous Chapter.

In the first method, the intensity ratio changes very little over a large density range. For example, the ratio of O IV intersystem lines (1407/1404.8) increases only by a factor of 3 correspond to a density range between 10^{10} and 10^{11} cm^{-3} (Hayes, 1982, 1983), and between 10^{11}-10^{12} cm^{-3}, the increase is only a factor of 1.6. Thus uncertainties in the atomic data or in the observed intensities can lead to large errors in the derived electron densities. The effect of these uncertainties, due to atomic data as well as line measurements, on the inferred densities will be considered in Chapter 6, where statistical calculations will be introduced. Examples of this method occur for O IV, Si III, N III and S IV lines between 1100 and 2000 Å.

The ratio of the intersystem to the allowed line varies rapidly and provides a sensitive method for determining electron density. This method has the advantage of much greater density sensitivity because the high density limit is reached only at densities much higher than found in a astrophysical plasmas. In this technique uncertainties can also arise in the analysis due to the difference in the emission functions for the different lines and the fact that some of the line ratios are temperature dependent. The intersystem to allowed line technique can be applied to the line ratio O IV/Si IV, (cf. Chapter 1). High time resolution observations of this line ratio indicate an enhancement in the electron density of more than an order of magnitude, in correlation with hard X-ray bursts during

solar flares (Cheng et al. 1986). These bursts are not confined to solar flares. Hayes and Shine (1987), have demonstrated the existence of *continual* small scale activity, bursts. They also compared the two techniques used for the electron density determination discussed above. Fig. 2.3 shows a comparison of the electron densities derived from the O IV multiplet with those from the Si IV/O IV ratio taken from Hayes and Shine. It is clear from this figure that the inferred densities from the two methods are inconsistent. The discrepancy could be due to the effect of the inhomogeneities of the emitting plasma, i.e. small dense structures embedded in a background transition region as predicted by Doschek (1984). The effect of plasma inhomogeneities on electron density diagnostics will be discussed in a more detailed and general treatment in Chapters 4 and 5.

It is rather difficult to find suitable density diagnostics for the lower part of the transition region ($2x10^4$ K-$2x10^5$ K). The energy difference between allowed lines and intersystem lines are of comparable values to kT. Thus many line ratios are temperature as well as density sensitive. There are, however, some ions for which density sensitive line ratios can be found that are independent of temperature. These ions, mentioned earlier, are N III and O IV (boron isoelectronic sequence), Si III (Magnesium isoelectronic sequence) and S IV (Aluminium isoelectronic sequence). The $2s2p\ ^4P$ levels in N III and O IV are metastable for electron density appropriate to the transition region (energy levels of B-like ions are shown in Fig. 2.4). The transitions involved are the $2s^22p\ ^2P^0$-$2s2p^2\ ^4P$ lines near 1750 Å for N III and 1400 Å for O IV; The $3s3p\ 3P^0$-$3p^2\ ^2P$ lines of Si III near 1300 Å, and the $3s^23p^2\ P_0$-$3s3p^2\ ^4P$ lines of S IV, also near 1400 Å making them ideal transition region lines. The density sensitivity of O IV lines have been considered by Flower and Nussbaumer (1975c), and for N III by Nussbaumer and Storey (1967). More recently O IV has been investigated by Nussbaumer and Storey (1982) and Hayes (1983). The advantage of using the ratios of lines between the $2s^2p^2\ ^4P$ and $2s^22p\ ^2P$ levels as electron density diagnostics is that these ratios are insensitive to electron temperature. One problem with this method is that the theoretical ratios are sensitive to changes in atomic parameters and it has been shown by Doschek and Feldman (1979) that 20 % changes in the radiative transition probability can lead to an

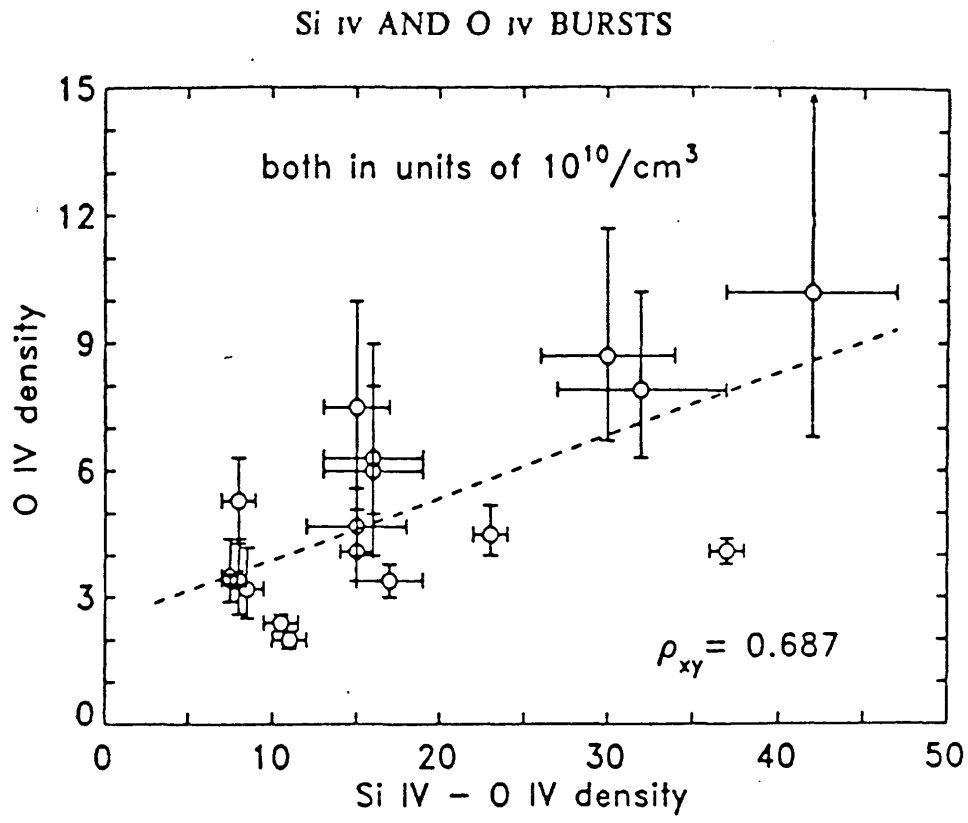

Fig. 2.3 Comparison of the electron densities derived from the Si IV/O IV diagnostic with those from the O IV multiplet only. Hayes and Shine (1987).

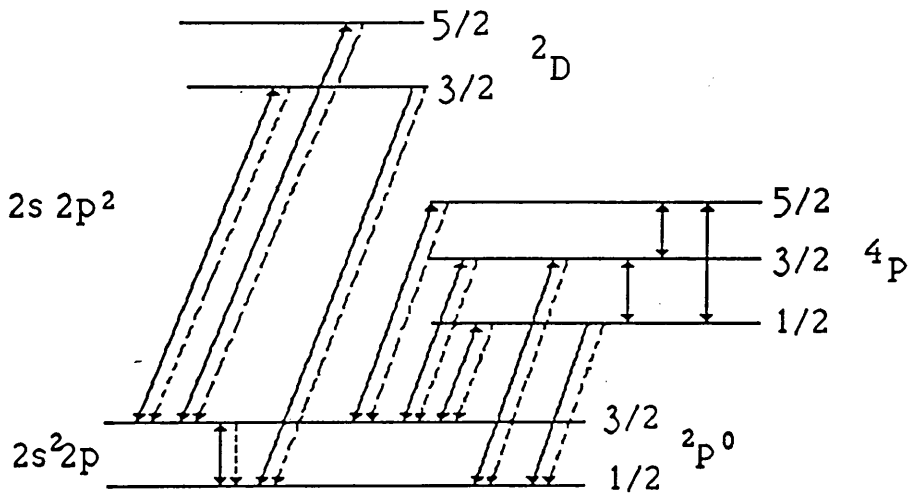

Fig. 2.4 Energy level scheme for boron-like ions: ——— Collisional transitions, ------ radiative transitions.

order of magnitude error in the inferred density.

Si III ($T=3.5\times10^4$ K) lines have been studied by Nicolas et al (1979) and Dufton et al (1983). The levels 3s3p ^3P are found to be metastable for the electron density range 5×10^9-10^{12} cm^{-3}. The most useful line ratios for diagnostic purposes are (1301 Å)/(1312 Å) and (1301 Å)/ (1296 Å). The former varies by about a factor of 20 over three orders of magnitude change in electron density, but is electron temperature dependent, while the latter, although less sensitive to electron density, has the advantage of being insensitive to electron temperature.

Probably the most extensively studied ion in the solar transition region is C III. This ion was the first to be considered for applications in this region by Jordan (1971, 1974) and independently by Munro et al (1971). Figure 1.3 shows that C III at 1909 Å is the only good line for density diagnostics below 10^{10} cm^{-3}. However, other C III lines are also very useful. For example, the triplet transition group of lines label g_i in Fig. 2.5 fall near 1176 Å ($2s2p\ ^3P$- $2p^2\ ^3P$), and the resonance line at 977 Å ($2s^2\ ^1S_0$-$2s2p\ ^1P_1$), line c in Fig.2.5.The ratio of these lines to the intersystem 1909 Å line ($2s^2\ ^1S_0$-$2s2p\ ^3P_1$), line a, is both density and temperature sensitive, but all the lines can be observed by a single instrument and have been observed in solar and stellar spectra. Similarly, line e ($2s2p\ ^1P_1$-$2p^2\ ^1S_0$) in Fig. 2.5 falling near 1247 Å, has been observed in solar spectra. The ratio of this line to the intersystem line at 1909 Å is also both density and temperature sensitive. Results are shown in Fig.2.6 from Dufton et al (1978) in which, if the 1176 Å line and 1247 Å and 1909 Å lines can be observed simultaneously the temperature and the density can be obtained. In most solar features, the 997 Å and 1176 Å lines are predominantly excited by electron collisions from their respective lower levels. The levels 2s2p 3P are metastable, making the ratio (1176 Å)/(977 Å) a possible electron density diagnostics for solar conditions.

The electron density inferred from this line ratio has been a matter of some debate. The value of the line ratio that determines the electron density depends critically on atomic data . It has been emphasised by Jordan (1974) that errors in the electron excitation rates

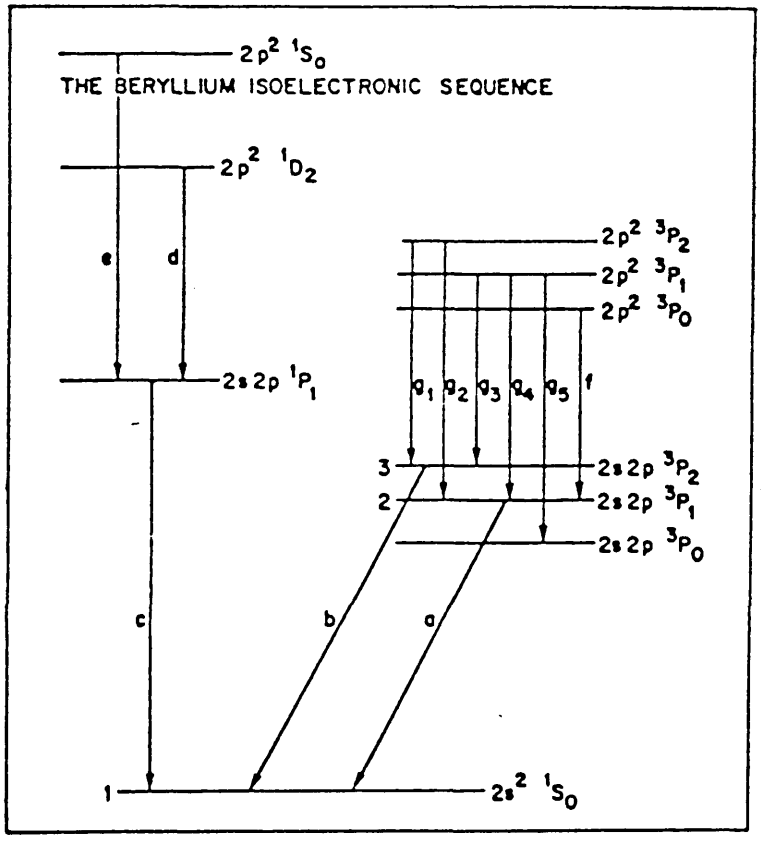

Fig. 2.5 Energy level diagram for Be I isoelectronic sequence. Doschek (1985).

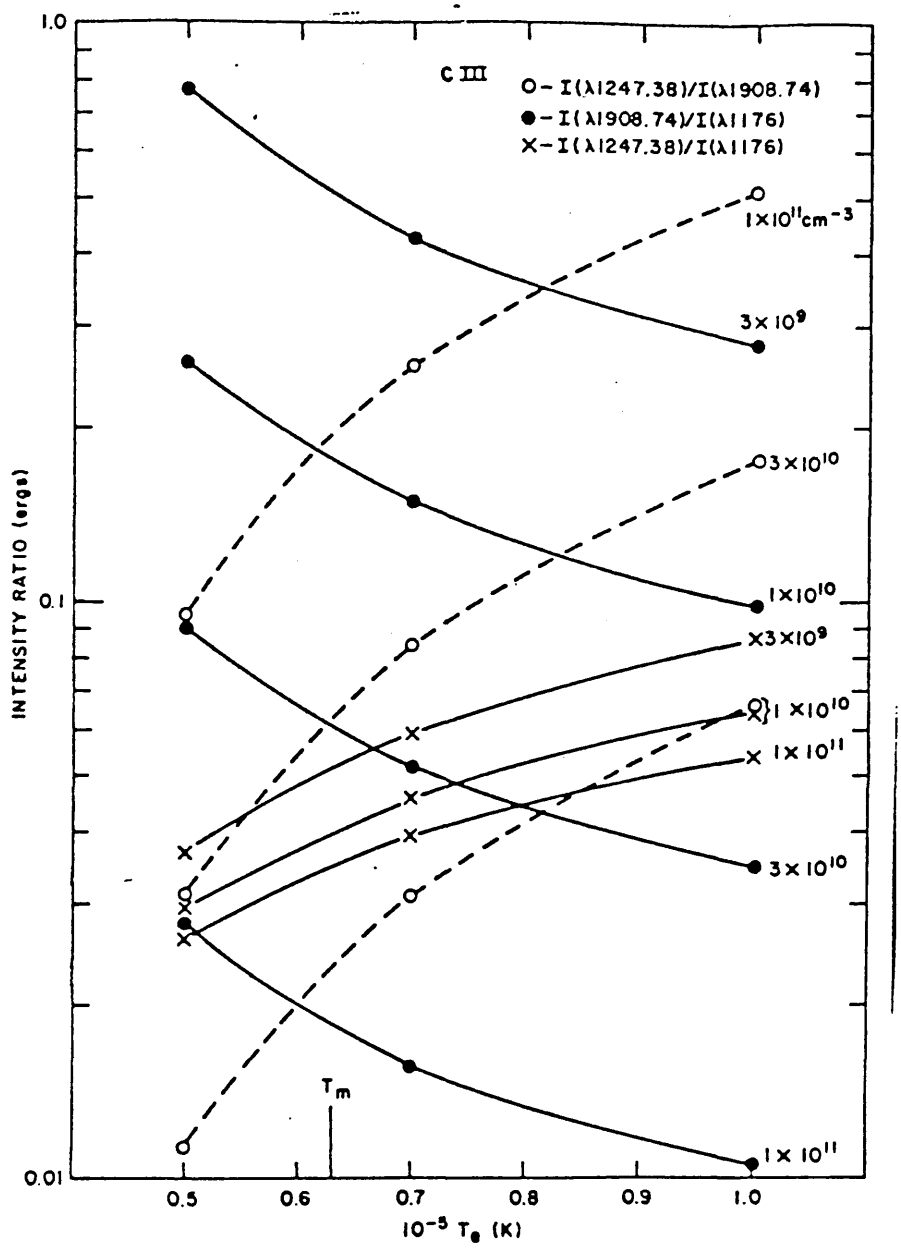

Fig. 2.6 Density and temperature sensitive line ratios of C III. The T_m is the temperature of maximum ion abundance in ionisation equilibrium. Intensity ratios are from Dufton et al (1978).

of 25% can lead to orders of magnitude difference in the electron density deduced.

Another useful ion in the beryllium sequence which can be used as a density diagnostic tool for active regions is O V ($T \sim 2.5 \times 10^5$ K). Atomic data were originally obtained by Malinovesky (1975) and later by Dufton et al. (1978). The resonance transition at 629 Å ($2s^2\ ^1S$-$2s2p\ ^1P$), see Fig. 2.5, has been used with the multiplet at 760 Å ($2s2p\ ^3P$-$2p^2\ ^3P$) arising from the metastable level as a density diagnostic for the transition region. Because of the larger radiative transition value for the ^3P-^1S transition in O V than in C III, the region of density sensitivity occurs at higher densities than for the C III ion. It can be seen from Fig. 2.7 that the ratio (760 Å/ 629 Å) is best used for density determination about 4×10^9 cm^{-3}. The observed variation of this line ratio is similar to that measured for C III.

For a summary of the electron density diagnostics in the UV wavelength region, Fig.1.6 should be consulted. It should be mentioned that several intersystem lines in the lower transition region become density sensitive at densities above $\sim 5 \times 10^{10}$ cm^{-3}, and these lines have been utilised in diagnosing densities in active regions, flares and surges. Electron densities derived using different line pairs formed at similar temperatures are found to be different by a factor of two or three. This may, in part, reflect the structure of the atmosphere, i.e. the lines are not formed in regions of the same mean density; this effect will be the main objective of Chapters 4 and 5. However, uncertainties in atomic data and in instrumental calibration may also be a cause of this discrepancy, as will be seen in Chapter 6.

The sizes of structures within the transition region are very small. From a flare observed from Skylab, it has been shown that a surge observed at lower transition region temperatures during flare onset had a characteristic length of about 60 km, <0.1". It is also evident that the high density transition region plasma coexists with nearby low density plasmas. This result was achieved by obtaining density n_e from intensity of intersystem lines and volume emission measure $n_e^2\ V$ from allowed lines (Doschek et al

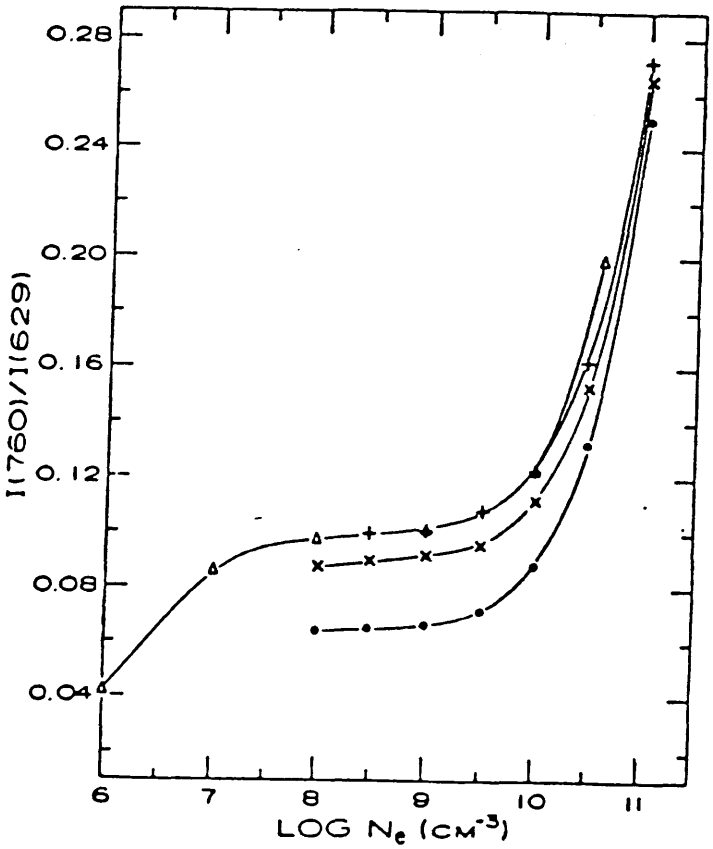

Fig. 2.7 The predicted ratio of O V lines as a function of electron density and electron temperature of 2.5×10^5 K. Open triangles represents calculations by Malinovesky (1975). The results of Dufton et al. (1978) are denoted by the remaining curves.(Dupree 1978)

(1977). Photographs made in He 304 Å radiation taken on Skylab, and spectra obtained from rockets and Spacelab 2, e.g. Dere et al (1987), showed that the transition region structures are of very small sizes. The volume of the emitting plasma can be calculated using density diagnostics such as O IV lines near 1400 Å and the emission measure calculated from allowed lines. By comparing this volume, calculated using spectroscopic diagnostics (spectroscopic volume), with the apparent volume as deduced from images, it has been calculated that the spectroscopic volume was much smaller than the apparent volume Dere et al (1987). Most density-emission measure analyses indicate that "filling factors" for the transition region emission are extremely small (0.1-0.001) (Dere 1982). In other words the transition region emission arises from very small structures that are distributed over a much larger volume.

2.3.1 Solar Flares

The solar atmosphere is often wracked by tremendous explosions, releasing huge amounts of energy and accelerating particles to extremely large velocities ($\leq$1000 km s^{-1}). These phenomena are known as solar flares, and they are intrinsically fascinating, particularly from the diagnostic point of view. Astronomers are now studying these complex explosions with a range of instruments from radio telescope arrays to gamma ray spectrometers in order to obtain a better idea about how they work. Solar flares are extremely complex and inhomogeneous in nature (see Sturrock, 1980, Svestka, 1976, and Tandberg-Hanssen and Emslie, 1988) which makes a thorough spectroscopic analysis necessary.

During maximum solar activity a dramatic increase in the number and size of solar flares is noticeable. Many flares each day can occur at the time of peak solar activity. A flare occupies only a small region of the solar surface, usually <2 arcminute square in area, but over its lifetime it can release energy ranging from 10^{28}-10^{33} ergs. Although the energy released in a single flare is negligible compared to the total energy output of the sun in the same time, flares are sufficiently localised that they show up as very intense regions in H-alpha, UV light and X-ray, and even occasionally in white light.

Unfortunately most of the radiation produced during a solar flare is blocked by the atmosphere of the earth, which mainly absorbs the high energy UV, X-ray and gamma radiation, allowing only visible light, including H-alpha, and some radio waves to reach the surface. In order to get an understanding of the physical process taking place within solar flares, all the emitted radiation should be studied.

The causes of the flaring process are still unknown, although we do know that the only energy source capable of producing the violent outbursts observed must be magnetic in nature. As the number of strong magnetic field regions appearing on the sun increases, all the energy may be released in a flash of X-ray, UV and optical radiation together with a burst of energetic electrons and protons. One of the models that explains solar flares requires the released magnetic energy to accelerate a large number of particles, which stream through the solar atmosphere, resulting in heating by frictional processes and producing X-rays by collisional bremsstrahlung. Gamma radiation may also be produced when accelerated protons collide with the ambient nuclei in the atmosphere.

Soft X-ray emission from flares, which arises in plasma at temperatures between about 2×10^6 K and 20×10^6 K, is considered to be particularly interesting for spectroscopy. The plasma responsible for this emission is also quite important from the flare energetics point of view, since a significant fraction of the total flare energy released results in soft X-ray plasma and its corresponding radiation. A flare is usually accompanied by a rapid rise in X-ray emission followed by a slower decline (impulsive and gradual phase respectively).

In flares the temperature routinely reaches 25×10^6 K. These high temperatures are attained in flux tubes of a length ranging from a few tens of arcseconds to a few arcminutes. The electron density also becomes quite high, in some cases reaching values greater than 10^{12} cm^{-3} and being typically about 10^{11} cm^{-3}. In addition to this so called thermal flare, there is a nonthermal component characterised by an electron "temperature" of $100\text{-}200 \times 10^6$ K, which is evidenced mainly by hard X-ray bursts during the rise phase of flares. The impulsive bursts are caused by a rapid acceleration of particles to very high

energies (Kev-Mev). Because of the large temperature range covered by flares their spectra are extremely important to astrophysics.

2.3.2 Solar Flare Diagnostics

Some of the most exciting results, particularly concerning flare plasmas, have been obtained in the EUV range. There are many excellent electron density diagnostics in this region. Some of the more interesting and important examples are Fe IX, Ca XVI, Ca XVII, and Fe XXI. A more detailed discussion regarding other density diagnostics can be found in Dere et al. (1979). Fe IX, is one of the most sensitive ratios for temperatures $T \approx 10^6$ K near 240 Å and has many excellent lines for deriving densities in flares. The Fe IX lines are unblended and fairly intense and will be discussed in more detail in the following Chapter. The other ions mentioned above are formed at higher temperatures. Unfortunately, diagnostic analysis become more difficult at higher temperatures because the decay rates from metastable levels increase faster than the collisional deexcitation rates as atomic number and temperature of formation increase. The highest temperature ions that are useful are Ca XVI, Ca XVII ($T \approx 6 \times 10^6$ K), and Fe XXI ($T \approx 10 \times 10^6$ K). It is evident from the presently available observations that the density in the high temperature flare plasma does not appear to exceed 10^{13} cm^{-3}. This implies, based on the atoms physics and solar abundances, that only three ions formed at temperatures greater than about 5×10^6 K will be useful density diagnostics, i.e. Ca XVI, Ca XVII, and Fe XXI. Fig. 2.8 shows a flare spectrum over the wavelength region 200-250 Å, obtained from the SO82A spectroheliograph, the two Ca XVI lines at 208.6 and 224.5 Å are distinctly noticeable.

Ca XVI is a member of the Boron-like ions formed at about 5×10^6 K, and density sensitivity occurs as for the four-level case discussed in Chapter 1 (Fig.1.2). The theoretical line ratio as a function of electron density has been calculated by Dere et al (1979) and is shown in Fig. 2.9. The atomic data for Ca XVI used for the calculation of this curve are given in the above reference. The ground state is $2s^2 2p\ ^2P_{1/2}$ (see Fig. 2.4 for energy level scheme in Boron-like ions), and the first excited state is $2s^2 2p\ ^2P_{3/2}$. At

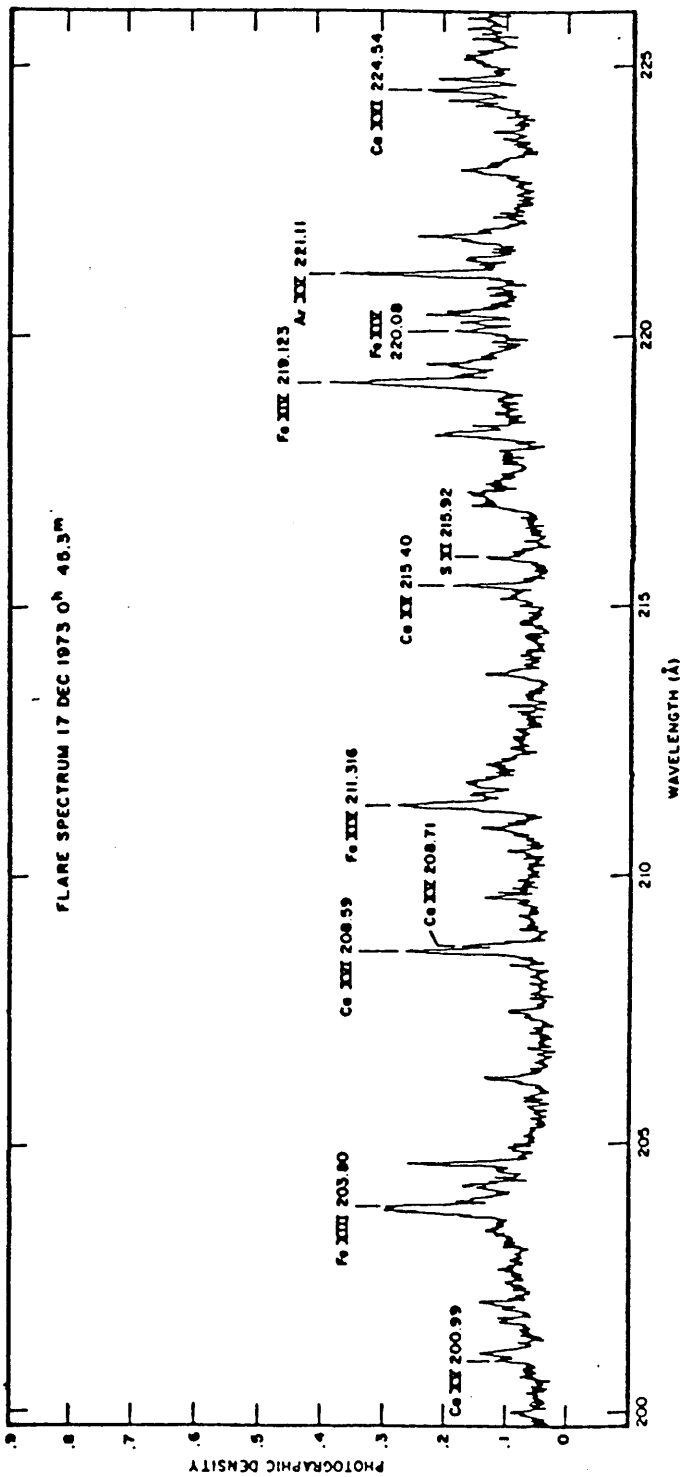

Fig. 2.8 Solar flare spectrum recorded by the NRL spectroheliograph on Skylab, of the 1973 December flare for the wavelength region 200-225 Å. (Dere et al. 1979).

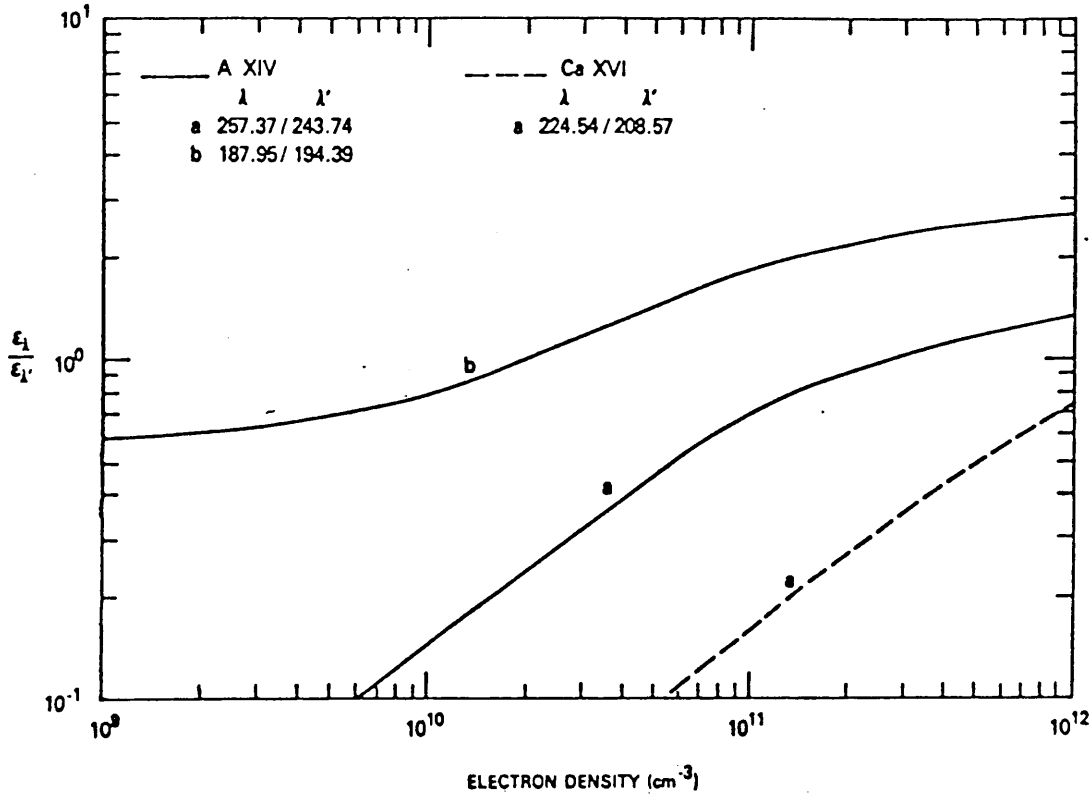

Fig. 2.9 Emission ratios as a function of electron density for the lines and ions indicated. The Ca XVI is formed at a temperature of about 6×10^6 K, and it is useful as a density diagnostic in flare plasmas. (Dere et al 1979).

low densities Ca XVI produce a strong line at 208.57 Å due to the transition, 2p $^2P_{1/2}$-3d $^2D_{3/2}$. The 2p $^2P_{3/2}$-3d $^2D_{5/2}$ line at 224.54 Å is weak because at low densities it can only be excited from the $^2p_{1/2}$ level, and the collisional rate coefficient is small. However, at high densities the $^2D_{5/2}$ level can be excited from the $^2p_{3/2}$ level, and the rate coefficient is large. The line ratio increases as the density increases and eventually reaches a high density limit when the populations of $^2p_{1/2}$ and $^2p_{3/2}$ are in the ratio of their statistical weights.

The Ca XVI lines are useful for density diagnostics in compact flares. The values of electron densities inferred from this line ratio are generally between 10^{11} and $4x10^{11}$ cm^{-3}.

The Ca XVII ion is Be-like, and is formed at slightly higher temperatures than Ca XVI. The ground state is $2s^2\ ^1S_0$, and the first excited states are $2s^2p\ ^3P_{0,1,2}$. The density sensitive diagnostic is provided by the triplet states. The $^3P_0$ state cannot decay to the ground state, while the decay rate from $^3P_2$ state to the ground is of negligible value compared with that of the $^3P_1$ level. The $^3P_1$ level can decay to the ground at a rate unaffected by collisions at solar densities. As a result, lines due to transitions of the type, $2s^2p\ ^3P$-$2p\ ^3P$, are density sensitive relative to the singlet transition $^1S_0$-$^1P_1$ at 192.82 Å. This ion was first suggested as a useful density diagnostic by Doschek et al (1977), who calculated various line ratios using available atomic data. The obtained density was about $5x10^{11}$ cm^{-3} for the intensity ratio of the transition $2s2p\ ^3P_2$-$2p2\ ^3P_2$ at 232.83 Å to the line 192.82 Å. These lines are included in the spectral region of Fig. 2.8 discussed above. The densities derived from Ca XVII lines are not in satisfactory agreement with densities deduced from other ions such as Ca XVI. Uncertainties in observational data may cause part of this contradiction.

The Fe XXI ion is a C-like ion and is formed at a temperature of $10x10^6$ K. This ion is considered to be one of the highest ions useful as a density diagnostic in solar flares. The ground state levels are $2s^22p_2\ ^3P_{0,1,2}$ and $^1D_2$, $^1S_0$. The energy level diagram showing transitions for C-like ions is shown in Fig. 2.10, taken from Raju and Dwivedi

(1979). The $^3P_2$ level is the most useful level for density sensitive lines at flare densities, because higher levels such as $2s2p^3\ ^3D_3$ can be excited from this level, whereas they cannot be strongly excited from other ground state levels. Therefore a good density sensitive ratio would be the line ($2s^22p_2\ ^3P_2$-$2s2p_3\ ^3D_3$) at 145.66 Å to ($2s^22p_2\ ^3P_0$-$2s2p_3\ ^3D_1$) at 128.73 Å, and the density dependence will be qualitatively similar to Ca XVI. The Fe XXI lines are discussed by Mason et al (1979), who give the necessary atomic data, and suggest the use of Fe XXI lines for solar flare density measurements. The Ca XVI, Ca XVII, and Fe XXI lines also produce density sensitive line ratios in the X-ray region, but again there are not many high spectral resolution observations available.

Electron density diagnostics for solar flares in the EUV wavelength region were reviewed by Dere et al. (1979) and Doschek (1985, 1988). Dere et al. have considered the wavelength region covered by the ATM-NRL-S082A spectroheliograph aboard Skylab (171-630 Å).

An interesting result (Dere et al. 1979) has been found from EUV density measurements over a very broad temperature range. The electron density in flares appears to increase with temperature, indicating that the gas pressure is not constant throughout the flare volume. The reason for this behaviour is not yet understood but presumably due to the presence of strong magnetic pressure.

Another interesting result from EUV diagnostics concerns the differential emission measure (DEM) for compact flares. Most theoretical calculations predict a temperature dependence of the DEM as approximately $\propto T^{3/2}$. However, investigations indicate an emission measure dependence of about T^3, e.g. Widing and Spicer (1980), Widing and Heiei (1984). The reason for this large difference between theory and observation is still not known. A recent paper by Widing and Cook (1987) combines electron density diagnostic ratios from this wavelength region and those from a longer wavelength region (1100-2000 Å) to provide an electron density profile for the temperature range $4x10^4$-$10x10^6$ K., Fig 2.11. They pointed out that the emission from

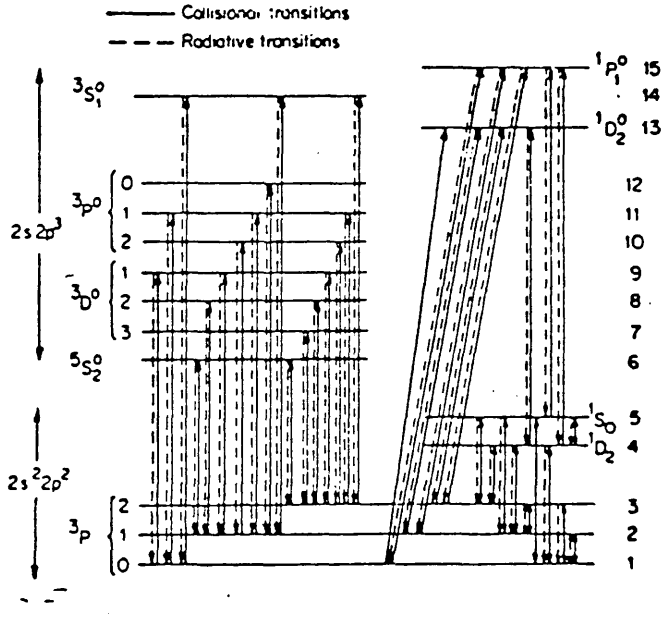

Fig. 2.10 Energy level scheme for carbon-like ions. ——— Collisional transitions; ------ radiative transitions. (Raju and Dwivedi 1979)

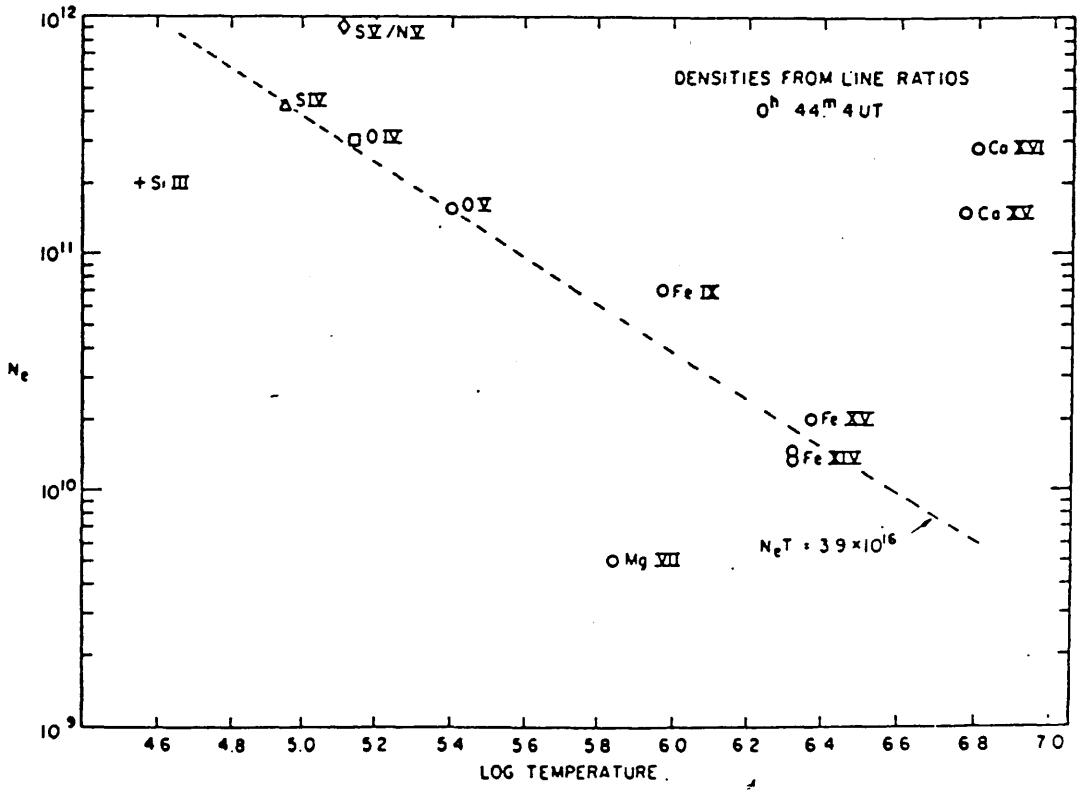

Fig. 2.11 Electron densities for a solar flare plotted against temperature obtained using lines from ATM-NRL-A and NRL-B spectra. Widing and Cook (1987).

the transition region ($T<10^6$ K) in compact flares actually arises in entire loop structures, rather than from the footpoints of high temperature regions of hotter loops. The cool loops have lower densities than the hot loops, which would explain the increase of density with temperature. The flare emission of higher temperature was emitted by a small intense kernel, while lower temperature emission was associated with a more diffuse region, with the kernel embedded at its base. The low temperature emission does not seem to be confined to the footpoints of high temperature loops as some models predicted.

Widing (1982) has pointed out that a group of lower transition region ions that emit lines in the EUV have been identified. He mentioned that new density diagnostics for the O V 192, 215, 220 Å lines have been developed and applied. It has been found that strong enhancements of these types of lines during the impulsive phase of some flares is observable , apparently during the time of hard X-ray bursts, Widing and Hiei (1984) and Widing (1982). They find that the transition region emission measure function shows an unusual flat slope a $T^{0.6}$, while being of the form T^3 for hot loops.

There also exist some other lines that have formed in the X-ray solar spectrum. In recent years SMM, P78-1 and Hinotori have provided a wealth of solar flare spectra in this wavelength region. In high temperature flares some iron lines fall between about 90 and 150 Å, such as Fe XVIII-Fe XXIII, which are interesting and important lines from the diagnostics point of view. Other groups of lines form in the range from about 1.7 to 25 Å. This wavelength range contains very useful information concerning plasma conditions in solar flares.

We discussed in the previous Chapter the importance and the possibility of utilising some of the He-like and H-like ions as density diagnostics, pointing out that they are useful for solar flare plasmas. The best examples of He-like line ratios, that are density dependent, have been observed by Aerospace Corp. SOLEX spectrometers. The first observations of a large variation in the line ratios R were from solar flare and active region observations of the He-like O VII lines recorded by these instruments (McKenzie

et al. 1980). An example of such observations is shown in Figure 2.12. It is evident in the active region spectrum that the ratio R (Z/Y) is about 2.8, indicating a value of electron density of 1.1×10^{10} cm^{-3}, cf. Fig.1.5. However, in the two flare spectra observed the ratio implied densities of 3.7×10^{10} and 1.2×10^{11} cm^{-3}. High time resolution spectra of other flares show a strong, short lived density enhancement ($n_e > 10^{12}$ cm^{-3}) coincident with the peak in the hard X-ray emission (Doschek 1981). Figs. 2.13 shows the electron density as a function of time as well as the intensity of the Ca XIX and Fe XXV resonance lines derived for the 9 May 1980 and for another flare that occurred on 8 April 1980. In both flares there was a rather rapid rise in density followed by a nearly equally rapid fall, near the time of peak fluxes in the resonance lines. In both flares the maximum density was around 10^{12} cm^{-3}. Several He-like lines and other electron density sensitive line ratios which fall into the wavelength region (10-100 Å) were reviewed by Brown et al. (1986). Fig. 2.14 shows results for spectra obtained during the decay phase of a flare. Constant electron density rather than constant pressure indicates the complexity of the structure of the flare.

Finally it should be mentioned that satellite lines are very useful for electron temperature diagnostics, which will be obtained by taking the ratio of a dielectronic satellite (e.g., line g of Fe XXIV) to a He-like or H-like resonance line (e.g., line w of Fe XXV). Some of the most important conclusions that have been obtained by applying these lines to flare spectra, have been obtained from SMM (Acton et al 1981), the P78-1 Spacecraft (Doschek et al. 1979, and Culhane 1989) and the Japanese Hinotori spacecraft (Tanaka et al. 1982).Some of the main conclusions are:

(1) The temperature for the bulk of the thermal flare plasma does not exceed about 25×10^6 K during a flare, and for smaller flares can be much less.

(2) For nearly half of the large flares, there is also a super-hot component, with a temperature of about 35×10^6 K. The emission measure of this component is much less than for the bulk of the thermal component.

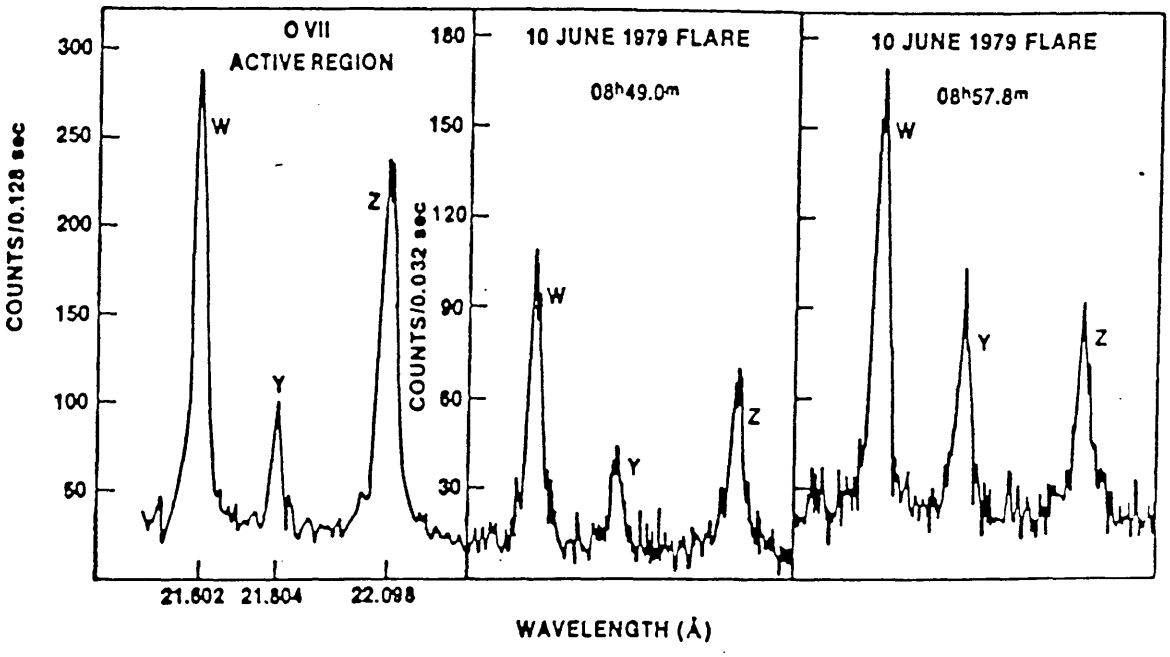

Fig. 2.12 The O VII spectra of an active region and solar flare. The ratio (z/y) is density sensitive.(McKenzie et al. 1980).

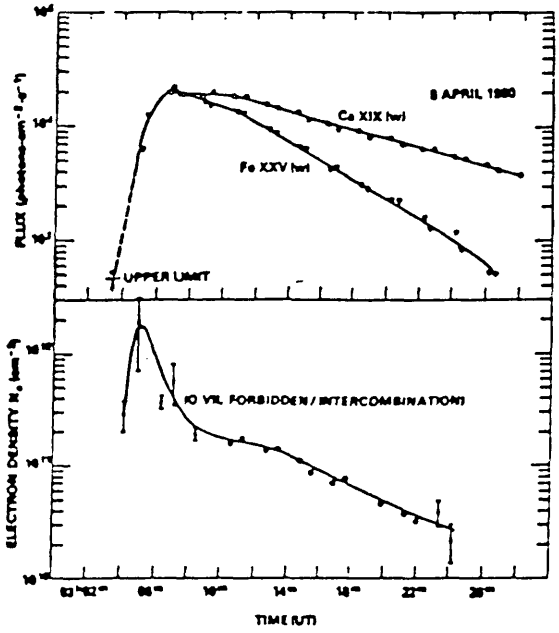

Fig. 2.13a Electron density as a function of time for 1980 April 8 flare, obtained from the O VII line ratios and of the fluxes in the Ca XIX and Fe XXV (Doschek et al. 1981).

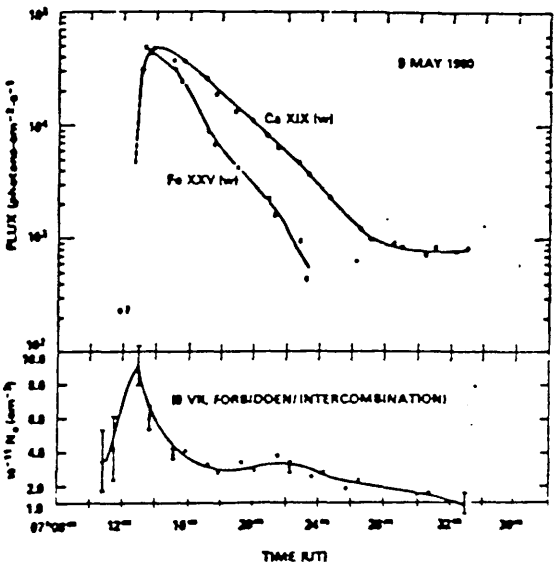

Fig. 2.13b The same as in Fig.2.13a for the 1980 May 9 flare (Doschek et al. 1981).

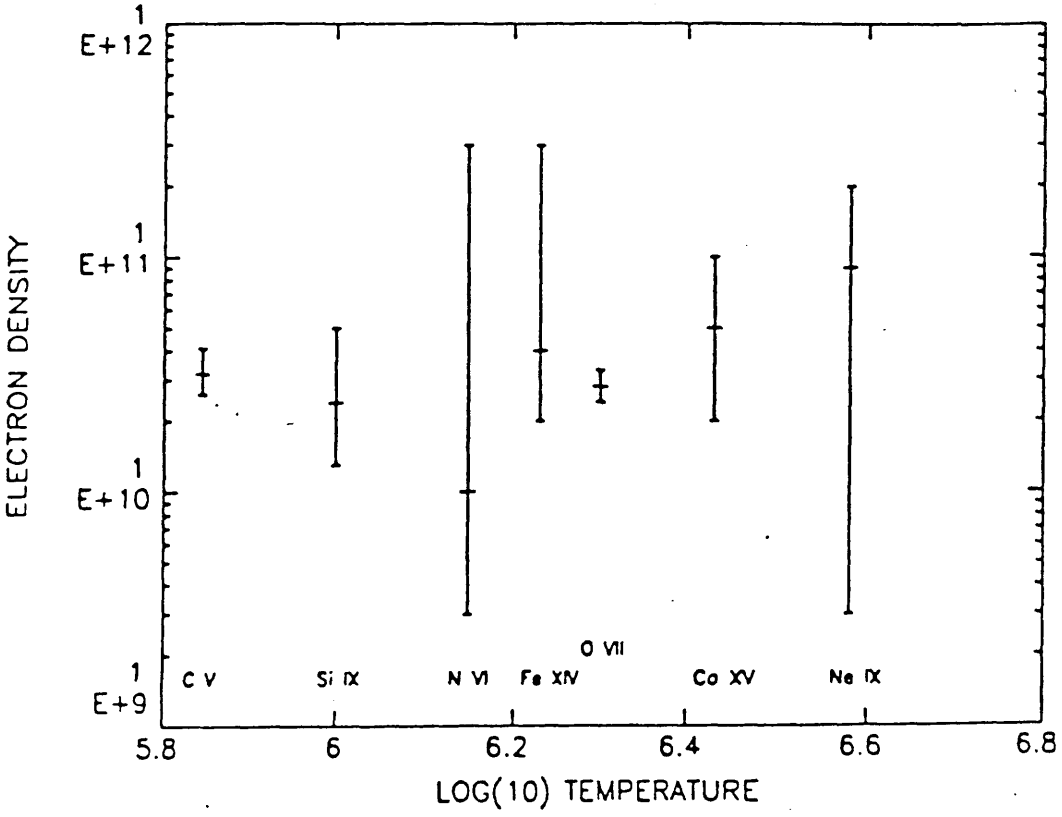

Fig. 2.14 Observed electron densities and error bars for seven diagnostic line pairs for a flare spectrum (Brown et al 1986).

(3) The temperature deduced from calcium lines (k/w ratio) averages about 3.8×10^6 K lower than the temperature deduced from the j/w iron lines, confirming the existence of a multithermal plasma, for most flares. However, the functional dependence of the emission measure with temperature near 20×10^6 K is more complicated than expected from theoretical calculations, in which the relationship is not of a power law formula, i.e. T^b.

2.4 Summary

Although much about the structure and physical conditions of the solar atmosphere is presently known, many basic problems, such as its origin and the mechanisms by which it is maintained, need to be resolved. In addition, certain problems concerning the structure of the atmosphere are still largely unsolved. Of particular importance is the fact that the atmospheric regions can not be regarded as having plane-parallel structure. The solar atmosphere is highly inhomogeneous, and it is not valid to specify a unique temperature or density at a given height above the photosphere. The exact nature and shape of the transition region structures cannot be determined with the presently obtainable spatial resolution. For example the High Resolution Telescope Spectrograph (HRTS) observations discussed by Dere et al (1987) have a spatial resolution of about 0.8"-3" covering a spectral range of 1150-1700 Å. A spatial resolution of about 0.1" is therefore required in order to unravel the true nature of the transition region, and its relationship to the chromospheric and coronal plasma.

There are several problems that can effect the determination of very accurate electron densities in the UV region. One of these problems is the existence of inhomogeneous plasmas of non-isothermal structure. Doschek et al (1977) and Widing (1982) have found that in solar flares there exist inhomogeneous plasma in which a relatively low density plasma in embedded with small high density knots, as has been shown above. Also in laboratory plasmas such as Tokamak, inhomogeneities are induced by plasma instabilities and may give a similar situation to the one mentioned above. The plasma inhomogeneity may be the main reason of producing large differences in derived densities. This fact, as well as the question of what the effect of these types of plasmas on line ratios can be, will be the main objective of Chapter 4.

Therefore, the density structure of the source should be taken into consideration when analysing solar, stellar, and laboratory spectra. These effects are particularly important in the case of analysing spectra where spatial resolution cannot be achieved, such as in stellar spectra.

CHAPTER 3

APPROXIMATE REPRESENTATION OF DENSITY SENSITIVE LINE RATIOS

3.1.Introduction

The electron density in the solar atmosphere may be derived by several different methods (cf. Chapter 1). One method which has been used extensively is that of the analysis of UV, EUV and X-ray line intensity ratios with different density dependence. The importance of electron density determination has led to the rapid development of density diagnostic techniques and also a great improvement in the efficiency and accuracy of the observational instruments. These techniques have been discussed in detail in the preceding chapters with a few specific examples given as illustration.

It should be emphasised that in these analyses it is usually assumed that the plasma under consideration is isothermal and of homogeneous structure. However, images of different plasmas of interest display a great deal of inhomogeneous structure, (cf. Chapter 2). Recent observations have revealed that the transition region, solar corona, and solar flares are extremely inhomogeneous in nature and may, in fact, be composed of many unresolved filamentary structures. The effects of such inhomogeneities of an atmosphere on the density distribution inferred from an observed line ratio must be examined. In order to do this we will derive an analytical representation of the emission rate in a spectrum line in terms of a spectroscopic mean density, $<n_e>$, discussed fully in Chapter 4, for an arbitrary distribution of electron density.

In the present chapter, we consider an approximate, analytical, representation that describes line ratios as functions of electron density, and which is found to be a good approximation to line ratios of interest. This representation is compared with some of the more commonly used specific density diagnostic examples.

3.2.General Formulation

In order to determine atomic line ratios theoretically it is generally necessary to solve the equations of statistical equilibrium for the different atomic levels in each ion, taking into account all of the important atomic processes such as collisional excitation/de-excitation and radiative decay. This non-trivial calculation involves large quantities of

atomic data and much computer time. In this section we will show how a simple analytical expression, to represent the various diagnostic line ratios, can be derived for important simple cases and that the same functional form is a good empirical parametric fit to more complex cases.

The general form of the power p emitted per unit volume in a particular line (denoted by α), from an optically thin plasma of volume V, is given by,

$$P_\alpha(n_e) = h\nu_{21} n_2 A_{21} \tag{3.1}$$

where $h\nu_{21}$ is the energy of the transition between the upper level 2 and the lower level 1, A_{21} is the spontaneous radiative decay rate, and n_2 is the number density in the excited level.

In the case of a two level atom for which the excited level is metastable, we can write the detailed balance equation (Equation 1.4) to find n_2 as

$$n_2 = \frac{n_1 n_e C_{12}}{A_{21} + n_e C_{21}} \tag{3.2}$$

Let n_{ion} be the total number density of the ion, then

$$n_{ion} = n_1 + n_2 \tag{3.3}$$

therefore equation (3.2) may be rewritten as

$$n_2 = \frac{n_e n_{ion} C_{12}}{A_{21} + n_e (C_{21} + C_{12})} \tag{3.4}$$

From equations (3.1) and (3.4) the power in a spectral line can be expressed as

$$P_\alpha (n_e) = h\nu_{21} \frac{n_e n_{ion} C_{12}}{1 + \frac{n_e (C_{21} + C_{12})}{A_{21}}} \tag{3.5}$$

n_{ion} may conveniently parametrised as $n_{ion} = \frac{n_{ion}}{n_{el}} \frac{n_{el}}{n_H} \frac{n_H}{n_e} n_e$, then (3.5) becomes

$$P_\alpha(n_e) = h\nu_{21} \frac{C_{12} \frac{n_{ion}}{n_{el}} \frac{n_{el}}{n_H} \frac{n_H}{n_e} n_e^2}{1 + \frac{n_e (C_{21} + C_{12})}{A_{21}}} \qquad (3.6)$$

On denoting

$$K_\alpha = \frac{n_{ion}}{n_{el}} \frac{n_{el}}{n_H} \frac{n_H}{n_e} h\nu_{21} C_{12} \qquad (3.7)$$

and

$$n_\alpha = \frac{A_{21}}{(C_{12} + C_{21})} \qquad (3.8)$$

equation (3.5) takes the form

$$P_\alpha(n_e) = K_\alpha \frac{n_e^2}{(1 + \frac{n_e}{n_\alpha})} \qquad (3.9)$$

where K_α is a measure of the power emitted at low density where the radiative decay is dominant, and is a known constant for any given line. The value of K_α depends on the atomic data, the temperature adopted and the element abundance, but is independent of the electron density, n_e. In equation (3.9), n_α is a measure of the density sensitivity range of n_e at which collisional deexcitation becomes important.

The line ratio of the emissivity of two lines (α_1, α_2), at an electron density n_e can then be given as

$$R_{12}(n_e) \equiv \frac{P_{\alpha 1}(n_e)}{P_{\alpha 2}(n_e)} = \frac{K_{\alpha 1}}{K_{\alpha 2}} \frac{1 + n_e / n_{\alpha 2}}{1 + n_e / n_{\alpha 1}} \qquad (3.10)$$

Which, on writing $R_\alpha = K_{\alpha 1}/K_{\alpha 2}$, $n_\alpha = n_{\alpha 1}$, and $\Lambda_\alpha = n_{\alpha 2}/n_{\alpha 1}$, becomes

$$R_{12}(n_e) = R_\alpha \frac{1 + n_e / n_\alpha \Lambda_\alpha}{1 + n_e / n_\alpha} \qquad (3.11)$$

We will denote this expression for R_{12} as 'the reciprocal representation'. The parameters (R_α, Λ_α, n_α) are constants which characterise the line ratio curve. Whether $\Lambda_\alpha > 1$ or $\Lambda_\alpha < 1$ indicates which of the two cases, mentioned in Chapter 1, is being considered, since most of the density sensitive line ratios fall into one or the other of the two general

cases. (In either case density sensitivity arises because at sufficiently high densities collisional de-excitations can compete with the radiative decay in depopulating the metastable level). The first case is the one for which the metastable level is in an excited configuration. The intensity of the line arising from this level *decreases* relative to a line which is unaffected by collisional processes (cf. Fig.1.1), this situation being represented by equation 3.11 with $\Lambda_\alpha>1$. The second case is the one in which the line excited from a metastable level in the ground configuration *increases* relative to a collisionally independent line (cf. Fig. 1.2) and corresponds to $\Lambda_\alpha<1$ in equation 3.11.

In what follows, we will represent the behaviour of the line ratio R, as a function of electron density, by equation (3.11) and discuss the comparison of this analytical representation with the more complex multi-level calculations for each of the cases discussed above.

3.3 Application 1: Ions for which R decreases with n_e ($\Lambda_\alpha>1$)

As an illustrative example, Fe IX, which is one of the Ar-like ions, has been adopted to demonstrate this case. Fe IX is a very important ion for diagnosing EUV spectra, which are formed in the quiet sun corona, and has been discussed in detail by Feldman et al. (1978). This ion is formed in the temperature region of the low solar corona ($T\approx9\times10^5$ K), the region where Fe IX is of maximum abundance. Atomic data for Fe IX have been obtained by Flower (1977).

The ground state of this ion is $3s^23p^6\ ^1S_0$ and the first three excited states are $3p^53d\ ^3P_{0,1,2}$ as shown in Fig.3.1. The pertinent transitions for our discussion are $^3P_2$-$^1S_0$ at 241.911 Å, and $^3P_1$-$^1S_0$ at 244.739 Å, since the density sensitivity of the ratio of these lines is caused by metastable levels in the excited configuration. The transition from $^3P_1$ to $^1S_0$ is an electric dipole with a radiative decay rate of 9.3×10^6 s^{-1}. While the transition of $^3P_2$ into the ground state $^1S_0$ is a magnetic quadrupole with a very small radiative decay rate, only 71 s^{-1}. Note that the $^3P_2$ can also decay to $^3P_1$ level (a magnetic dipole transition) with a rate of 2.1 s^{-1}, which is not significant compared to the quadrupole rate. Other transitions include the j=0 to j=0 which is strictly forbidden and

therefore not be included in our discussion. At low densities both excited levels, $^3P_2$ and $^3P_1$, are populated primarily from the ground state, and collisional deexcitation is not effective at this stage. The calculated intensity ratio 241.911 Å/244.739 Å is about 5:3, approximately the ratio of the excitation rate coefficients, which is proportional to the ratio of the statistical weights of the levels. However, at higher densities collisional de-excitations from $^3P_2$ to the $^3P_1$ and $^1S_0$ levels begin to compete with the spontaneous radiative decay in depopulating the level $^3P_2$. As a result the ratio 241.911 Å/244.739 Å starts to decrease.

In order that our representation may be compared with the higher level theoretical calculations we require to best fit values for the parameters (Λ_α, R_α, n_α). For a given line ratio curve, produced numerically, we can find the relevant values of R_α and Λ_α from the asymptotic line ratios as the electron density tends to zero and infinity respectively (cf. 3.11). The determination of the final parameter, n_α, is a little more complicated. By using a best fit procedure to the published line ratios ('weighted least square', wle) we find the optimum value of n_α which reproduces the line ratio curves. Our best fit criterion is governed by minimising the parameter

$$\text{wle} = \sum_j \left(\frac{R_{tj} - R_{cj}}{R_{cj}}\right)^2 \qquad (3.12)$$

where R_t is the true line ratio, obtained from Fig. 3.1, R_c is the calculated line ratio and j runs over all n_e values.

As an example we use the results of Feldman et al. (1978). The appropriate representation parameters are shown in Table 3.1. n_α is obtained with a minimum wle of 0.07 where wle is governed by equation (3.12). This is shown graphically in Fig. 3.2. This procedure has been applied to many different density sensitive line ratios and we find that it is always possible to reproduce the numerical curves very well.

Some examples and applications of our representation to an observed value for Fe IX lines can be given. For example, the observation of Fe IX in the flare loop of 21

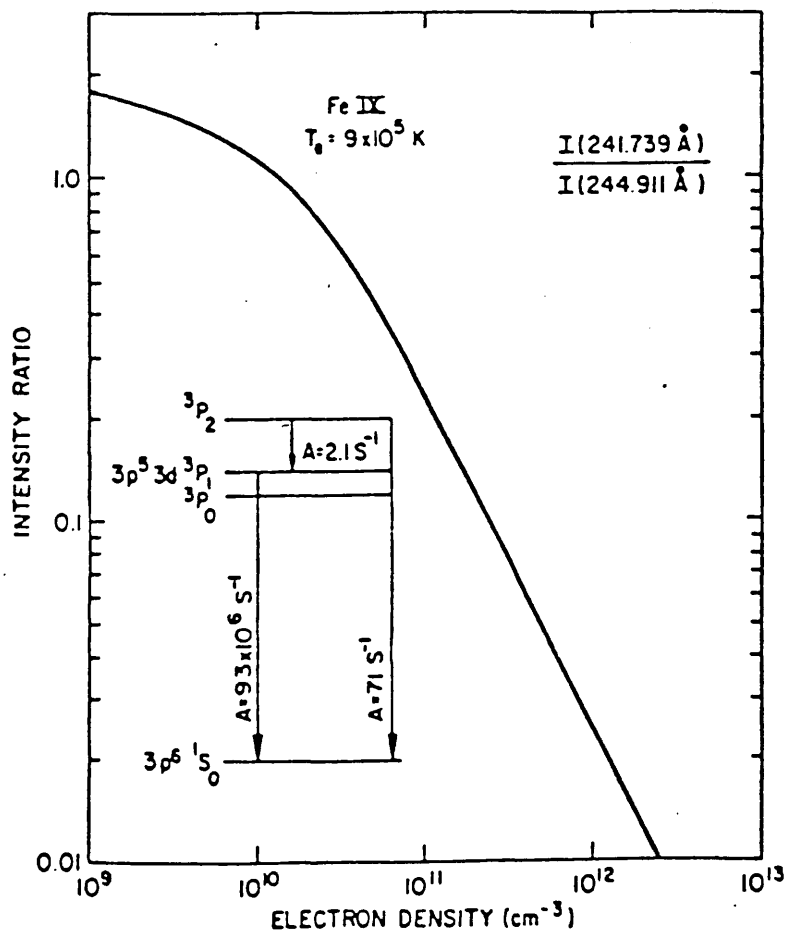

Fig. 3.1 Density sensitive line ratio for Fe IX (Feldman 1978).

Table 3.1

Representation parameters (Feldman et al. 1978)

Parameters	For Fe IX (λ 241.739Å/λ 244.91Å)
T (K)	9.0×10^5
$n_\alpha(cm^{-3})$	1.312×10^{10}
R_α	1.76
Λ_α	176

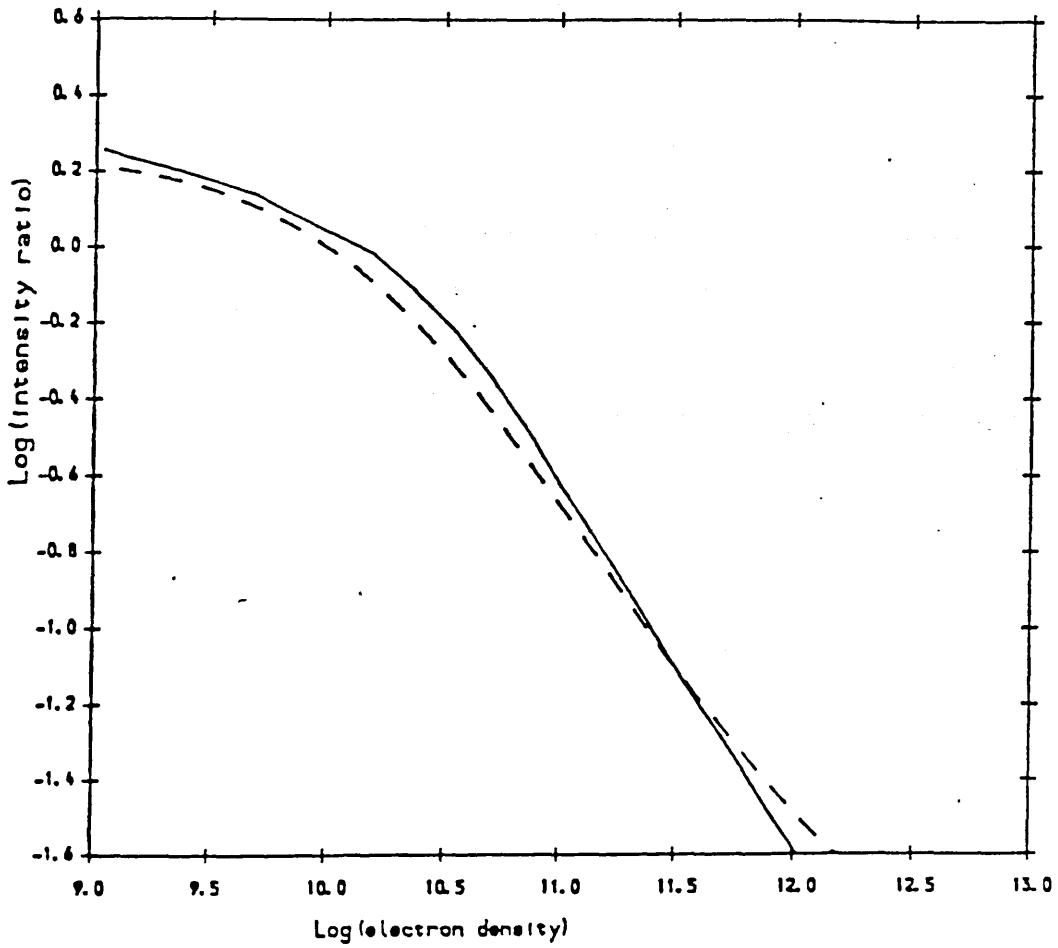

Fig. 3.2 Intensity ratio R as a function of density n_e for the line pair 241.911 Å/244.739 Å of Fe IX. The solid curve is taken from Feldman et al. 1987 while the dashed curve is the fit of the reciprocal form of equation (3.11) for the parameters given in table (3.1).

January 1974 produced a line ratio of 0.125 (Feldman et al. 1978). This line ratio corresponds to a density which can be inferred utilising our representation, viz .

$$n_e = 1.312 \times 10^{10} \frac{\frac{0.125}{1.76} - 1}{\frac{1}{176} - \frac{0.125}{1.76}} = 1.86 \times 10^{11}\ cm^{-3}$$

3.4.Application 2: $\Lambda_\alpha<1$

In the preceding section we discussed the possibility of utilizing a simple analytical approximation in order to represent the numerically calculated line ratio curves. The application of this representation to the cases where R decreases with increasing density ($\Lambda_\alpha>1$), was very encouraging and shows very good results. In this section we investigate the other situation in which the line ratio increases with increasing density, $\Lambda_\alpha<1$.

For this case we have chosen one of the boron like ions. O IV (1400 Å) is considered to be one of the ions that has most accurate atomic data and most accurate observational data and has been studied more intensively than any ion in the sequence. (Doschek 1984). The O IV intersystem lines are density sensitive because they arise from metastable levels, as has been shown in the two previous sections. This ion is one of the ions in 1100-2000 Å region which is particularly important for plasma diagnostics of the lower transition region. The atomic data were obtained from Flower and Nussbaumer (1975c), and Hayes (1982, 1983).

The density diagnostic in this ion arises due to the dependence of the fine structure levels of the ground $2s^22p\ ^2P$ term and the metastable level $2s2p^2\ ^4P$ (see Fig. 3.3). The intersystem line between $2s^22p\ ^2P_{3/2}$ and $2s2p^2\ ^4P_{5/2}$ occurs at 1401.156 Å, $2s^22p\ ^2P_{3/2}$ and $2s2p^2\ ^4P_{3/2}$ at 1404.81 Å, $2s^22p\ ^2P_{3/2}$ and $2s2p^2\ ^4P_{1/2}$ at 1407.386, and $2s^22p\ ^2P_{1/2}$ and $2s2p^2\ ^4P_{1/2}$ at 1399.77 Å.

The density sensitivity in this case is similar to the 4-level atom explained in Chapter 1, in which two intersystem lines have been considered. In the low density limit,

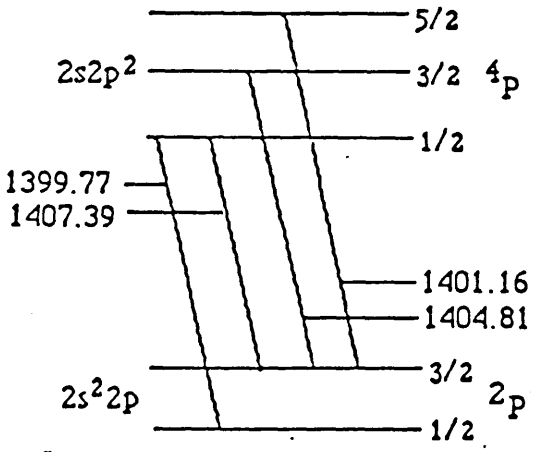

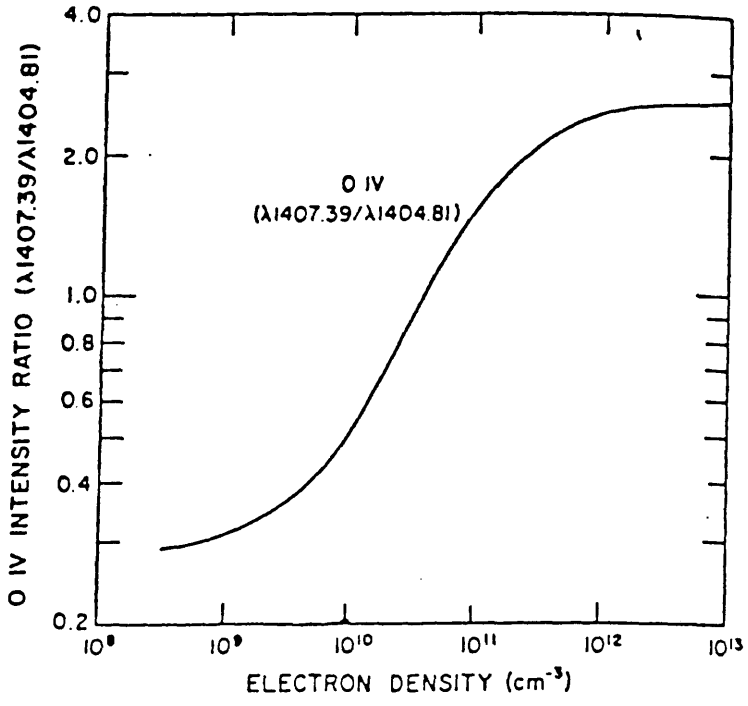

Fig. 3.3 Density sensitive line ratio for O IV (Doschek 1984).

the ratio of the two lines is proportional to the ratio of the collision rates. At the high density limit the intensity ratio is proportional to the ratio of the transition probabilities. Note that A_{21} for the transition that produces the line 1407 Å is greater than that of 1405 Å, therefore the ratio of the above lines does increase with increasing density. The variation of R with density for the O IV 1407 Å/ 1405 Å ratio is shown in Figure (3.4).

The empirical reciprocal representation R_{12} (Equation 3.11), is shown in Fig. 3.4 and we see that it agrees very well with the actual values obtained from the more detailed spectroscopic calculations. The values of the different parameters required in (3.11) are indicated in Table 3.2.

As an example of the accuracy of this representation in obtaining electron density from an observed line ratios for O IV 1407Å/1405Å can be given as follow. The observation of the above O IV line ratio from a surge observed above the limb was of the order of 0.9 (Doschek 1984). This line ratio corresponds to a density, obtained from our representation, of

$$n_e = 8.738 \times 10^{10} \frac{\frac{0.9}{0.3} - 1}{\frac{1}{0.115} - \frac{0.9}{0.3}} = 3.06 \times 10^{10} \text{cm}^{-3}$$

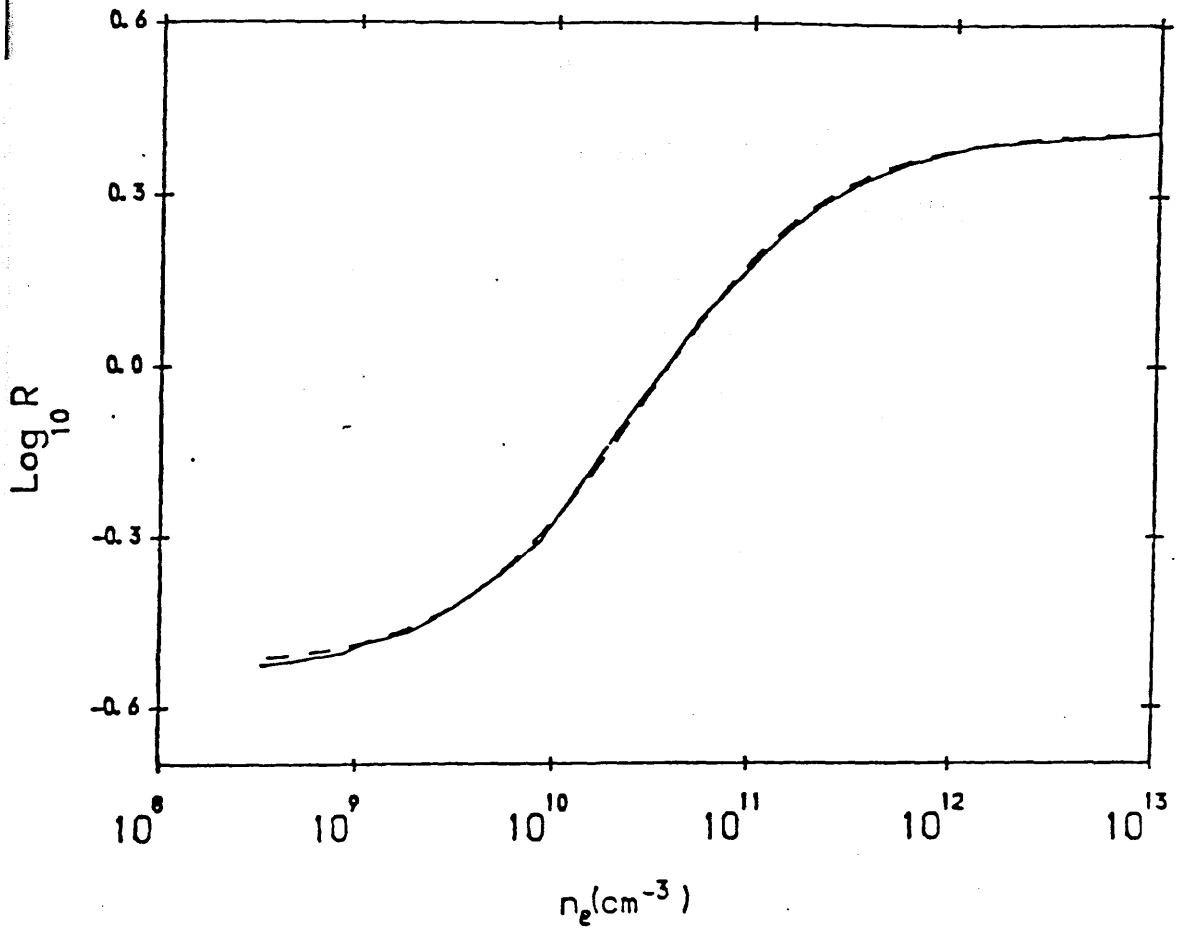

Fig. 3.4 Intensity ratio R as a function of density n_e for the line pair 1407.39 Å/1404.81 Å of O IV. The solid curve is taken from Doschek. 1984 while the dashed curve is the fit of the reciprocal form of equation (3.11) for the parameters given in table (3.2).

Table 3.2

Representation parameters (Doschek et al 1984)

Parameters	For O IV (l 1407.39/l 1404.81)
T (K)	1.3×10^5
$n_\alpha (cm^{-3})$	8.738×10^{10}
R_α	0.3
Λ_α	0.115

3.5.Conclusion

In this Chapter we have presented a simple but accurate analytical representation that can be utilised in studying solar plasmas and investigating the structure of the different sources. It has been shown (Figs. 3.2, 3.4) that the ratio of a pair of spectral lines which is a function of electron density can be represented closely by a simple analytical expression (Equation 3.11). This simple form is found to lead to extremely good representations of actual line ratio curves, obtained by numerical methods which require very accurate atomic data and much theoretical effort. The use of our analytical representation reduces considerably the effort involved while still retaining a large degree of accuracy. It is therefore an excellent method for electron density determination in solar plasmas allowing a more flexible treatment of the effects of the inhomogeneities on density sensitive line ratios. This will be discussed in great detail in the following Chapters.

CHAPTER 4

ISOTHERMAL PLASMA OF INHOMOGENEOUS STRUCTURE

4.1. Introduction

The inference of plasma temperature T and density n_e structure from spectral line ratios is a problem of universal importance for both laboratory and astrophysical plasmas. In the preceding Chapters we have discussed the basic principles behind the density and temperature diagnostic analysis of line ratios and reviewed the many investigations made in this field.

In many of these studies the emitting plasma is assumed to be homogeneous. However, in practice, almost all plasmas of interest are inhomogeneous, at least in the sense of possessing large scale T and n_e gradients (e.g. the solar transition region and corona and solar flares as discussed in Chapter 2). Furthermore, spectral observations are almost always, by necessity, of extended plasma volumes, whether over the entire plasma or over the line of sight volume in an image pixel. It is therefore necessary to understand how to interpret single spectral line ratio measurements of T or n_e in terms of 'mean' plasma values and ideally to develop a methodology to extract maximal information, from a series of line ratios, on the spatial distribution of T and n_e which directly govern, for example, energy transport in the plasma. In the case of temperature diagnostics from, for example, pairs of resonance lines, this methodology has been quite thoroughly developed, particularly in the case of solar plasmas (cf. Chapter 2). Specifically, the ratios of such line pairs with different temperature sensitive ranges permits inference of the plasma emission measure ($\int n_e^2\, dV$) per unit T range (e.g. Dere and Mason 1981, Craig and Brown 1976, 1986). These analyses are usually based on the assumption of steadystate ionisation balance where the temperature varies relatively slowly with time. Since this differential emission measure function involves the distribution of both n_e and T, the spatial distributions of T, n_e separately can only be arrived at via some assumed relationship between T and n_e, such as constant pressure. Ideally what is wanted is a means of separately inferring the distribution using density sensitive line ratios (e.g. intersystem lines or intersystem to allowed lines).

The methodology for interpreting density sensitive line ratios from inhomogeneous plasmas has received comparatively little attention to date, compared to the temperature distribution problem. The fact that solar plasmas are certainly inhomogeneous in density has been clearly demonstrated by the fact that different line ratios lead to different values of the 'mean' density from the same solar source as shown in Chapter 2, (e.g. Doschek 1984, Doschek et al. 1977, Widing 1982, Feldman et al. 1977, Nussbaumer et al. 1982 and Feldman and Doschek 1978). Doschek (1984) has investigated this effect for the special case of a plasma which is isothermal but which comprises two distinct spatial regions one of low and one of high density (both uniform). The main conclusion of his work is that the presence of a small fraction of the plasma, by mass or volume, at high density can (because of its large emission measure) lead to a 'spectroscopic mean' density, inferred from a single density sensitive line ratio, much higher than the volumetric mean density (total N_e/total volume).

In this Chapter we consider the basic problem of interpreting density sensitive line intensities from an inhomogeneous plasma in more general terms than Doschek, by considering arbitrary density distributions but still restricting the analysis to isothermal situations. We first (Section 4.2) show how the problem can be considered as that of determining a plasma emission measure $\zeta(n_e)$ differential in density n_e, and how any single line ratio yields a 'spectroscopic mean' (equivalent homogeneous) density $\langle n_e \rangle$; this is a single weighted moment of $\zeta(n_e)$ and differs from one line pair to another and also from the volumetric mean density. We then utilise the derived representation of the density sensitivity of line strengths (cf. Chapter 3), and illustrate some aspects of the problem for a specific (exponential atmosphere) plasma model (section 4.4). In section 4.5, we return to the general problem showing that for a single line ratio, a homogeneous $n_e(\underline{r})$ solution yields a minimum possible plasma volume, consistent with the ratio. We then discuss how the use of more and more line ratios leads, in principle, to an ever closer estimate of the true inhomogeneous structure of the plasma in terms of $\zeta(n_e)$, and of its true total volume.

4.2. Definition of the problem

For an optically thin plasma of electron density $n_e(\underline{r})$, temperature $T(\underline{r})$ at position $\underline{r}$ in a volume V, the total power P_α emitted in a spectrum line α (derivable from the observed line flux) can be written

$$P_\alpha = \iiint_V n_e^2(\underline{r})\, F_\alpha(n_e, T)\, d^3\underline{r} \qquad (4.1)$$

where $F_\alpha(n_e,T)$ incorporates an element abundance factor as well as details of the transition processes determining the level populations and emission rate. In this Chapter we will concern ourselves only with volumes V in which T is uniform but with $n_e(r)$ varying, in order to isolate the effect of the latter. In the plasma as a whole, such a situation can exist only if gravity or a magnetic pressure gradient exists to balance the gas pressure gradient or if the plasma is in a transient hydrodynamic state. (We consider an example of the case of gravitational balance in Section 4.4). In practice the situation may also be approximated diagnostically by chosing to study only lines formed over a narrow temperature range in which case our analysis will only refer to the subvolumes V of the plasma in that range. We will also assume that T is known either by choice of lines, or from resonance line intensity ratios. The effect of a non-uniform T will be discussed in the following Chapter.

With these assumptions we can set $F_\alpha(n_e,T)=G_\alpha(n_e)$ in (4.1) and write

$$P_\alpha = \iiint_V n_e^2(\underline{r})\, G_\alpha(n_e)\, d^3\underline{r} \qquad (4.2)$$

In this Chapter we will be concerned with what can be learnt about the function $n_e(\underline{r})$ from data on P_α for different lines α. Clearly to provide any distinct information the functions $G_\alpha(n_e)$ must differ in functional form and not just by a scale factor. On the other hand, even data on P_α for an infinite series of distinct lines α can never, even in principle, allow recovery of the function $n_e(\underline{r})$ of three spatial coordinates without any geometric information or assumption. In this regard the problem is precisely analogous to that of studying temperature structure by means of resonance line temperature sensitivity

(for which F_α in (4.1) depends on T only). Following the discussion of that problem by Craig and Brown (1976), it can be seen that the essence of the density problem can be expressed as that of determining, from a series of P_α's, the emission measure $\zeta(n_e)$ differential in density. $\zeta(n_e)$ is then defined by partitioning V into surfaces S_{ne} of constant density and by writing

$$dV = \frac{dS_{ne} dn_e}{|\nabla n_e|} \tag{4.3}$$

and

$$\zeta(n_e) = \iint_{S_{ne}} \frac{n_e^2(\underline{r})\, dS_{ne}}{|\nabla n_e|} \tag{4.4}$$

so that (4.2) becomes

$$\int_0^\infty \zeta(n_e) G_\alpha(n_e)\, dn_e = P_\alpha \tag{4.5}$$

The central issue is then the inverse problem of determining how much we can learn about $\zeta(n_e)$ from measurements P_α. Clearly a single line flux depends on the absolute magnitude of ζ so that to learn anything about the n_e distribution of ζ requires at least two lines (1, 2). Let R_{12} be the ratio of the observed intensities of a pair of lines (1, 2). Then

$$R_{12} = \frac{P_{\alpha 1}}{P_{\alpha 2}} = \frac{\int_0^\infty \zeta(n_e)\, G_{\alpha 1}(n_e)\, dn_e}{\int_0^\infty \zeta(n_e)\, G_{\alpha 2}(n_e)\, dn_e} \tag{4.6}$$

in the case of a plasma of uniform density n_0 ($\zeta(n_e) = \zeta_0\, \delta(n_e - n_0)$ with δ the delta-function), (4.6) implies

$$R_{12} = g_{12}(n_0) = \frac{G_1(n_0)}{G_2(n_0)} \tag{4.7}$$

from which n_0 can be inferred from

$$n_0 = g_{12}^{-1}(R_{12}) \tag{4.8}$$

where g_{12}^{-1} is the inverse function of g_{12}, n_0 being unique provided $g_{12}(n_0)$ is monotonic, as is the case for all density sensitive line ratios of interest.

In the case of a non-uniform density plasma, (4.8) can still be applied (and commonly is applied) to a line ratio measurement, to yield an effective spectroscopic mean density of the plasma for that line pair, viz.

$$\langle n_e \rangle_{12} = g_{12}^{-1}(R_{12}) = g_{12}^{-1}\left[\frac{\int_0^\infty \zeta(n_e)\, G_1(n_e)\, dn_e}{\int_0^\infty \zeta(n_e)\, G_2(n_e)\, dn_e}\right] \qquad (4.9)$$

This is the density of a homogeneous plasma which would give the same line ratio R_{12} as the real plasma, for that particular line pair. Obviously the value of $\langle n_e \rangle_{12}$ will depend not only on $\zeta(n_e)$ but on the forms of G_1, G_2 so that a series of line pair measurements will in general give a series of differing $\langle n_e \rangle_{12}$ values unless the plasma is in fact homogeneous. Qualitatively, the spread in $\langle n_e \rangle_{12}$ values found between line pairs will be an indication of the degree of inhomogeneity in the plasma density. In this Chapter we explore the extent to which this information on inhomogeneity can be quantified, i.e. what can be determined about $\zeta(n_e)$. In some of our analysis it is feasible to establish results for general forms of the G_1, G_2 functions but for some purposes we require a specific representation of the G's, which we discussed in the previous Chapter. We then illustrate the effect of inhomogeneity on $\langle n_e \rangle_{12}$ for this representation by considering the particular case of an exponential atmosphere (Section 4.4). In doing so we will compare the $\langle n_e \rangle_{12}$ values with other mean density values of physical importance viz the volumetric mean density (related to the plasma mass) given by

$$\bar{n}_e = \frac{1}{V}\iiint_V n_e(\underline{r})\, d^3\underline{r} = \frac{1}{V}\int_0^\infty \frac{\zeta(n_e)}{n_e}\, dn_e \qquad (4.10)$$

and the emission mean density (related to resonance line intensities) given by

$$\tilde{n}_e = \left[\frac{1}{V}\iiint_V n_e^2(\underline{r})\, d^3 r\right]^{1/2} = \left[\frac{1}{V}\int_0^\infty \zeta(n_e)\, dn_e\right]^{1/2} \qquad (4.11)$$

Comparison of (4.9), and (4.11) shows that use of $<n_e>$ or of $\tilde{n}_e$ will always tend to give a 'mean' density weighted toward higher values than $\overline{n_e}$ due to the proportionately larger contribution of higher densities to emission measure per unit volume. This was indeed found by Doschek (1984) in his discussion of a plasma comprising two uniform regions, one of high and one of low density.

Following our discussion of the exponential atmosphere in terms of the 'forward' predictive approach we will then consider the inverse problem in terms of what constraints and information are obtainable on $\zeta(n_e)$ from one or more line ratios.

4.3.Representation of the density sensitivity

Spectral line intensities can be used to determine the physical parameters of the plasma, e.g. electron density. These diagnostic lines has been discussed in Chapter 1 and illustrated by some specific examples.

In Chapter 3 we presented an approximate analytical representation, (Equation 3.11), which may be used for the analysis of electron density diagnostics. Some examples were shown which approximated very well to some published curves. In terms of this representation an analytic expression is obtainable for the spectroscopic mean density as follows:

In general, for a pair of lines (1, 2) we have, from (4.6), (3.6) and (3.10)

$$R_{12} = R_\alpha \int_0^\infty \frac{\zeta(n_e)\, dn}{1 + n_e / n_\alpha} \Big/ \int_0^\infty \frac{\zeta(n_e)\, dn_e}{1 + n_e / \Lambda_\alpha n_\alpha} \qquad (4.12)$$

while for a homogeneous plasma at density $<n_e>$

$$R_{12} = R_\alpha (1 + <n_e> / \Lambda_\alpha n_\alpha) / (1 + <n_e> / n_\alpha) \qquad (4.13)$$

Equating these two expressions, we can thus solve for the spectroscopic mean $<n_e>$ for this line pair for any specific $\zeta(n_e)$, viz.

$$< n_e > = n_\alpha \left[\frac{\int_0^\infty \frac{\zeta(n_e)\,dn_e}{1+n_e/\Lambda_\alpha n_\alpha} - \int_0^\infty \frac{\zeta(n_e)\,dn_e}{1+n_e/n_\alpha}}{\int_0^\infty \frac{\zeta(n_e)\,dn_e}{1+n_e/n_\alpha} - \frac{1}{\Lambda_\alpha}\int_0^\infty \frac{\zeta(n_e)\,dn_e}{1+n_e/\Lambda_\alpha n_\alpha}} \right] \qquad (4.14)$$

It is convenient to express this in dimensionless form by defining dimensionless densities

$$\nu = n_e / n_\alpha \,, \quad < \nu > = < n_e > / n_\alpha \qquad (4.15)$$

and a dimensionless (fractional) emission measure $\eta(\nu)$ per unit ν, such that

$$\int_0^\infty \eta(\nu)\, d\nu = 1, \qquad \text{viz:}$$

$$\eta(\nu) = \zeta(n_e) \Big/ \int_0^\infty \zeta(n_e)\, dn_e \qquad (4.16)$$

then (4.14) becomes.

$$< \nu > = \left[\frac{\int_0^\infty \frac{\eta(\nu)\,d\nu}{1+\nu/\Lambda_\alpha} - \int_0^\infty \frac{\eta(\nu)\,d\nu}{1+\nu}}{\int_0^\infty \frac{\eta(\nu)\,d\nu}{1+\nu} - \frac{1}{\Lambda_\alpha}\int_0^\infty \frac{\eta(\nu)\,d\nu}{1+\nu/\Lambda_\alpha}} \right] \qquad (4.17)$$

which depends only on Λ_α. It should be noted, however, that in determining <ν> from an observed line ratio R_{12}, the values of R_α and n_α must also be known.

4.4 Illustrative diagnosis of an exponential atmosphere model

A particularly simple case of density inhomogeneity in a radiating source is that of a plane stratified slab of horizontal area S and total height H (hence volume V=SH), in which the density varies with height z according to

$$n_e(z) = n_0\, e^{-z/h} \qquad , 0 \le z \le H \qquad (4.18)$$

where h is a constant scale height. This description approximates well to the distribution of an isothermal gas column in hydrostatic equilibrium under gravity, such as the limb of a hot solar loop. If $n_1 = \alpha\, n_0$ is the density at the top of the slab (z=H) then

h=H/(ln(1/α)) and we can parametrise the density distribution by (S, H, n_0, α). In terms of these, the differential emission measure is, by (4.4)

$$\zeta(n_e) = \frac{S H}{\ln (1/\alpha)}\, n_e \quad , \alpha \le n_e / n_0 \le 1 \tag{4.19}$$

while the total emission measure is

$$\zeta_{tot} = \frac{S H n_0^2}{2 \ln (1/\alpha)} (1-\alpha^2) \tag{4.20}$$

and the volumetric and emission mean density are, using(4.10), and (4.11)

$$\bar{n} = \frac{n_0(1-\alpha)}{\ln (1/\alpha)} \tag{4.21}$$

and

$$\tilde{n} = \frac{n_0 (1-\alpha^2)^{1/2}}{(2 \ln (1/\alpha))^{1/2}} \tag{4.22}$$

For observations of a particular line pair from a structure of this form, (satisfying the representation of Section 4.3), with density sensitivity parameters n_α, R_α and Λ_α, we write (4.20) as (cf. (4.15))

$$\eta(\nu) = \frac{2}{1-\alpha^2} \frac{\nu}{\nu_0^2} \tag{4.23}$$

where $\nu = n_e/n_\alpha$ and $\nu_0 = n_0/n_\alpha$. Thus by (4.16) the inferred spectroscopic mean density for this pair is,

$$<\nu> = \frac{<n_e>}{n_\alpha} =$$

$$\frac{(\Lambda_\alpha - 1)(1-\alpha)\nu_0 + \ln[(1+\nu_0)/(1+\alpha\nu_0)] - \Lambda_\alpha^2 \ln[(\Lambda_\alpha+\nu_0)/(\Lambda_\alpha+\alpha\nu_0)]}{\Lambda_\alpha \ln[(\Lambda_\alpha+\nu_0)/(\Lambda_\alpha+\alpha\nu_0)] - \ln[(1+\nu_0)/(1+\alpha\nu_0)]} \tag{4.24}$$

and, in the same units,

$$\bar{\nu} = \frac{\nu_0 (1-\alpha)}{\ln (1/\alpha)} \quad , \tilde{\nu} = \frac{\nu_0 (1-\alpha^2)^{1/2}}{[2\ln(1/\alpha)]^{1/2}} \qquad (4.25)$$

In Fig.4.1 we show $\bar{\nu}$ and $\tilde{\nu}$ as functions of ν_0 for various α values, while in Figs.4.2 we show $\langle\nu\rangle$ versus ν_0, for a range of α values, for two values of Λ_α corresponding to the O IV and Fe IX lines of Tables 3.1 and 3.2 respectively. Inspection of these figures shows that application of such spectroscopic density diagnostics to an exponential atmosphere structure leads, as expected physically, to spectroscopic mean densities $\langle\nu\rangle$ lying between the upper (ν_0) and lower ($\alpha\nu_0$) bounds of density in the atmosphere, but that $\langle\nu\rangle$ can differ greatly from $\bar{\nu}$ or $\tilde{\nu}$ when there is substantial inhomogeneity ($\alpha \ll 1$).This is seen more clearly in Figs 4.3 where we have plotted $\langle\nu\rangle/\bar{\nu}$ as a function of ν_0 for various α, for the same Λ_α values as above. It can be seen that the discrepancy between $\langle\nu\rangle$ and the physically important value $\bar{\nu}$ also depends on the matching of the density sensitivity parameter n_α to the values of n_e actually present in the atmosphere. Specifically, values of $\langle n_e\rangle$ agree best with $\overline{n_e}$ when $n_\alpha \ll n_0$ and disagree badly when $n_\alpha \gg n_0$, the extent depending on α and on Λ_α. In all cases the spectroscopic mean density errs on the high side of n_e because of its emission measure weighting toward high density regions as anticipated in Section 4.2.

The above results confirm that use of a single line ratio alone can, without other information, give very misleading results concerning the mean density of a plasma. In practice, such observations will, however, usually be obtained simultaneously with measurement of the total emission measure of the plasma (from resonance line flux) and sometimes an estimate of the source volume from images. When this is the case, further important insight into the density diagnostic problem and into solving for the true atmosphere density is gained, as follows.

Firstly we suppose that observations are made only of the total emission measure ζ_{tot} and of the spectroscopic mean density $\langle n_e\rangle$ for a single line pair (i.e. fluxes of one resonance line and one density sensitive line). Secondly we suppose that this radiation in fact comes from an exponential atmosphere as described above, though this

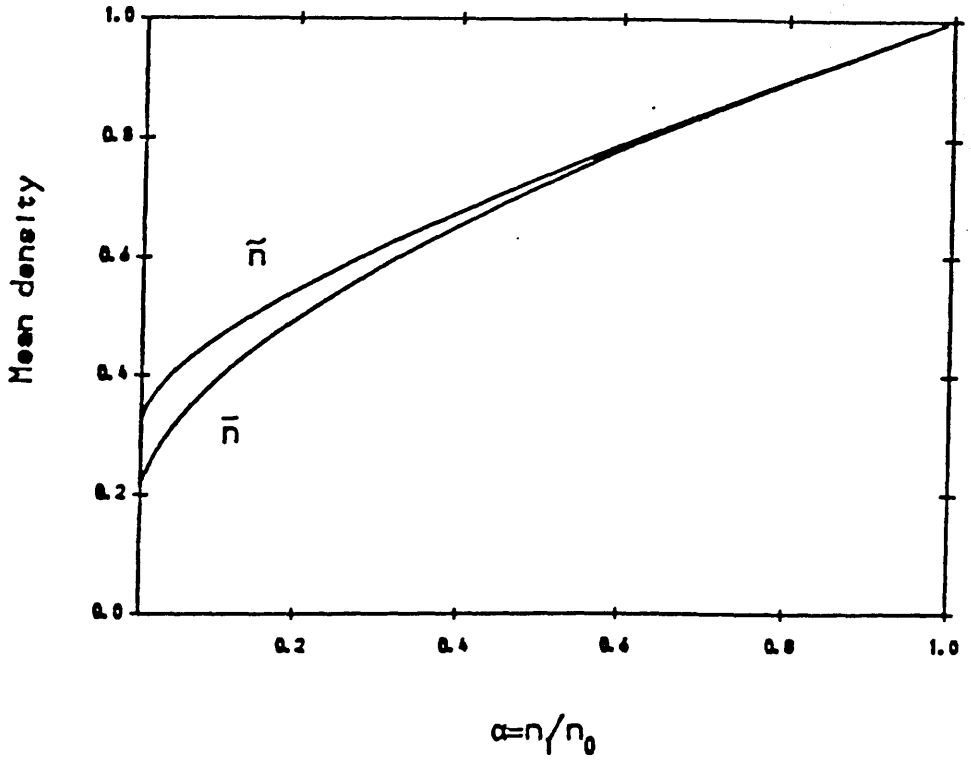

Fig. 4.1 Volumetric mean density $\bar{n}$ and emission mean density $\tilde{n}$, in units of base density n_0, as functions of the density range (inhomogeneity) parameter α for the isothermal atmosphere model of Eq. 4.18.

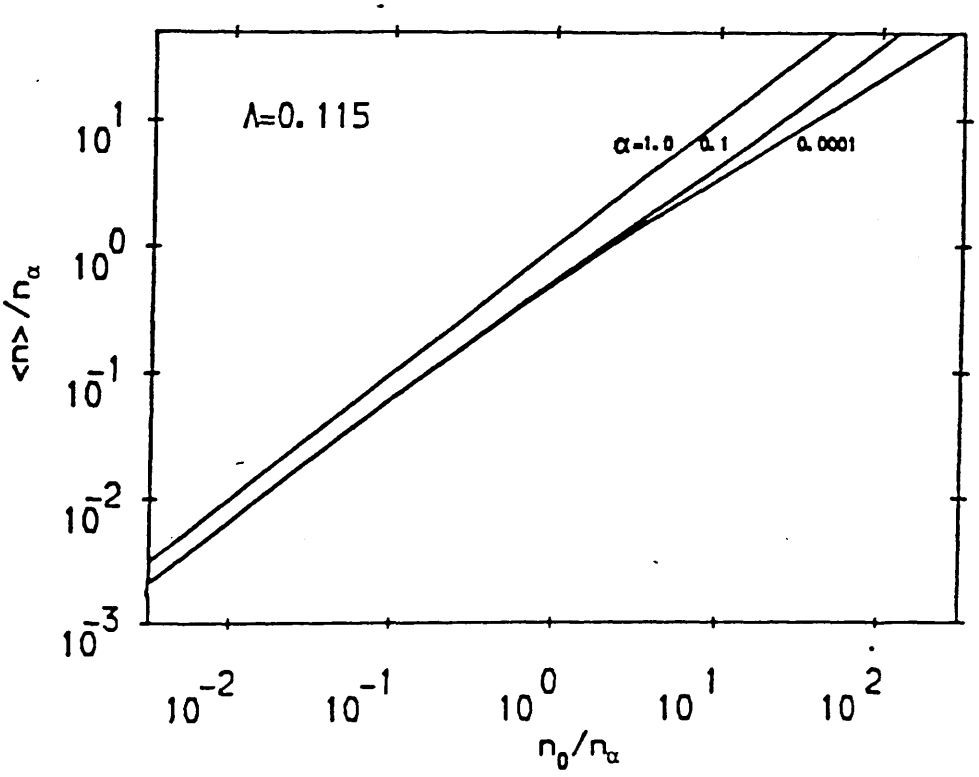

Fig. 4.2a. Spectroscopic mean density $\langle n_e \rangle$ inferred for the isothermal atmosphere model of Eq. (4.18), as a function of base density n_0 and of inhomogeneity parameter α, for the value of Λ_α=0.115 (corresponding to the O IV line pair ot Table 3.1). Both $\langle n_e \rangle$ and n_0 are shown in units of the density sensitivity parameter n_α. These curves therefore apply to any line pair with the same Λ_α value as the O IV pair, even if their n_a value is quite different from that of O IV.

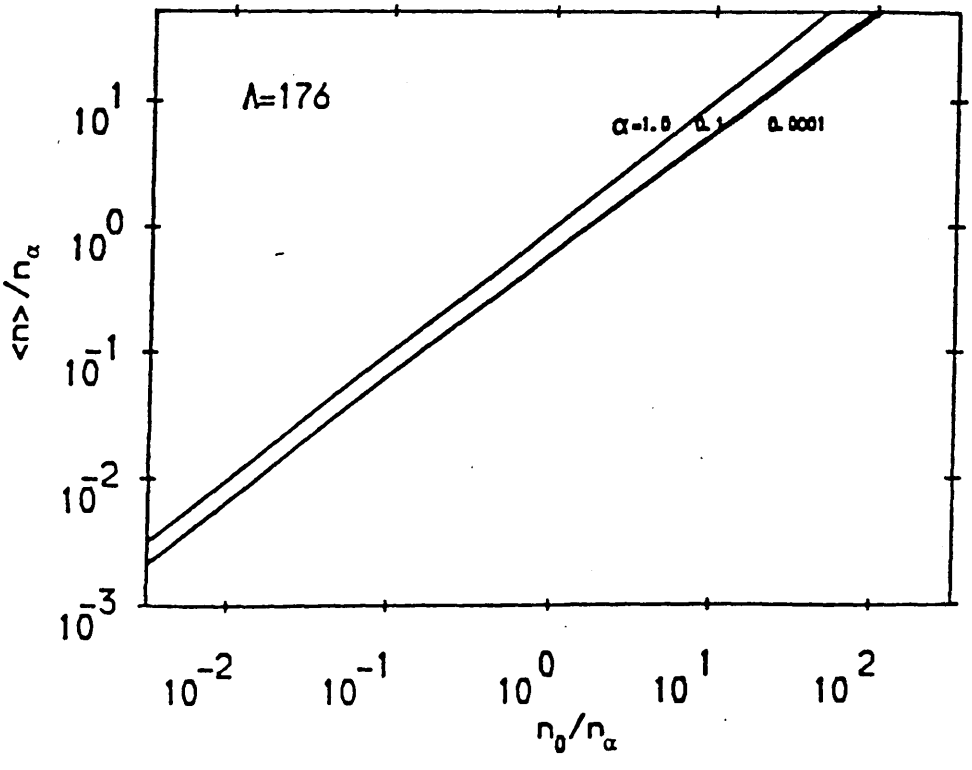

Fig. 4.2b. As Fig. 4.2a but for the value Λ_α=176 (corresponding to the Fe IX line pair of Table 3.2).

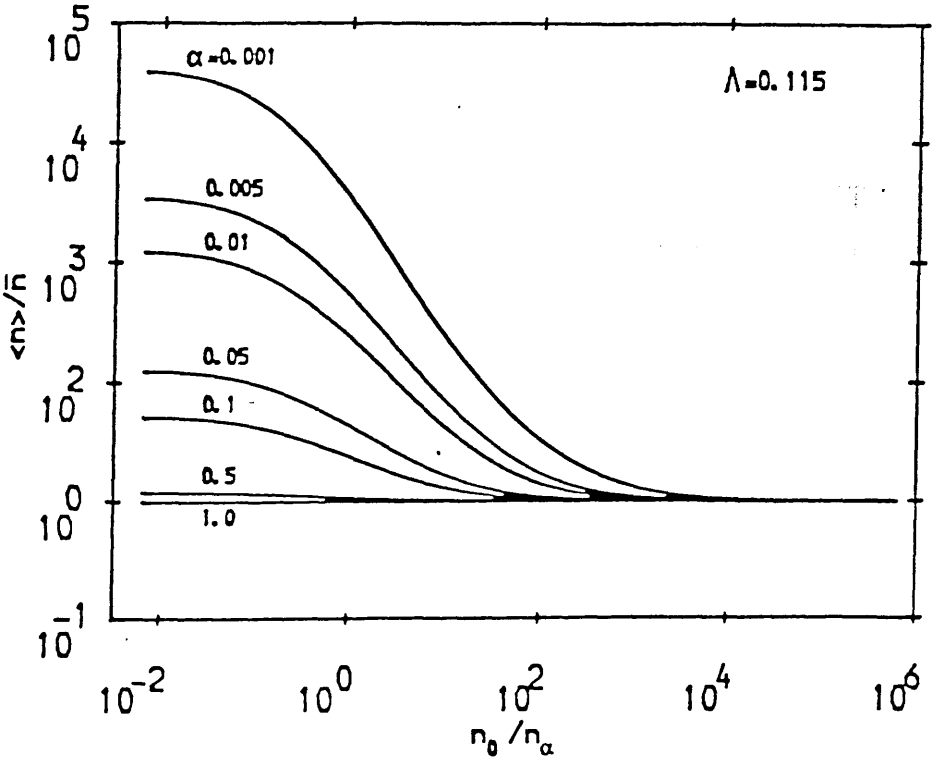

Fig. 4.3a. Inferred spectroscopic mean density $\langle n_e \rangle$, compared to volumetric mean density $\bar{n}$, in the exponential atmosphere model of Eq. (4.18), as a function of base density n_0 and of inhomogeneous parameter α, for a line pair with Λ_α=0.115.

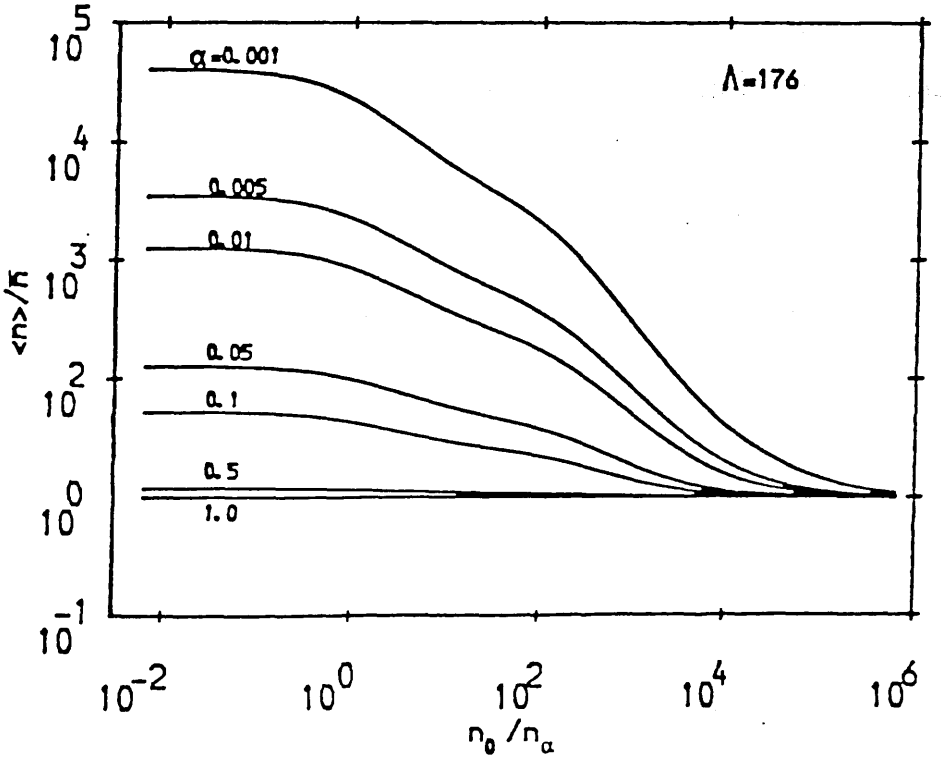

Fig. 4.3b. As Fig. 4.3a but for a line pair with Λ_α=176.

structure is unknown to the observer. A common procedure in such cases is to infer an effective or 'spectroscopic' volume (Dere and Mason 1981)

$$<V> = \zeta_{tot} / <n_e>^2 \qquad (4.26)$$

In the case of one resonance line we find, using (4.17) with $\eta(\nu)$ given by (4.23),

$$\frac{<n_e>}{n_\alpha} = \frac{\nu_0^2(1-\alpha^2)/2 - \nu_0(1-\alpha) + \ln[(1+\nu_0)/(1+\alpha\nu_0)]}{\nu_0(1-\alpha) - \ln[(1+\nu_0)/(1+\alpha\nu_0)]} \qquad (4.27)$$

while by (4.20), the true volume V= S H is related to ζ_{tot} by

$$V = \frac{2\ln(1/\alpha)}{1-\alpha^2}\,\frac{\zeta_{TOT}}{n_\alpha^2}\,\frac{1}{\nu_0^2} \qquad (4.28)$$

Hence by (4.26) and (4.28) the ratio of spectroscopic to true volume for an exponential atmosphere is

$$f = \frac{<V>}{V} = \frac{1-\alpha^2\nu_0^2}{2\ln(1/\alpha)}\left[\frac{\nu_0(1-\alpha) - \ln[(1+\nu_0)/(1+\alpha\nu_0)]}{\nu_0^2(1-\alpha^2)/2 - \nu_0(1-\alpha) + \ln[(1+\nu_0)/(1+\alpha\nu_0)]}\right] \qquad (4.29)$$

which we plot in Fig.4.4 as a function of α and ν_0.

It is clear that f«1 for all (α, ν_0) and that for any given ν_0, f only approaches unity as α tends to one (homogeneous source); the approach being slowest when ν_0«1 i.e. n_0«n_α. This means that if an observer of ζ_{tot} and $<n_e>$ interprets these data on the assumption that the plasma is homogeneous -i.e. $n_e(\underline{r}) = <n_e>$ (or $\zeta(n_e) \sim \delta(n_e - <n_e>)$), when it is in fact inhomogeneous, then the volume <V> given by (4.26) will always be less than the actual spatially resolved emitting volume V, the more so when the inhomogeneity is large. In other words the homogeneous interpretation of spectroscopic density will always yield small 'filling factors' when applied to an inhomogeneous source as is often found observationally-e.g Dere (1982) finds f=0.1-0.001. In the next section, we will demonstrate that this result is universally true, irrespective of the form (apart from monotonicity) of the $G(n_e)$ functions for the lines concerned. This result explains

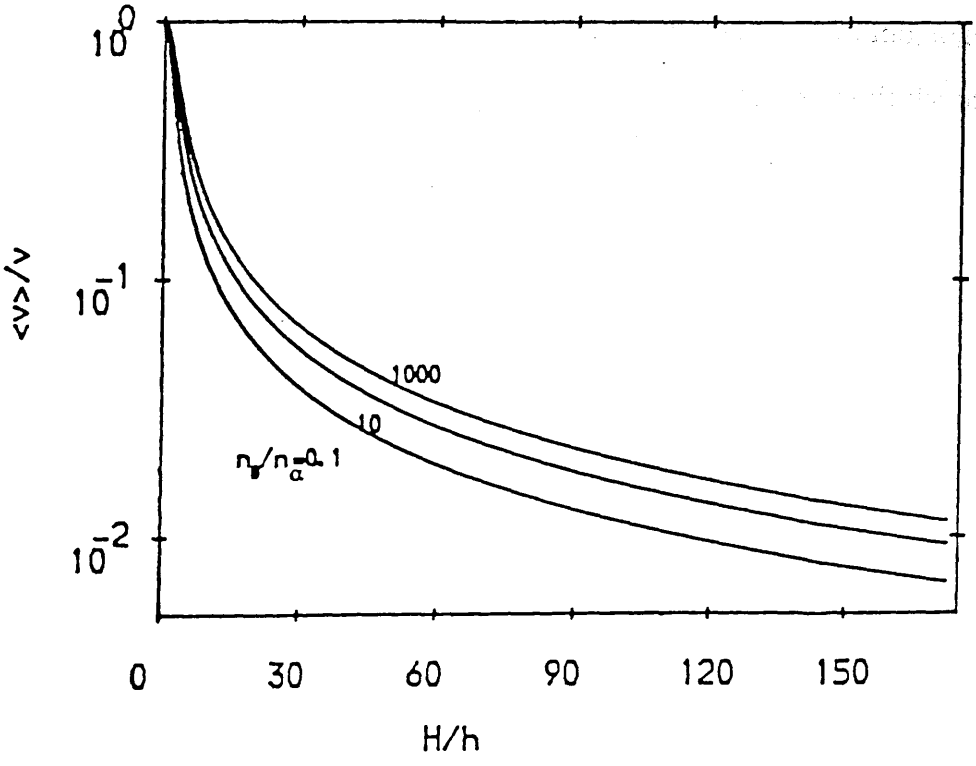

Fig. 4.4. Inferred spectroscopic volume $\langle V \rangle = \zeta_{tot}/\langle n_e \rangle$, relative to true volume V, ('filling factor'), for an exponential atmosphere, as a function of base density n_0 (in units of line density sensitive parameter n_α) and of atmospheric inhomogeneity expressed in terms of number of scale heights ($H/h = \ln(1/\alpha)$).

the apparent paradox that even when numerous line pairs are observed, formed in different regions of both density and temperature, their 'filling factors' f inferred as above do not sum to unity. What these results imply is that the source volumes of all the observed lines contain substantial density inhomogeneity within them so that their true volumes are much larger than the estimates <V> - there is then no question of any 'unfilled' volume. Indeed, observations yielding <V><V are an important measure of source inhomogeneity such as may be present due to unstable filamentation or fragmentation of the plasma on a small scale, especially in solar flares, as well as to the large scale gravitational density stratification discussed above. To illustrate this explicitly in this last case, suppose we infer <v> for some given line pair ratio, together with the total emission measure ζ_{tot} and the total volume V. Then for the particular parametrisation of this model we have by (4.20)

$$\frac{\nu_0^2(1-\alpha^2)}{2\ln(1/\alpha)} = \frac{\zeta_{tot}}{n_\alpha^2 V} = \mu \qquad (4.30)$$

and by (4.24)

$$\Phi\wedge_\alpha(\nu_0, \alpha) = <\nu> \qquad (4.31)$$

where the right hand sides are observed, and $\Phi\Lambda_\alpha$ represents the right hand side of (4.24). These two equations can then be solved numerically to find α (for a description of this numerical method Appendix (A.1) should be consulted), which measures the inhomogeneity, and for $n_0=\nu_0\, n_\alpha$, from which we can determine $\bar{n}_e$ by (4.21) and hence the mass of the source plasma from $\bar{n}_e V$. Results for $\bar{\nu}$ and α are shown in Figs. 4.5 and 4.6 for our usual two Λ_α values.

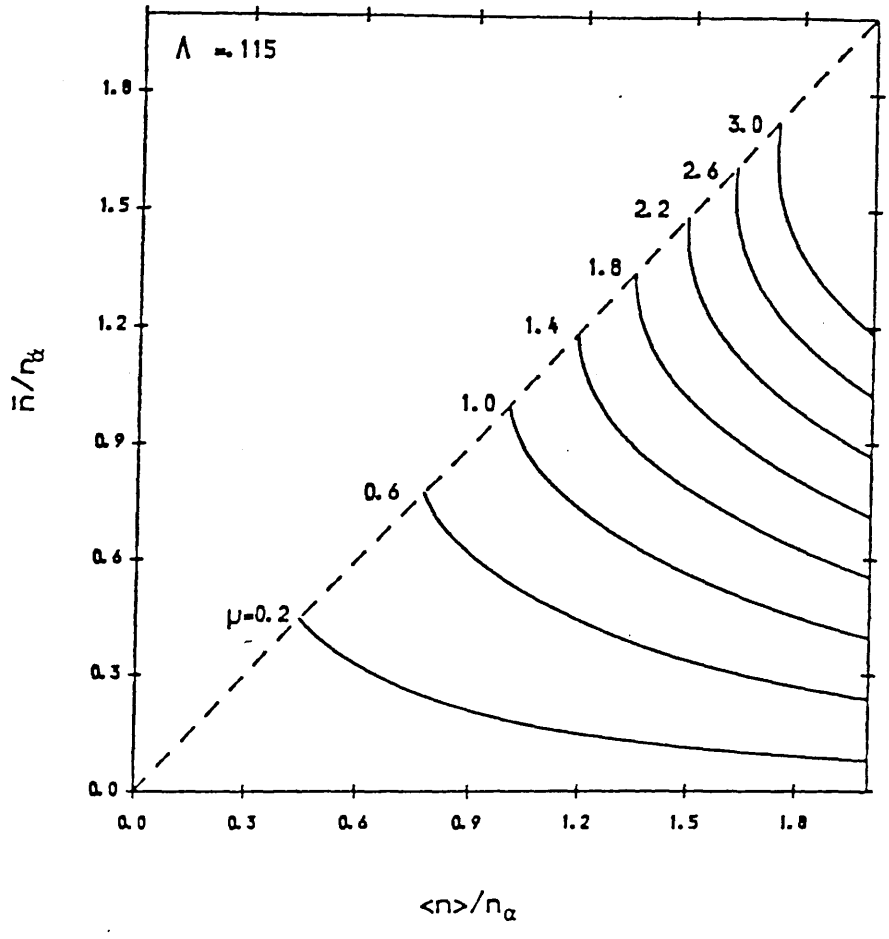

Fig. 4.5a. Volumetric mean density $\bar{n}$ (in units of n_α) inferrable, for an assumed exponential form of atmosphere structure, from observations of the intensities of one allowed line (i.e. of total emission measure ζ_{tot}), one density sensitive line ratio (i.e. of atmospheric mean density $<n_e>$) and of volume V. Each solid curve corresponds to a specific observed value of the parameter $\mu=\zeta_{tot}/(n_\alpha{}^2\ V)$. The dashed boundary corresponds to the homogeneous (maximum mean density/minimum volume) solution. Results are given for a density sensitivity parameter $\Lambda=0.115$.

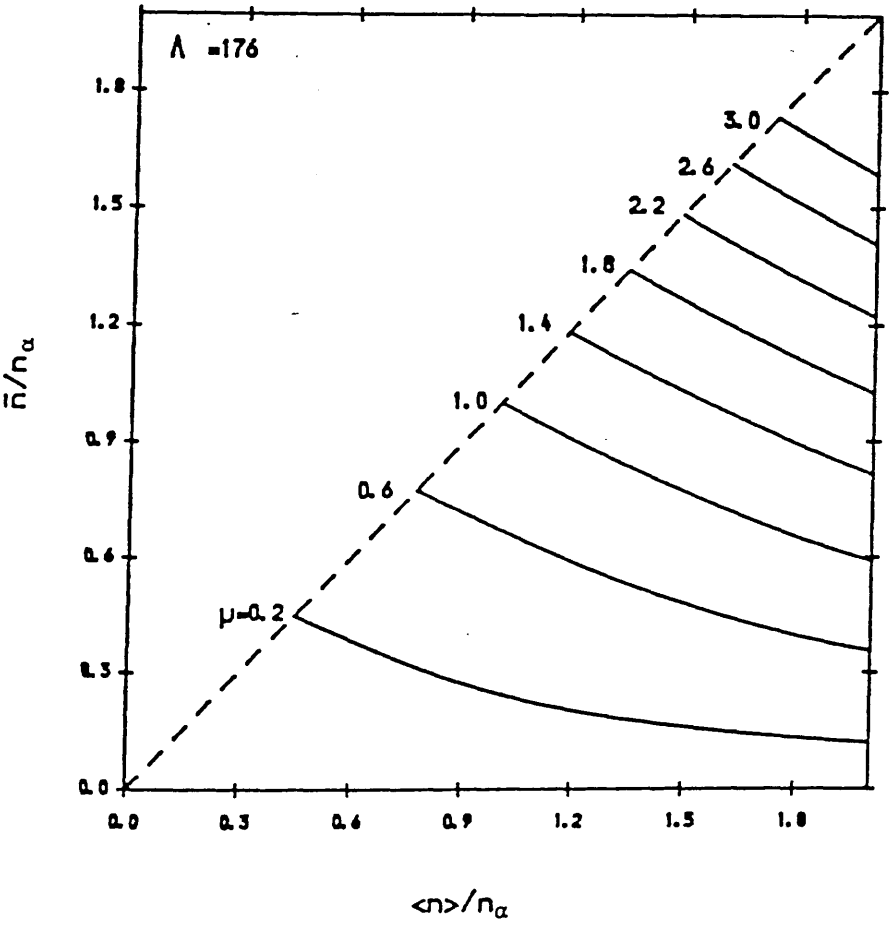

Fig. 4.5b. As Fig. 4.5a except for density sensitivity parameter Λ_α=176.

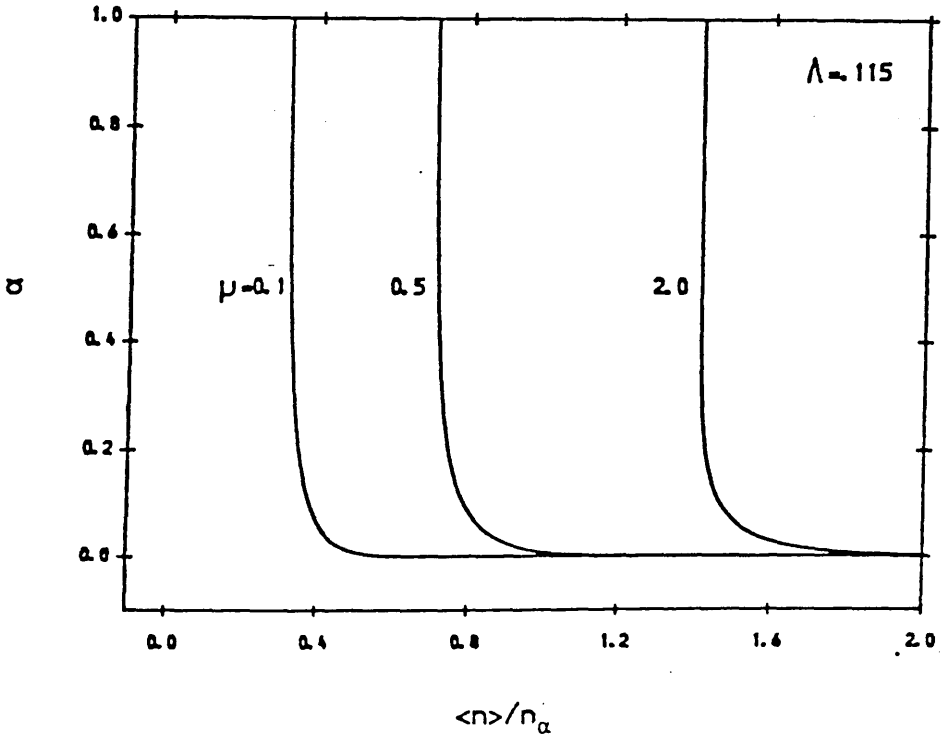

Fig. 4.6a. Inhomogeneity parameter $\alpha(=n_1/n_0)$ inferrable, for an assumed exponential form of atmospheric structure, from the same set of observations as described for Fig. 4.5a, for Λ_α=0.115. The vertical asymptotes for each μ value correspond to the fact that the inferred spectroscopic $<n_e>$ can never be less than the homogeneous solution value $n_e=(\zeta_{tot}/V)^{1/2}$.

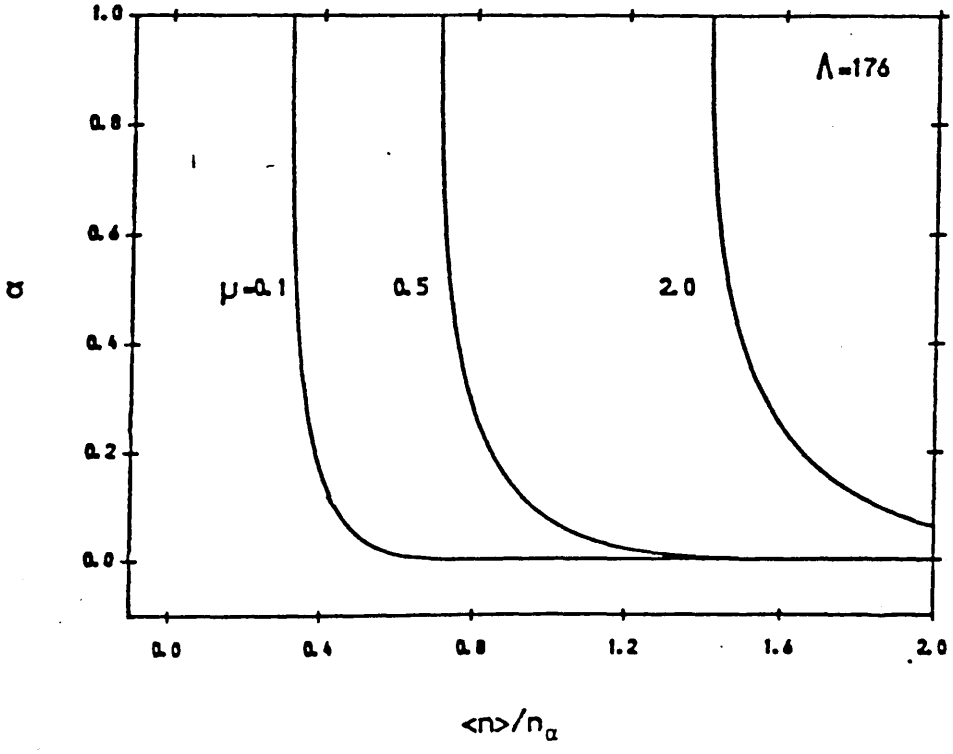

Fig. 4.6b. As Fig. 4.6a except for Λ_α=176.

4.5. The inverse problem and minimum volume solutions for a set of prescribed line strengths

The result suggested in Section 4.4 that a homogeneous source minimises the volume needed to fit a prescribed pair of line strengths, can be generalised to more than two lines by using the spatial integral form of the problem (4.2), rather than its expression in (4.5) in terms of $\zeta(n_e)$. Consider, therefore, a situation where the strengths of two distinct lines are prescribed by observations, viz

$$\int_V n_e^2(\underline{r})\, G_1(n_e)\, dV = P_1 \qquad (4.32)$$

$$\int_V n_e^2(\underline{r})\, G_2(n_e)\, dV = P_2 \qquad (4.33)$$

where G_1/G_2 is monotonic in n_e. If we have some solution $n_e(\underline{r})$ for these equations, then we can consider any other solution in terms of a perturbation $\delta n_e(\underline{r})$ with associated perturbation δV in V. In order to comply with the observations (4.32) and (4.33), this perturbation must satisfy

$$\int_V [n_e^2 G_1' + 2n_e G_1]\delta n_e dV + \int_{\delta V} n_e^2 G_1 dV = 0 \qquad (4.34)$$

$$\int_V [n_e^2 G_2' + 2nG_2]\delta n_e dV + \int_{\delta V} n_e^2 G_2 dV = 0 \qquad (4.35)$$

To obtain the distribution $n_e(\underline{r})$ which gives an extremum in V we require that $\delta V = 0$ and that (4.34) and (4.35) be satisfied for all perturbations $\delta n_e(\underline{r})$ about that distribution. That is

$$\int_V [n_e^2 G_1' + 2n_e G_1]\delta n_e\, dV = 0$$

$$\int_V [n^2 G_2' + 2n_e G_2]\delta n_e\, dV = 0 \qquad (4.36)$$

and for all $\delta n_e(\underline{r})$

The simultaneous solution of which, for all δn_e, requires

$$(2G_1 + n_e G_2') + \lambda(2G_2 + n_e G_2') = 0, \quad \text{for all } \underline{r} \tag{4.37}$$

where λ is a Lagrange undetermined multiplier. Since G_1, G_2 are functions of n_e only, (4.37) shows that the extremum solution has $n(\underline{r}) = n_0$ independent of $\underline{r}$, n_0 being the solution of (4.37), and λ being found from the original equations (4.32) and (4.33) namely

$$g(n_0) = \frac{G_1(n_0)}{G_2(n_0)} = R_{12} = \frac{P_1}{P_2} \tag{4.38}$$

which determines n_0 uniquely since g is monotonic. Then

$$V_{\text{extremum}} = V_0 = \frac{P_1}{n_0^2 G_1(n_0)} = \frac{P_2}{n_0^2 G_2(n_0)} \tag{4.39}$$

To demonstrate that this extremum is a minimum, it is only necessary to show that some other specific solution $n_e(\underline{r})$ has a larger associated V. Consider for example a solution comprising two uniform regions of densities and volumes (n_A, V_A), (n_B, V_B) respectively. Then to satisfy (4.32) and (4.33) we must have

$$n_A^2 V_A G_1(n_A) + n_B^2 V_B G_1(n_B) = P_1 \tag{4.40}$$

$$n_A^2 V_A G_2(n_A) + n_B^2 V_B G_2(n_B) = P_2 \tag{4.41}$$

from which we can deduce, using (4.38) and (4.39) that

$$\frac{V_A}{V_0} = \frac{n_0^2}{n_A^2} \frac{G_2(n_0)}{G_2(n_A)} \left[\frac{g(n_0) - g(n_B)}{g(n_A) - g(n_B)}\right] \tag{4.42}$$

and

$$\frac{V_B}{V_0} = \frac{n_0^2}{n_B^2} \frac{G_2(n_0)}{G_2(n_B)} \left[\frac{g(n_A) - g(n_0)}{g(n_A) - g(n_B)}\right] \tag{4.43}$$

the total volume V satisfying

$$\frac{V}{V_0} = \frac{V_A}{V_0} + \frac{V_B}{V_0} \tag{4.44}$$

Now for V_A and V_B both to be > 0, (4.42) and (4.43) require that $g(n_0)$ lies between $g(n_A)$ and $g(n_B)$ or, since g is monotonic, that n_0 lie between n_A and n_B. Suppose, without loss of generality, that g is monotonically increasing and that $n_A > n_0 > n_B$. Then, in the particular case where $n_A \gg n_0 \gg n_B$, V_B will be $\gg V_A$ and $V/V_0 \simeq V_B/V_0 \to \infty$ as $n_B/n_0 \to 0$ (provided $n^2 G_2(n_e) \to 0$ as $n_e \to 0$ and $n_e^2 G_2(n_e) \to \infty$ as $n_e \to \infty$), thus showing (4.39) to be a minimum.

Physically the fact that the homogeneous solution yields a minimum volume can be understood by noting that as n_A increases and n_B decreases the amount by which the volume of the n_B plasma has to be increased is more than that by which the volume of the n_A plasma has to be reduced, in order to retain the observed values of P_1 and P_2, because of the n_e^2 weighting of the emissivity per unit volume. The sharpness of the minimum (4.39) depends on the G functions and on the particular value of P_1/P_2. We illustrate expressions (4.42)-(4.44) here by considering the special case where line 2 is a resonance line (G_2 independent of n_e or $\Lambda_\alpha \to \infty$), line 1 has G_1 of the form (3.6) and the observed line ratio corresponds to a homogeneous solution $n_0 = \beta n_\alpha$. Then if we consider an inhomogeneous solution with $n_A = \gamma n_0$, $n_B = n_0/\gamma$, (4.42)-(4.44) with (3.6)-(3.10) give

$$\frac{V_A}{V_0} = \frac{1}{\gamma^2} \frac{(1+\beta\gamma)}{(1+\beta)(1+\gamma)}; \quad \frac{V_B}{V_0} = \frac{\gamma^2(\gamma+\beta)}{(1+\beta)(1+\gamma)} \qquad (4.45)$$

Figure 4.7 shows V_A, V_B, V as functions of γ for the case $\beta=1$. Other β values give similar results though the sharpness of the minimum does depend on β. Having established that a homogeneous solution always exists for any pair of line strengths, and that this is a minimum volume solution, it is next natural to consider situations when three or more line strengths are specified. Consider then the situation where P_1, P_2, P_3 are prescribed for three lines of distinct $G(n_e)$. It is at once clear that the homogeneous density solution say $n_0^{1,2}$, $V_0^{1,2}$ for any single line pair P_1, P_2 will not in general

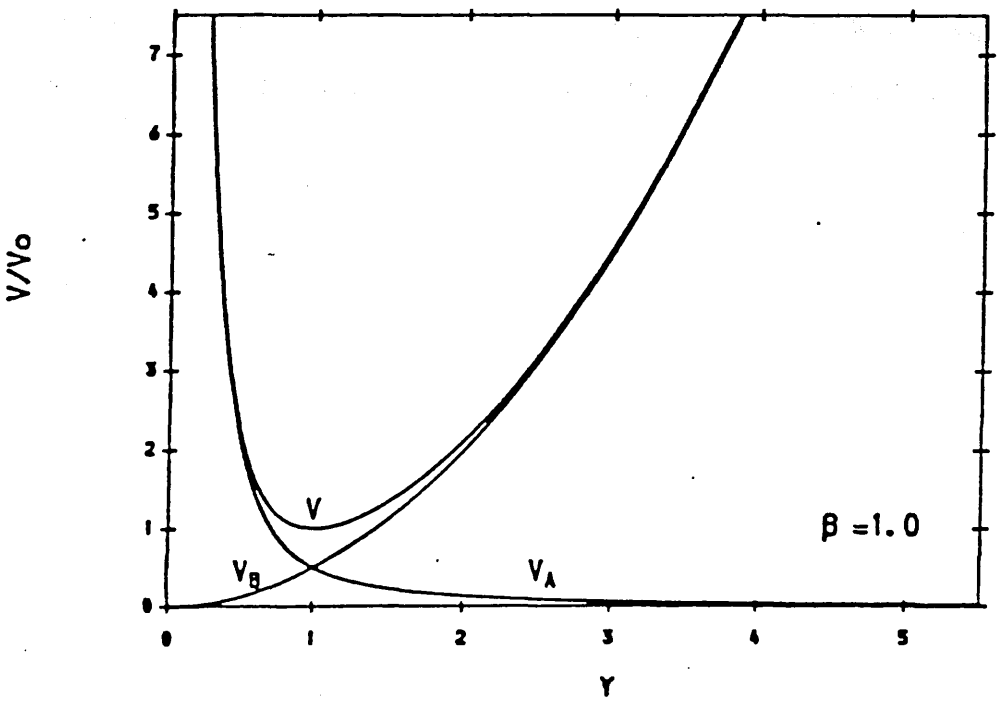

Fig. 4.7. Total volume V, and separate volumes (V_A, V_B) of two distinct homogeneous high density regions of density ratio γ^2, needed to produce the same total emission measure and the same forbidden/allowed line ratio as a single homogeneous region (γ=1), of density n_e=n_α and volume V_0. This volume V minimises sharply at the homogeneous solution.

reproduce the third line strength P_3 unless the plasma is in fact homogeneous. Thus any solution reproducing arbitrary P_1,P_2 and P_3 must in general be inhomogeneous, and from the above analysis applied to each line pair, it also follows that any solution for three general line strengths must necessarily have a volume $V^{1,2,3} > \max \{V_0^{1,2}\ V_0^{1,3}, V_0^{2,3}\}$. By generalisation of the variational method applied in (4.36)-(4.39), it can in fact be shown that the minimum volume solution $n_e(\underline{r})$ for three prescribed line strengths comprises a pair of homogeneous regions of distinct densities, their total volume exceeding that of the homogeneous solutions for each line pair taken separately, unless the plasma is in fact homogeneous. It is also clear qualitatively that the greater the inhomogeneity of the real plasma, the greater will be the total volume of the two component plasma needed to fit a third line strength compared to that required for any two line strengths considered alone. Furthermore, as the number of specified line strengths is increased beyond three ,the number and total volume of regions of distinctly needed for a minimum volume solution may be anticipated as increasing. We may also anticipate that, in principle, prescription of an infinite set of distinct P_α values will asymptotically yield a complete solution of the inverse problem

$$\int_0^\infty \zeta(n_e)\, G_\alpha\,(n_e)\, dn_e = P_\alpha \qquad (4.46)$$

for $\zeta(n_e)$ represented in terms of an infinite series of piecewise homogeneous elementary volumes, the total of which will be the true plasma volume. For the density sensitivity representation of Section 3, the specific inverse problem amounts to solution of the Fredholm equation of the form.

$$\int_0^\infty \zeta(n_e)\, K\,(n_e, m)\ dn_e = Q(m) \qquad (4.47)$$

with

$Q(m) = P_\alpha\,(m)\,/mK_\alpha\,(m)$

and kernel

$$K(n_e,m) = 1/(m+n_e) \qquad (4.48)$$

The analytic and numerical properties of this equation, and the serious implications of the instability of its inversion (cf. Craig and Brown 1986), for such problems as density structure analysis are discussed by Thompson and Sweet (1988).

4.6 Summary and Conclusions

We have addressed the problem of interpreting density line strengths from an isothermal plasma of inhomogeneous density $n_e(\underline{r})$. In the case of two observed lines, we have shown that the results may be expressed in terms of a spectroscopic mean density $\langle n_e \rangle$ which is the density of a homogeneous plasma which would produce the same line ratio. The value of $\langle n_e \rangle$ will differ for different line pairs, and differ from both the volumetric mean $\bar{n}$ and emissivity mean $\tilde{n}$ unless the plasma is actually homogeneous. This effect was illustrated, using a simple but accurate representation of density sensitivity, by means of an exponential atmosphere model which showed how large a variation in $\langle n_e \rangle / \bar{n}$ (Figs 4.3) can occur and how this variation serves to measure the plasma inhomogeneity. This effect explains the different densities commonly inferred for the same source by application of different diagnostic line pairs.

More generally we have shown that the values of a set of density dependent line strengths are related by an integral equation to the inhomogeneous plasma structure in terms of an emission measure function $\zeta(n_e)$, differential in density n_e. For a finite number of line strengths, $\zeta(n_e)$ can never be determined completely, even in principle. However, for a finite set of N such measurements, there does exist a unique solution for $\zeta(n_e)$ which minimises the total source volume V consistent with the data, namely a set of N-1 delta functions, corresponding to a set of N-1 spatial regions, each of uniform, but different, density. In particular, for a single line ratio, the volume V inferred will be minimal when the plasma is assumed to have uniform density $\langle n_e \rangle$ (i.e.$\zeta(n_e)$ is a delta function of $n_e = \langle n_e \rangle$), this volume being always less than the true volume if the plasma is inhomogeneous. This effect must contribute to the commonly observed and puzzling 'phenomenon' of small 'filling factors' when spectroscopically deduced volumes are

compared with spatially resolved volumes. We have illustrated this effect again using the exponential atmosphere model as an example.

As the number of observed lines is increased, the minimum volume solution for $\zeta(n_e)$ progressively approaches the true inhomogeneous structure and its volume approaches the true volume. For our chosen representation of density sensitivity we have briefly discussed the form of the integral equation the solution of which in principle yields this true $\zeta(n_e)$. We emphasise, however, that instability of the inversion process will necessarily limit the possibility of recovery in the same way as occurs in inference of emission measure differential in temperature, from temperature sensitive allowed line ratios from non-isothermal plasma.

This problem of recovering $\zeta(n_e)$ from spectral information alone, combined with the extreme inhomogeneity of solar plasmas indicated by their small inferred filling factors, shows that high spatial resolution will be needed for much further progress in this problem.

CHAPTER 5

MULTITHERMAL PLASMAS OF INHOMOGENEOUS STRUCTURE

5.1. Introduction

In the preceeding chapter we have reviewed and discussed the problems and the importance of determining the density, as well as the temperature, structure of inhomogeneous plasmas. In chapter 4 we restricted ourselves to the detailed treatment of how to interpret one or more density sensitive line intensity ratios for plasmas which are isothermal but of non-uniform density. We concluded that : observations of a single line ratio from such a plasma will in general yield an overestimate of the mean plasma density, to an extent increasing with plasma inhomogeneity; observations of more and more distinct line ratios in principle can lead to derivation of the emission measure $\zeta(n_e)$ per unit density n_e; in practice such derivation of $\zeta(n_e)$ will be sharply limited by data noise, but can certainly give a valuable quantitative measure of the degree of density inhomogeneity.

In this chapter, we generalise the formulation of the problem to cases where both the density n_e and temperature T are inhomogeneous, showing how the concepts of emission measure differential in temperature $\xi(T)$, utilised in resonance line analysis of temperature structure, and of $\zeta(n_e)$, utilised in density structure analysis in the isothermal case, can be extended for arbitrary plasmas. We then show how in the special, degenerate, case where surfaces of constant T and of constant n_e coincide, it is possible to utilise jointly data on temperature and density sensitive line ratios to draw conclusions concerning the plasma pressure distribution $P(T)=2n_e(T)kT$.

As our starting point we take the expression for the power emitted in a particular line, denoted by α, which is a function of electron temperature, density, and volume from an optically thin plasma of volume V, which in the notation used in chapter 4 is

$$P_\alpha = \iiint_V n_e^2(\underline{r})\, F_\alpha(n_e(\underline{r}), T(\underline{r}))\, dV \qquad (5.1)$$

where $n_e(\underline{r})$, $T(\underline{r})$ are values at position $\underline{r}$. The function F_α is determined by ionisation and excitation balance calculations based on atomic coefficients (assumed known). While

some of our discussion will deal with arbitrary forms of F_α we will also utilise the expression used in chapter 4, which approximates well to all line ratios of interest, viz.

$$F_\alpha(n_e, T) = \frac{K_\alpha(T)}{1 + n_e / n_\alpha(T)} \qquad (5.2)$$

but where we now allow for the variation of K_α and n_α with temperature (and hence position) whereas they were considered constant in the isothermal case treated in the previous chapter. In expression (5.2) K_α is a measure of the power emitted at low n_e, where radiative de-excitation dominates, and n_α is a measure of the density sensitive range of n_e at which collisional de-excitation becomes important for the line concerned. ($n_\alpha \rightarrow \infty$ for resonance lines). We would emphasise, as discussed in Chapter 4 that although (5.2) is a precise physically based description for '2-level' systems (cf. Section 5.3) the same functional form is also a numerically good description of the n_e, T dependence in more complex atomic situations provided the atomic constants occuring in K_α and n_α are empirically adjusted to give the best fit.

5.2. General formulation

It is useful first to recall the formulation for the special case of resonance lines where F_α is independent of n_e and the proper choice of volume element dV is based on constant temperature surfaces S_T, leading to (Craig and Brown 1976)

$$P_\alpha^R = \int_{T=0}^{\infty} \xi(T)\, F_\alpha^R(T)\, dT \qquad (5.3)$$

where

$$\xi(T) = \iint_{S_T} \frac{n_e^2(r)}{|\nabla T(r)|}\, dS_T \qquad (5.4)$$

is the emission measure differential in T which can, in principle, be derived from the integral equation (5.3) using measurements of sufficiently many temperature sensitive resonance line strengths (of different α values). Likewise the special case of density sensitive line analysis for an isothermal plasma of known temperature T_0 has a natural formulation (chapter 4) in terms of the emission measure $\zeta(n_e)$ differential in density

defined in terms of a volume element dV related to constant density surfaces S_{n_e}, viz.

$$P_\alpha^D = \int_{n_e=0}^{\infty} \zeta(n_e) F_\alpha^D(n_e, T_0)\, dn \qquad (5.5)$$

where

$$\zeta(n_e) = \iint_{S_{n_e}} \frac{n_e^2(\underline{r})}{|\nabla n_e(\underline{r})|}\, dS_{n_e} \qquad (5.6)$$

(In the case of both (5.4), (5.6) the most general definitions include summations $\sum_{S_T}$ and $\sum_{S_n}$ respectively over all disjoint surfaces S_T or S_{n_e} but we omit these here for simplicity).

Consideration of these two cases then indicates that for the general case (equation 5.1) we must deal with a volume element dV related to elements on which both n_e and T are constants. There are two situations. In one (degenerate), surfaces of constant n_e and of constant T are coincident. This is in fact the case which proves most tractable in terms of an inversion of the problem and which is probably of the greatest practical relevance. We return to it shortly but first we consider the second (and more general) case where S_{n_e} and S_T are not coincident but intersect on a line $L_{n_e,T}$. Then the natural formulation of equation (5.1) into an integral expression over the variables n_e, T on which the line strength depends, is in terms of the volume element (see Fig 5.1) .

$$dV = dL_{n_e,T} \frac{dn_e\, dT}{|\nabla n_e||\nabla T| \sin \theta_{n_e,T}} \qquad (5.7)$$

where $\theta_{n_e,T}$ is the local angle between the vectors ∇n_e and ∇T normal to surfaces S_{n_e}, S_T respectively and $dL_{n_e,T}$ is an element of length on $L_{n_e,T}$. If we then define an emission measure function differential in both density and temperature by

$$\psi(n_e, T) = \oint_{L_{n_e,T}} \frac{n_e^2(\underline{r})\, dL_{n_e,T}}{|\nabla n_e(\underline{r})|\,|\nabla T(\underline{r})| \sin \theta_{n_e,T}(\underline{r})} \qquad (5.8)$$

we have for any line

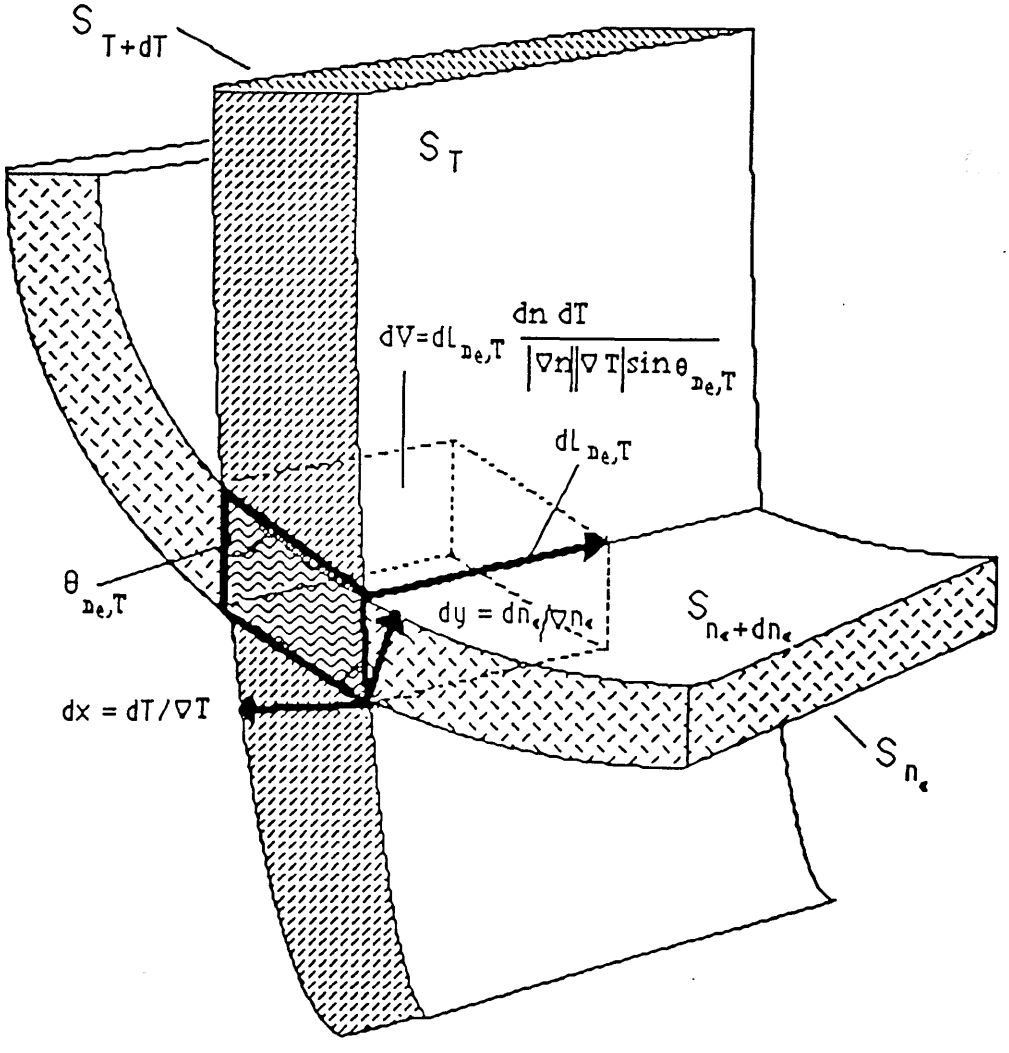

Figure 5.1.Two surfaces of constant temperature S_T and of constant density S_{n_e} intersecting on a line $L_{n_e,T}$. $\theta_{n_e,T}$ is the angle between the vectors ∇T and ∇n_e normal to the surfaces S_T, S_{n_e} respectively.

$$P_\alpha = \int_{n_e=0}^{\infty}\int_{T=0}^{\infty} \psi(n_e, T)\, F_\alpha(n_e, T)\, dn_e\, dT \qquad (5.9)$$

The general diagnostic problem is then seen as that of determining $\psi(n_e, T)$ by inversion of the double integral equation (5.9) for a set of measurements P_α, of various α, noting that α is not a single parameter but a label indicating the set of parameters arising in the density and temperature sensitivities of the different lines; for example K_α and n_α in representation (5.2) for which (5.9) becomes

$$P_\alpha = \int_{T=0}^{\infty} K_\alpha(T) \int_{n_e=0}^{\infty} \frac{\psi(n_e, T)\, dn_e\, dT}{1 + n_e / n_\alpha(T)} \qquad (5.10)$$

The rather convoluted functional $\psi(n_e,T)$ of $n_e(\underline{r})$, and $T(\underline{r})$ is thus the most we can ever learn spectroscopically about the plasma structure in the general case without making further assumptions. In the form (5.10) it is clear that as $n_\alpha \to \infty$ (resonance lines) the inner integral becomes $\xi(T)$ and the problem is the standard one of temperature analysis while in the isothermal case ψ is a delta function in T and (5.10) reduces to the density analysis problem for the isothermal case discussed in chapter 4.

It is important to note that resonance line analysis in principle always admits a solution for the inner integral of (5.10) with $n_\alpha \to \infty$ which can then be utilised in solution of (5.10) for density sensitive lines.-a property we will use below in analysis of the first case cited above.

When the surfaces S_T and S_{n_e} coincide, as they will in constant pressure or pressure-stratified structures for example, definition (5.8) fails because $\theta_{n_e,T}$ is everywhere zero. However, in this case we have the important property that the two surface integral functions $\xi(T)$ and $\zeta(n_e)$ both exist and are inter-related by

$$\xi(T) = \zeta(n_e)\left|\frac{dn_e}{dT}\right| \qquad (5.11)$$

Thus if we can determine $\xi(T)$ from resonance line analysis (5.3) we then know $\zeta(n_e)$ multiplied by an unknown function $|dn_e / dT|$, and by use of density sensitive lines we can integrate to find the form of $n_e(T)$ using (5.5). That is we can write (5.5) as

$$P_\alpha^D = \int_{T=o}^{\infty} \xi(T)\, F_\alpha^D(n_e(T), T))\, dT \qquad (5.12)$$

in which (given $\xi(T)$) the single unknown is the function $n_e(T)$, in principle determinable by solution of (5.12) from a set of density sensitive line strengths P_α^D. To illustrate this further we investigate (in Sections 5.3 and 5.4) the particular case when F_α^D is given by the form (5.2) used in chapter 4. Before doing so, however, we consider what will be the meaning of the $n_e(T)$ function so inferred when the source is assumed to be pressure stratified ($n_e=n_e(T)$ only), although in reality this situation is extremely unlikely. Clearly the result of solving (5.12) in such a case will be some kind of mean $\bar{n}_e(T)$ of n_e over the surface S_T weighted with respect to the density sensitivity function $F_\alpha^D(n_e, T)$ on that surface. To see the form of this mean we equate (5.12), with n_e replaced by $\bar{n}_e(T)$, to the general expression (5.9), in the form

$$\int_{T=0}^{\infty} \left[\int_{n_e=0}^{\infty} \psi(n_e, T) F_\alpha^D(n_e, T) dn \right] dT = \int_{T=0}^{\infty} \xi(T) F_\alpha^D(\bar{n}_e(T), T) dT \qquad (5.13)$$

so that, by definition (5.8) of $\Psi(n_e,T)$, $\bar{n}_e(T)$ is the solution of

$$F_\alpha^D(\bar{n}_e(T), T) = \frac{1}{\xi(T)} \int_{n_e=0}^{\infty} \oint_{L_{n_e,T}} F_\alpha^D(n_e, T)\, n_e^2(r) \frac{dn_e\, dL_{n_e,T}}{|\nabla n_e|\,|\nabla T| \sin\theta_{n_e,T}} \qquad (5.14)$$

where the equality holds for all α.

5.3.Formal Solution for Density Distribution $n_e(T)$ in a Pressure Stratified Plasma

For the density sensitive representation (5.2), equation (5.12) becomes

$$P_\alpha^D = \int_0^{\infty} \frac{\xi(T)\, K_\alpha(T) dT}{1 + n_e(T) / n_\alpha(T)} \qquad (5.15)$$

which, if $\xi(T)$ is known from resonance line analysis, is an integral equation for $n_e(T)$, given P_α^D, which describes the pressure distribution. As it stands, this integral equation is non-linear in the unknown $n_e(T)$ (and also in the known $n_\alpha(T)$), and so not soluble, for general K_α, n_α, by any standard inversion techniques. When this is the case it will be most practicable to use (5.15) to explore the compatibility of different models $n_e(T)$ with data P_α^D, as we will illustrate further in section 5.4. However, we first show that, for an

emission region in which $n_e T^{-1/2}$ decreases monotonically, with increasing T, it is possible to transform (5.15) to a standard linear integral equation. The form of this sheds light on the inverse problem and thus on the limitation in the possibility of deriving $n_e(T)$ from noisy data. As in the case of determining $\xi(T)$ from resonance lines (Craig and Brown 1986), the recognition of this limitation allows a systematic evaluation of the level of precision needed in the line flux measurements P_α^D, and in the calculation of the atomic parameters K_α, n_α, to obtain a desired precision in $n_e(T)$.

The transformation will be illustrated for a set, α, of lines in which the upper levels (level 2) are metastable and the lower level is the (single) ground state of an ion. It was shown in the preceeding chapter that, provided there are no strong interactions between the excited states, the function $n_\alpha(T)$ can be expressed as

$$n_\alpha(T) = A_{21}(\alpha) / (C_{21}(\alpha, T) + C_{12}(\alpha, T)) \qquad (5.16)$$

where A_{21} is the radiative transition probability rate between the upper level 2 and lower level 1. The collisional deexcitation rate C_{21} can be expressed as

$$C_{21}(\alpha, T) = \frac{\kappa T^{-1/2}}{\omega_2(\alpha)} \Omega_{12}(\alpha) \qquad (5.17)$$

where κ= constant and $\Omega_{12}(\alpha)$ is a dimensionless quantity referred to as the collision strength. When C_{21} in $cm^3\ sec^{-1}$, and T is in Kelvin degrees we have $\kappa=8.6\times10^{-6}$. Collisional excitation and deexcitation rates satisfy the thermodynamic relation

$$C_{12} = \frac{\omega_2(\alpha)}{\omega_1(\alpha)} \exp(-h\nu_{21} / kT)\ C_{21} \qquad (5.18)$$

where $\omega_{1,2}$ are the statistical weights of the levels 1 and 2, $h\nu_{21}=E_{21}$ is the energy of the transition between the upper level 2 and the lower level 1 and k is Boltzmann's constant.

Since $\frac{\omega_2(\alpha)}{\omega_1(\alpha)} \exp(-E_{21} / kT) << 1$ for values of T at which the ionisation equilibrium contributes significantly to P_α, equation (5.16) can be written approximately as

$$n_\alpha(T)=A_{21}(\alpha)/C_{21}(\alpha,T) \qquad (5.19)$$

The function $K_\alpha(T)$ can be expressed as (chapter 4)

$$K_\alpha(T) = \frac{n_{ion}}{n_{el}} \frac{n_{el}}{n_H} \frac{n_H}{n_e} C_{12}(\alpha, T) . E_{21} \qquad (5.20)$$

where n_{ion} is the ion number density under consideration, n_{el} is the element number density, n_H is the hydrogen number density and n_e is the electron number density.

We emphasise again that, although the above is only physically based for 2-level systems, expressions (5.2), (5.16) and (5.22) give a good numerical description of the n_e, T dependence of more complex systems where the 'constants' are empirically adjusted to give the best fit.

The ratio $\frac{n_{ion}}{n_{el}} \equiv f_{ion}(T)$ has been calculated by several authors assuming ionisation equilibrium for all abundant elements in the solar atmosphere, e.g., Arnaud et al(1985), Jordan(1969,1970) and Jacobs et al (1977,1980). It will be convenient here to represent it by an empirical Gaussian function for the ions under consideration viz.

$$f_{ion}(T)=B \exp(-2((T/T_m)-1)^2) \qquad (5.21)$$

(Another, logarithmic, empirical function has been investigated and this is described in more detail in chapter 7). In (5.21) T_m is the temperature at which $f_{ion}(T)$ is a maximum, and B is the value of f_{ion} at this temperature, the width of the function being $\simeq \frac{1}{\sqrt{2}} T_m$. It is evident from Fig.5.2 that formula (5.21) provides a good fit to the real curves especially over the temperature range where there is a significant contribution to f_{ion} (T).

The quantity $\frac{n_{el}}{n_H} \equiv A_H$ in (5.20) is the element abundance, and this ratio is known quite well for most of the abundant elements in the solar atmosphere, cf. Chapter 1. In regions of the solar atmosphere in which hydrogen is mostly ionised, the hydrogen

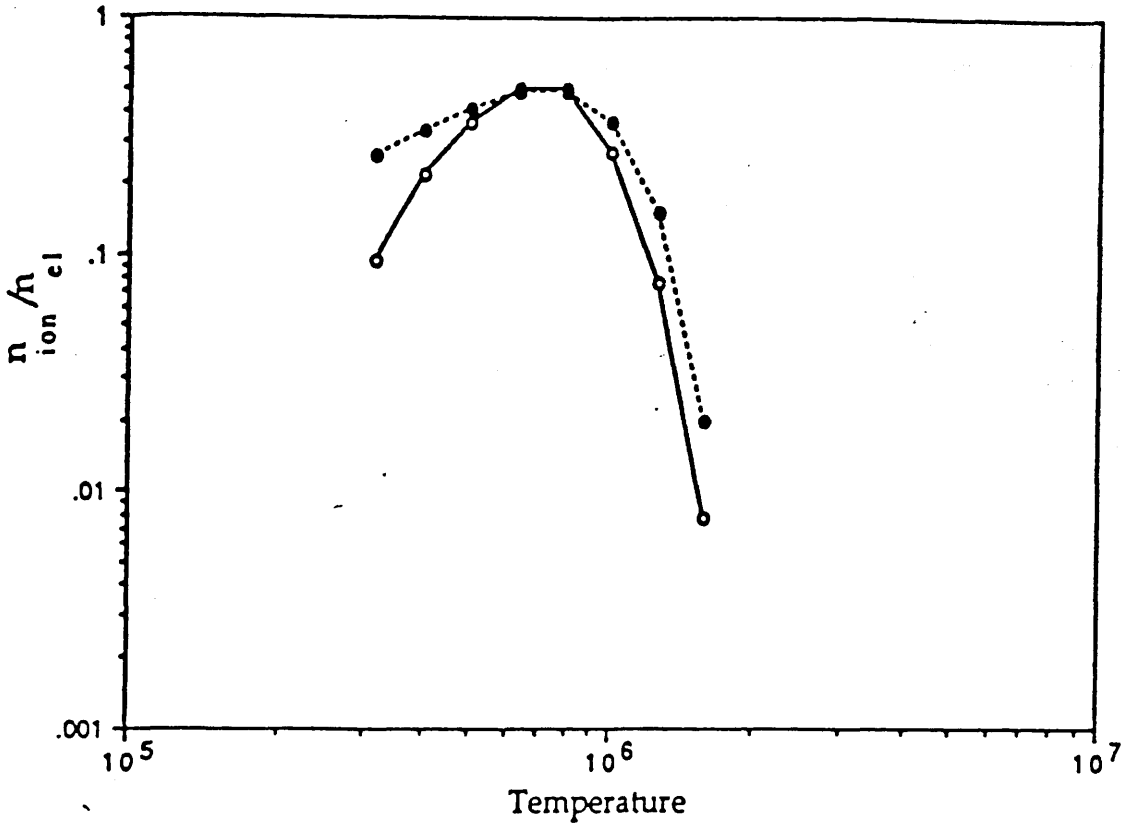

Figure 5.2.The ionisation equilibrium (n_{ion}/n_{el}) of FeIX as a function of temperature. The solid curve is taken from Jordan (1969) while the doted curve is the empirical representation of equation (5.21).

density relative to the electron density, $\frac{n_H}{n_e} \approx 0.8$.

On using the expressions for $n_\alpha(T)$ and $K_\alpha(T)$ given by (5.19) and (5.20), equation (5.15) can be written

$$P_\alpha^D \approx A_{21}(\alpha) . \frac{\omega_2(\alpha)}{\omega_1(\alpha)} . A_H \frac{n_H}{n_e} E_{21} \int_0^\infty \frac{\xi(T) f_{ion} T^{-1/2} \exp(-E_{21}/kT) dT}{\frac{A_{21}(\alpha)\omega_2(\alpha)}{\kappa \Omega_{12}(\alpha)} + n_e(T) T^{-1/2}} \quad (5.22)$$

In treating (5.22) we first define a new variable x, replacing α, to specify the line in the series, where

$$x(\alpha) = \frac{A_{21}(\alpha)\omega_2(\alpha)}{\kappa \Omega_{12}(\alpha)} \quad (5.23)$$

and measure P_α^D for a set of lines covering the range $x > 0$. We also write

$$y(T) = n_e(T) T^{-1/2} \quad (5.24)$$

In practice the density sensitive lines used have a relatively small range of wavelengths, hence in (5.22) we can take $E_{21} \approx \overline{E_{21}}$ and rewrite it as

$$G(x) = \int_0^\infty \frac{h(T) dT}{x + y(T)} \quad (5.25)$$

where

$$h(T) = \xi(T) f_{ion}(T) T^{-1/2} \exp(-\overline{E_{21}}/kT) \quad (5.26)$$

and

$$G(x) = P_\alpha^D / A_{21}(\alpha) . \frac{\omega_2(\alpha)}{\omega_1(\alpha)} . A_H . \frac{n_H}{n_e} E_{21} \quad (5.27)$$

In order to reduce equation (5.25) to standard linear form, we assume an emission region in which $n_e T^{-1/2}$ decreases monotonically as the temperature increases. This in fact is the case for most of the model emission regions discussed in Section 5.4. Then in equation (5.25) T can be replaced uniquely by y as the variable of the integration.

Let $n_e T^{-1/2} \rightarrow y_{max}$ as $T \rightarrow 0$, and $n_e T^{-1/2} \rightarrow y_{min}$ as $T \rightarrow \infty$. Hence (5.27) can be written

$$G(x) = \int_{y_{min}}^{y_{max}} \frac{F(y)\, dy}{x + y} \tag{5.28}$$

where

$$F(y) = -\, h(T)\, \frac{dT}{dy} \tag{5.29}$$

We assume further that as $T \rightarrow \infty$, $nT^{-1/2} \rightarrow 0$, hence $y_{min}=0$. Therefore

$$G(x) = \int_{0}^{y_{max}} \frac{F(y)\, dy}{x + y} \tag{5.30}$$

The formal procedure for finding $n_e(T)$ from equation (5.30) is as follows:

(I) Determine $\xi(T)$ from resonance line measurements, and then derive h(T) from equation (5.25).

(II) Take a trial $y_{max} = y_0$ and solve (5.30) (in principle) for F(y) in $0 \le y \le y_0$ where the function G(x) is given by equation (5.27) in terms of the observed density sensitive line strengths P_α^D .

(III) Solve (5.29) for y(T) with the boundary condition $y \rightarrow 0$ as $T \rightarrow \infty$.

(IV) Calculate $y_1 = y(0)$.

(V) Repeat the cycle (II)--(IV) with different trial values of y_0 until $y_1 = y_0$.

The required variation of n_e with T throughout the emission region is then given by

$$n_e(T) = T^{1/2} y(T) \tag{5.31}$$

This procedure shows that, in the case considered, if $\xi(T)$ is known and sufficiently many lines are observed with sufficient precision, then in principle $n_e(T)$ is determinable from density sensitive line fluxes. In practice the (severe) limitations on

achieving such a solution are set by the following factors :

(a) The differential emission measure function $\xi(T)$ cannot be well determined from resonance line data (Craig and Brown 1976,1986) without imposition of a strong smoothness constraint. This factor is, however, not likely to be too prohibitive because $\xi(T)$ is only involved in the above procedure in the integration of (5.29) in the course of which the errors in $\xi(T)$ will be smoothed out.

(b) Uncertainties in atomic coefficients entering (5.23), (5.26), and (5.27) and errors in the measurements of P_α (hence in G(x)). These will be magnified by :-

(c)The severely ill-posed nature of inverting integral equation (5.30) which is in fact a double inverse Laplace transform L(cf. chapter 4 and Thompson and Sweet 1989) as can be seen by considering

$$G(x) = L\{g(s);\, x\} = \int_0^\infty g(s)\exp(-sx)ds$$

$$= \int_0^\infty \int_0^\infty F(y)\exp(-sy)dy\, \exp(-sx)ds = \int_0^\infty \frac{F(y)}{x+y}dy \qquad (5.32)$$

where F(y) is the inverse Laplace transform L^{-1} of g(s) which is in turn the inverse Laplace transform of G(x). Since the single Laplace transform acts as a strongly filtering kernel, the double transform is much worse. (Quantitatively the ratio of the maximum to minimum eigenvalues, which measures error magnification in the inversion, in the double transform will be the square of that in the single transform). For these reasons we can anticipate that the solution of (5.15) in more general cases than we have analysed, will at best yield very limited information on $n_e(T)$. The best that can be hoped for is to use the data P_α^D to put limits on the possible form of $n_e(T)$. To explore this further we examine in Section 5.4, for several real density sensitive lines, the extent to which widely differing models of $n_e(T)$ predict different P_α^D. This will show whether the differences will be distinguishable in practice.

5.4. Predictions of P_α^D from Different Density Distributions $n_e(T)$

It is well known that resonance line data can at best yield the differential emission measure $\xi(T)$ which, in 1-D, defines only $n_e^2/(dT/dz)$ as a function of temperature

(within a scaling factor dependent on source area). Thus infinitely many density distributions $n_e(T)$ are consistent with a prescribed $\xi(T)$ for a corresponding variation of dT/dz with T. Here we consider the specific question as to whether a set of sources with different $n_e(T)$ but the same $\xi(T)$ are distinguishable using measurements of density sensitive lines. We do so for the specific illustrative case where the varying $n_e(T)$ is parameterised by

$$n_e = n_0\left(\frac{T_0}{T}\right)^{\beta+1} \qquad (5.33)$$

In this expression $\beta = 0$ corresponds to a constant pressure structure, $\beta>0$ to a structure in which pressure decreases with increasing temperature and $\beta < 0$ to one in which it increases with temperature. To exemplify the $\xi(T)$ function we adopt a power law $\xi(T) \propto T^{1/2}$. This form is adopted since it corresponds to a theoretical model of the upper transition region, in which the pressure is constant ($\beta=0$), and which has a constant conductive flux. This power law is in rough agreement with the function $\xi(T)$ in the upper temperature range (2×10^5-1.6×10^6K) as derived from observations of the solar transition region. It thus provides a convenient benchmark with which to investigate the value of β in an observed emission region. In terms of the lower and upper temperatures (T_0, T_1) of the above range, and of the emission measure $\xi_{TOT} = \int_{T_1}^{T_2} \xi \, dT$, the explicit expression is

$$\xi(T) = \tfrac{3}{2}\frac{\xi_{TOT}}{T_0}\,\frac{(T/T_0)^{1/2}}{(T_1/T_0)^{3/2}-1} \quad \text{for } T_0 \le T \le T_1 \qquad (5.34)$$

For future purposes the spatial distribution T(z) may be obtained from (5.4) in the case where $T(\underline{r})$ is a function of ζ only. In this case (5.4) can be written

$$dT/dz = S n_e^2(T)/\xi(T) \qquad (5.35)$$

where S is the area of the emission region. On substituting for $n_e(T)$ and $\xi(T)$ in terms of T from (5.33) and (5.34), (5.35) can be written

$$\frac{dT}{dz} = \frac{2}{3}\left[(T_1/T_0)^{3/2} - 1\right]\frac{n_0^2 S}{\xi_{TOT}}\frac{T_0^{2\beta+7/2}}{T^{2\beta+5/2}} \qquad (5.36)$$

It is noted that when β=0, (5.36) reduces to $T^{5/2}dT/dz$=constant i.e. constant conductive flux as expected. Equation (5.36) can be solved for z giving

$$T(z) = T_0\left[1 + \frac{2(2\beta+7/2)/3}{((T_1/T_0)^{3/2}-1)^{-1}}\frac{n_0^2 S}{\xi_{TOT}}z\right]^{\frac{1}{2\beta+7/2}} \qquad (5.37)$$

where the base of region is defined as z=0. On putting z=L in (5.37), and noting that $L=z(T_1)$ by definition, we have

$$L = \frac{3}{2(2\beta+\frac{7}{2})}\left[\left(\frac{T_1}{T_0}\right)^{3/2} - 1\right]^{-1}\left[\left(\frac{T_1}{T_0}\right)^{2\beta+\frac{7}{2}}\right]\frac{\xi_{TOT}}{n_0^2 S} \qquad (5.38)$$

With $\xi(T)$ given by (5.34), and $n_e(T)$ parameterised by (5.33), the density sensitive line strength (5.15) becomes

$$P_\alpha^D = \frac{3}{2}\frac{\xi_{TOT}}{t_1^{3/2}-1}\int_1^{t_1}\frac{t^{1/2}K_\alpha(tT_0)\,dt}{1+t^{-\beta-1}[n_0/n_\alpha(tT_0)]} \qquad (5.39)$$

where $t=T/T_0$. The factor ξ_{TOT} is a constant of the emission region, and hence is not a function of α. It can therefore be eliminated by considering the line ratio of a pair (α_1, α_2). Thus

$$R_{12} = \frac{P_{\alpha_1}^D}{P_{\alpha_2}^D} = \frac{\int_1^{t_1}\frac{t^{1/2}K_{\alpha_1}(tT_0)\,dt}{1+t^{-\beta-1}[n_0/n_{\alpha_1}(tT_0)]}}{\int_1^{t_1}\frac{t^{1/2}K_{\alpha_2}(tT_0)\,dt}{1+t^{-\beta-1}[n_0/n_{\alpha_2}(tT_0)]}} \qquad (5.40)$$

where $t_1=T_1/T_0$. On using the expressions (5.16)-(5.21) for K_α, n_α (and remembering that the two members of the pair are chosen from the same ion) (5.40) can be expressed in the form

$$R_{12} = H \frac{\int_1^{t_1} \frac{\exp\left(-2\left(\frac{tT_0}{T_m}-1\right)^2\right).\exp\left(\frac{-h\nu_{21}(\alpha_1)}{ktT_0}\right)dt}{1+t^{-\beta-1}\left[\frac{n_0}{(T_0 t)^{1/2}}.J(\alpha_1).\left(1+\frac{\omega_2(\alpha_1)}{\omega_1(\alpha_1)}\exp\left(\frac{-h\nu_{21}(\alpha_1)}{ktT_0}\right)\right)\right]}}{\int_1^{t_1} \frac{\exp\left(-2\left(\frac{tT_0}{T_m}-1\right)^2\right).\exp\left(\frac{-h\nu_{21}(\alpha_2)}{ktT_0}\right)dt}{1+t^{-\beta-1}\left[\frac{n_0}{(T_0 t)^{1/2}}.J(\alpha_2).\left(1+\frac{\omega_2(\alpha_2)}{\omega_1(\alpha_2)}\exp\left(\frac{-h\nu_{21}(\alpha_2)}{ktT_0}\right)\right)\right]}} \quad (5.41)$$

where

$$H = \frac{\Omega(\alpha_1)}{\Omega(\alpha_2)}\frac{\omega(\alpha_2)}{\omega(\alpha_1)}\frac{h\nu_{21}(\alpha_1)}{h\nu_{21}(\alpha_2)} \quad (5.42)$$

and

$$J(\alpha)=\kappa\,\Omega(\alpha)/(A_{21}(\alpha)\omega_2(\alpha)) \quad (5.43)$$

For the temperatures (T_0,T_1) adopted we have t_1=8. Thus, for a given line pair, (5.41) expresses the line ratio as a function of n_0 and β.

As a typical example we consider an emission region with temperature range T_0 =2×10^5 K to T_1 =1.6×10^6 K, within which the above expression for $\xi(T)$ adopted is applicable, and examine the ratio for a range of base densities n_0 and parameters β. A number of ions are selected with peak populations at temperatures spread across, and somewhat beyond, this temperature range and which have well studied density sensitive line pairs around the range of base densities n_0 to be considered. The details of the ions and lines chosen are given in Table 5.1 with the values of the relevant parameters.

In Figs.5.3-5.6 we show the line ratio R as a function of one of the model parameters, viz the electron density n_0 at T_0, for various values of the second parameter β. We have chosen some EUV emission lines which have been used extensively as electron density diagnostics for solar plasmas. These density sensitive line ratios, for a number of ions along different isoelectronic sequences, are OIV (Boron-like ions)-Doschek (1984), SiX (Boron-like ions)-Saha et al. (1982) and Flower et al. (1975), MgVI (Nitrogen-like ions) -Dwivedi (1989) and Bhatia et al. (1980), and FeIX (Argon-

Table 5.1

Atomic data for calculation of line ratios in equation (5.41)

Ion	λ (Å)	A (sec^{-1})	Ω	T_m (K)	ref.
O IV	1407.39	2.13×10^3	0.038	1.26×10^5	1
	1404.81	4.41×10^2	0.109		
Mg VI	387.9	1.1×10^9	0.5103	5×10^5	5
	403.31	3.52×10^9	3.0794		
Fe IX	241.739	$.71 \times 10^2$	0.068	9×10^5	2
	244.911	9.3×10^6	0.041		
Si X	347.43	2.07×10^9	0.71	1.6×10^6	3,4
	356.07	2.2×10^9	1.23		

1 Flower and Nussbaumer (1975). 2.Flower (1977). 3.Flower and Nussbaumer (1975). 4.Vernazza and Mason(1977). 5.Bhatia et al. (1980).

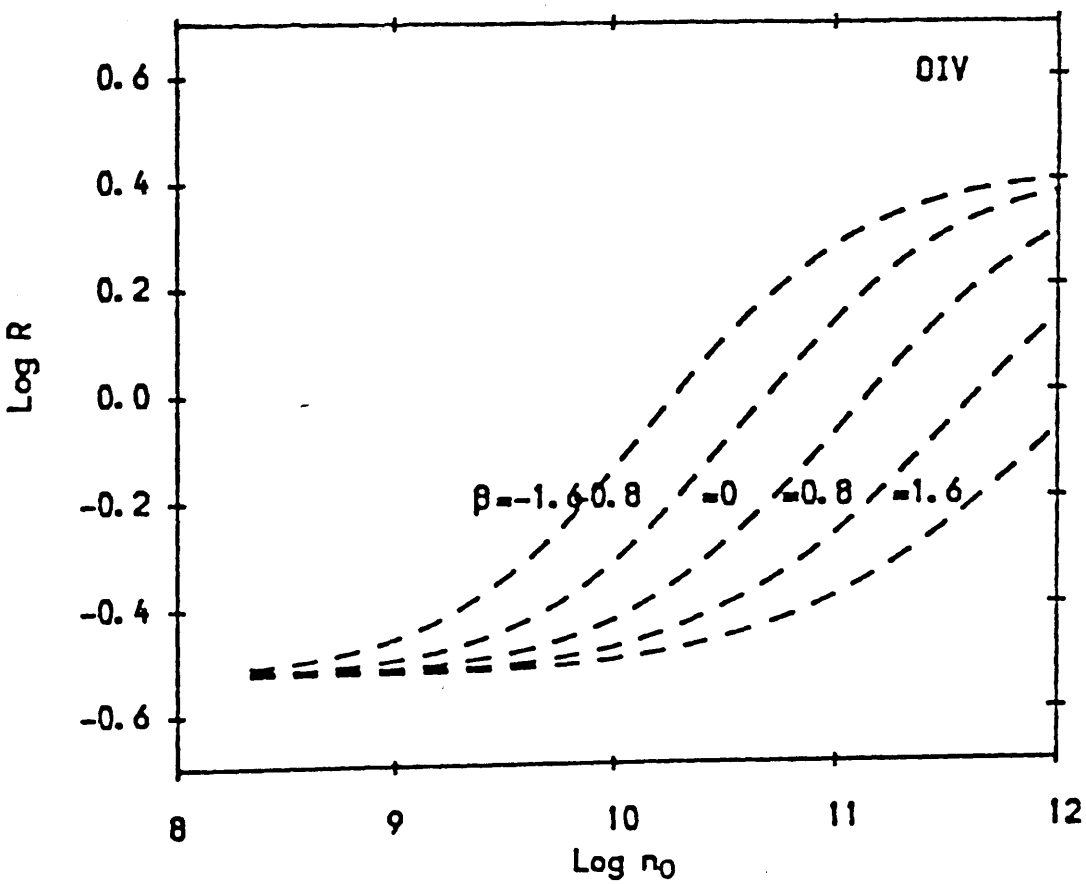

Figure 5.3. Line intensity ratio R as a function of base density n_0 for the line pair (1407.39/1404.81) of OIV.

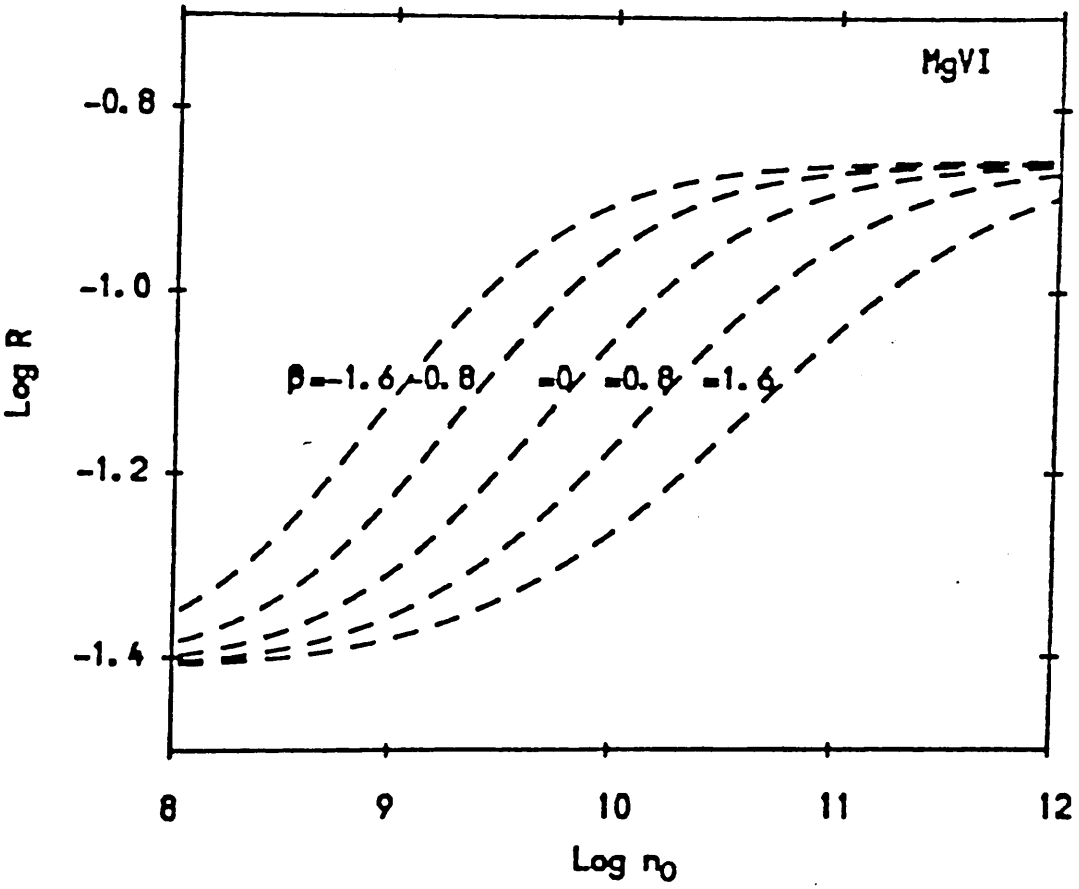

Figure 5.4. Line intensity ratio R as a function of base density n_0 for the line pair (387.9/403.31) of MgVI.

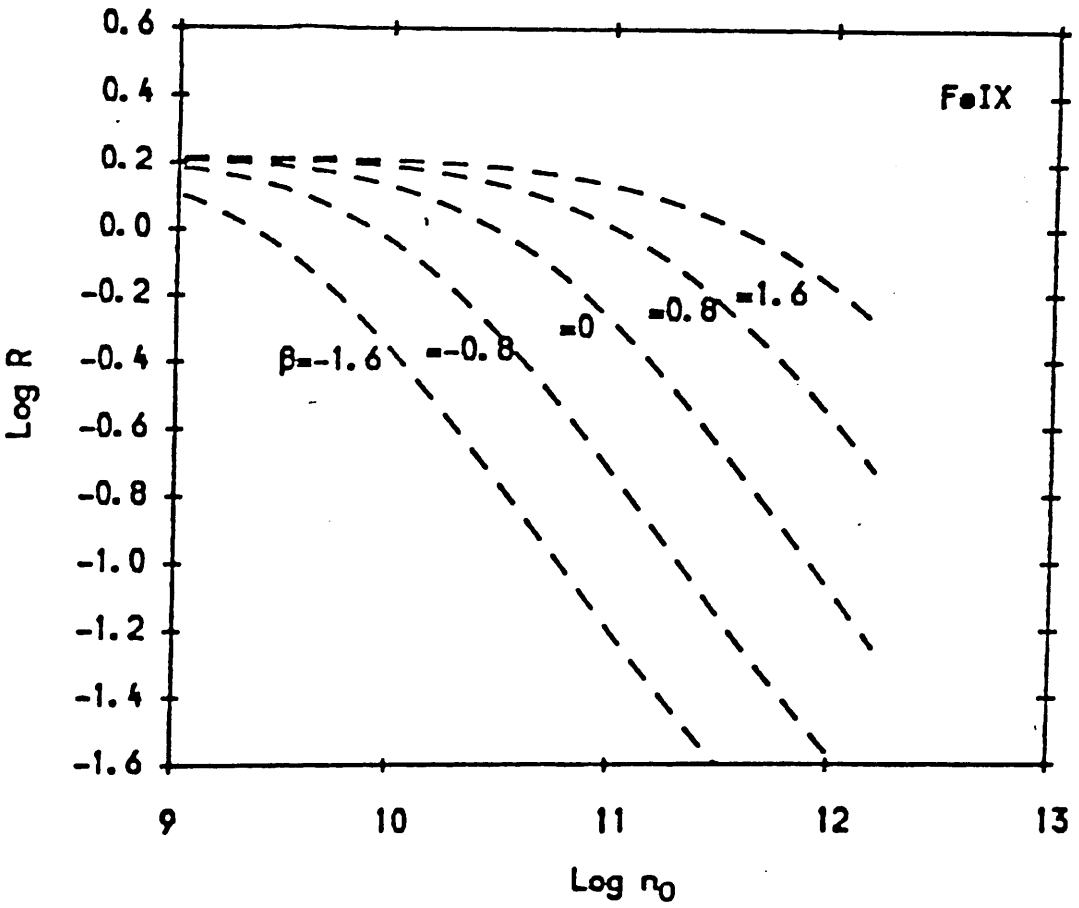

Figure 5. 5. Line intensity ratio R as a function of base density n_0 for the line pair (241.379/244.911) of FeIX.

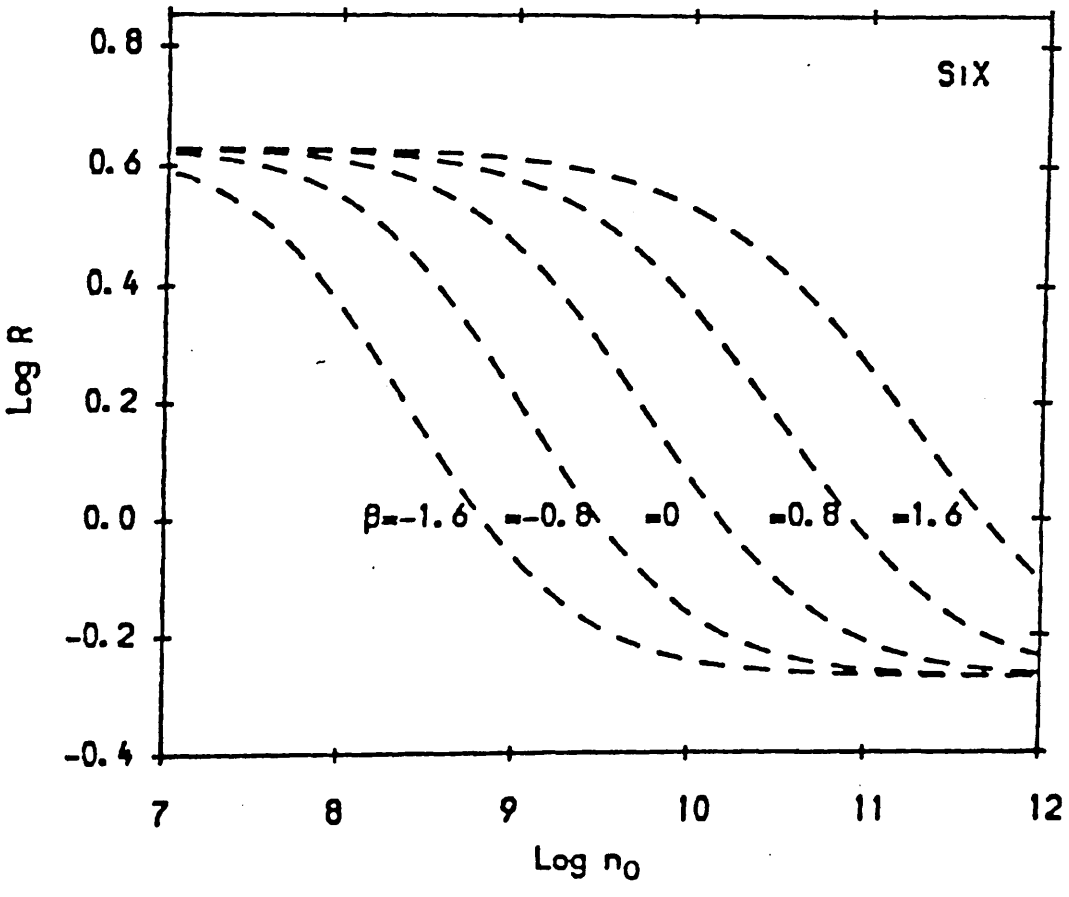

Figure 5.6. Line intensity ratio R as a function of base density n_0 for the line pair (347.34/356.07) of SiX.

like ions)-Feldman et al. (1981) and Dere et al.(1978). These lines span a temperature range of $1.3x10^5$ to $1.6x10^6$ i.e., 13:1. Figures 5.3-5.6 show that the line ratios are sensitive to β and to n_0. Thus sources with different $n_e(T)$ and the same $\xi(T)$ will in fact be distinguishable using density sensitive line ratios, though not from temperature sensitive ratios alone, as speculated at the beginning of this Section.

From Figs.5.3-5.6 it follows that, in terms of the observed line ratio for a given density sensitive line pair, it is possible to infer the value of n_0 as a function of β. Thus if, for a given emission region, the (n_0, β) curves for the observed line ratios of two different ions are found to intersect, this will determine the values of n_0 and β for that emission region. This will be tested for a real emission region in Section 5.5. Further, if three or more such curves intersect in the same place (within errors) then strong support will be provided for the model forms used for, $\xi(T)$, say (if not, the whole analysis can be tried for different $\xi(T)$).

5.5 Application: determination of n_0 and β in the upper Temperature range $T>2x10^5$ K of an observed emission region.

We examine an emission region observed by Skylark SL 1004 rocket launched from Woomera at 04-15 UT on 1973 March 14. The source in question was above the solar limb over a quiet region. The line intensities, in the range 150-870Å, have been taken from Firth et al. (1974). Table 5.2 contains the wavelengths of the lines and their relative intensities.

The (n_0;β) plots for the two ratios, $R_{obs}(FeIX)=1.4$ and $R_{obs}(SiX)=1.0$, are given in Figs. 5.7 and 5.8. As already mentioned in Section 5.4 these ions are active in the temperature range $9x10^5$-$1.6x10^6$ K.

The curves are superposed in Fig.5.9, showing an intersection (albeit at a rather shallower angle than would be preferred). As mentioned this intersection provides a unique value for n_0 and for β for the emission region in question. The resulting values ($n_0=1.3x10^{10}$ cm^{-3}, $\beta=0$) specify the base density and the model parameter of that region

Table 5.2

Observed line intensities (Skylark SL 1004, 1973,March 14)

λ(observed)Å	Identification	Intensity
241.73	Fe IX 241.739	7
244.86	Fe IX 244.912	5
347.39	Si X 347.43	3
356.07	Si X 356.07	3

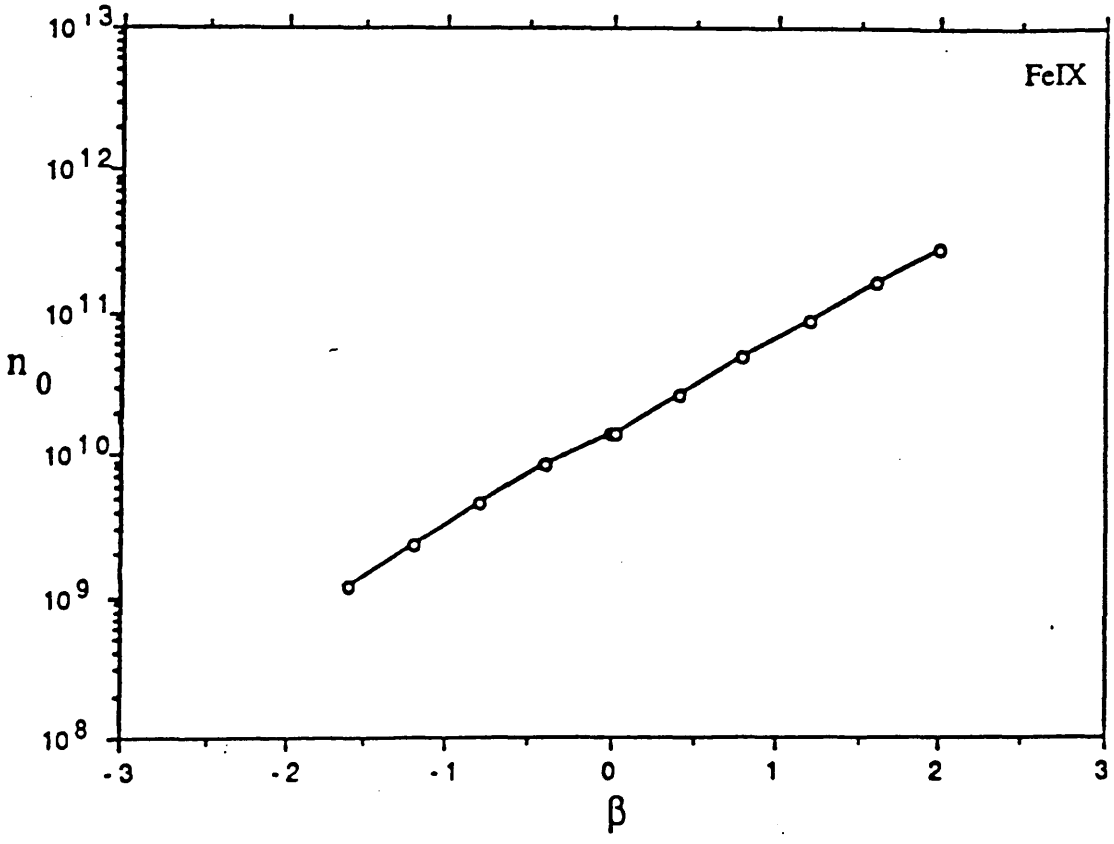

Figure 5.7. The base density n_0 as a function of the model parameter β, for an observed line ratio $R_{obs.}$=1.4 of FeIX.

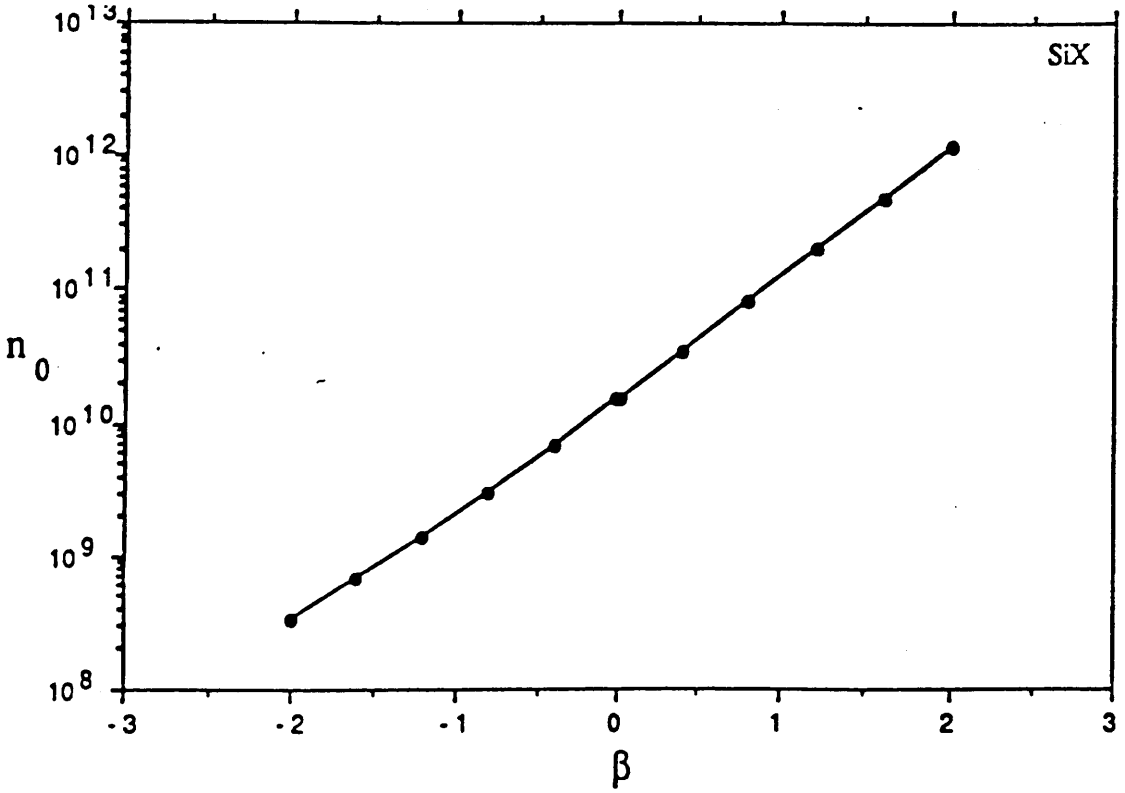

Figure 5.8. The base density n_0 as a function of the model parameter β, for an observed line ratio $R_{obs.}$=1.0 of SiX.

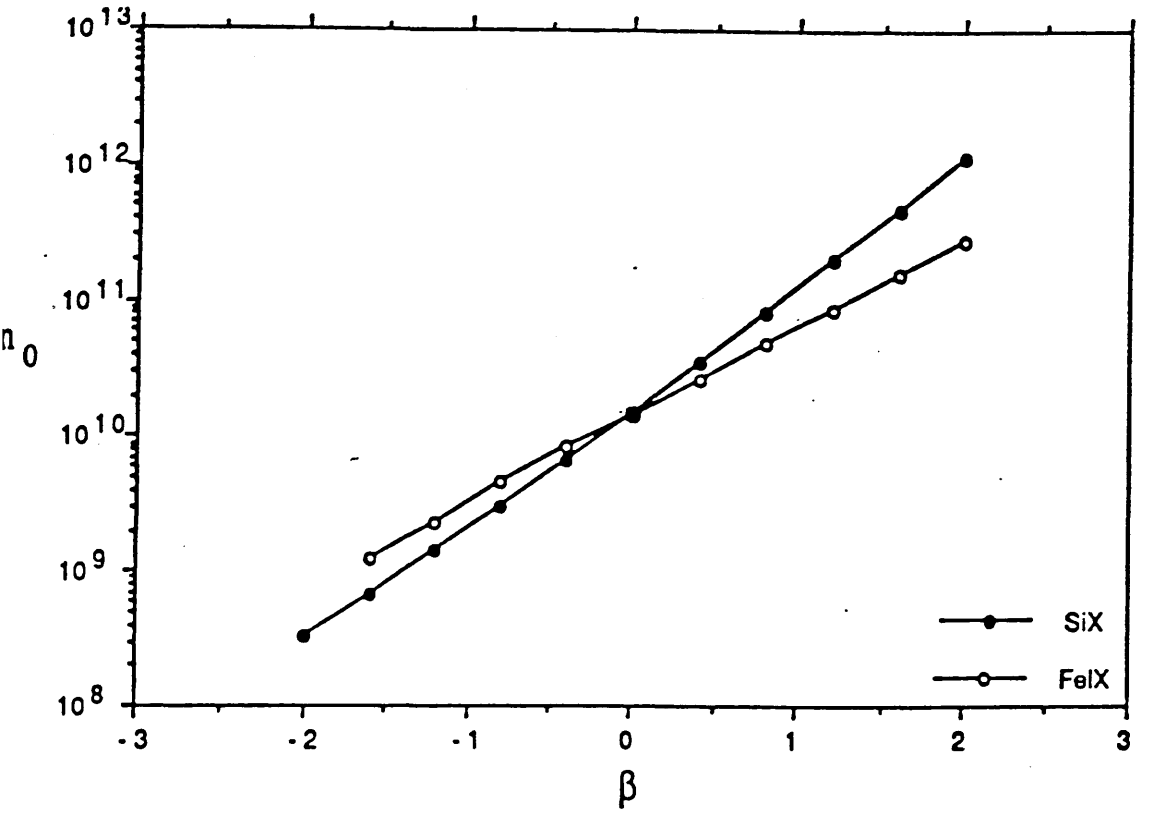

Figure 5.9. Intersection of the two curves, FeIX and SiX, indicating a unique value of n_0 and β for the chosen emission region (see text).

respectively. $n_0=1.3x10^{10}$ cm^{-3} is the electron density in this emission region at temperature $T_0=2x10^5$ K. This corresponds to $P_e=kn_0T_0=0.35$ dynes/cm^2. This value can be compared with a typical value for the quiet sun (Dere and Mason 1981) of $P_e=0.17$ dynes/cm^2. This agreement is very encouraging. It is noted further that the value, $\beta=0$, obtained is also consistent with the theoretical constant pressure model.

5.6 Discussion

We have explored the sensitivity of a density distribution $n_e(T)$ in an emission region as inferred from different line ratios, using a power law model of the form $n_e(T)=n_0(T_0/T)^{\beta+1}$. It has been shown that the parameters involved are very sensitive to the line ratios, thereby demonstrating the possibility of inferring $n_e(T)$ from actual data. The model was tested using the only two line ratios for which the atomic parameters and data on the same source were available. The values of β and the electron pressure were in good agreement with the standard theoretical model of the quiet sun transition region using constant conductive flux. The method would be finally justified if a third observed line ratio intersected reasonably well with the ones discussed above, cf. Fig 5.10. The effectiveness of the method will depend on the size of the ΔABC.

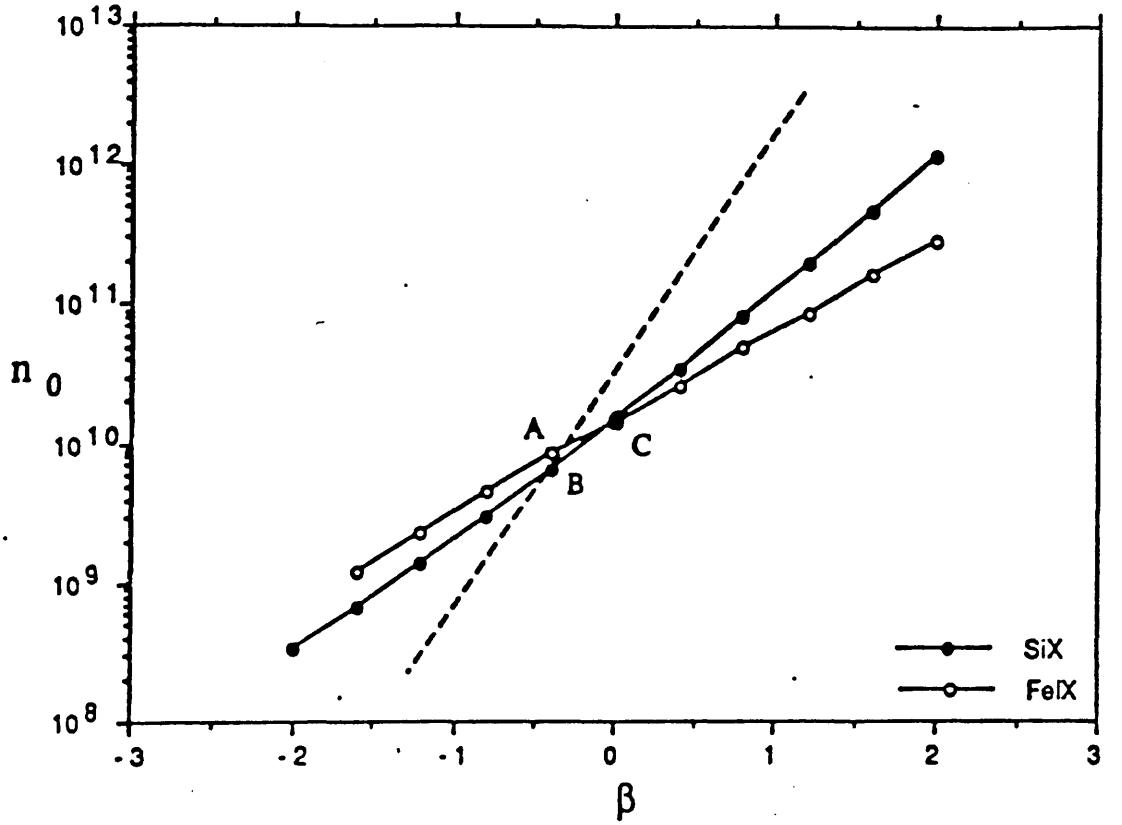

Figure 5.10. The intersection of FeIX, SiX and an assumed (dashed) curve of a third observed line ratio at ΔABC.

CHAPTER 6

BIAS IN PLASMA DENSITY ESTIMATES FROM NOISY LINE RATIO DATA

6.1. Introduction

The main reason for studying the solar spectrum, as discussed in Chapters 1 and 2, is that it tells us much about the characteristics and physical parameters in the solar atmosphere. Electron temperature (T), density (n_e), size of the emitting volume, mass motions and element abundances can all be determined from spectral analysis. Electron density determination in the solar atmosphere using density sensitive line ratios has been one of the most active fields for spectroscopists during the last two decades. These spectroscopic techniques have shed light on the physical conditions of diverse phenomena such as sunspots, flares, active regions, coronal holes and the quiet sun. Unfortunately, density diagnostic techniques are subject to errors affecting the inference of accurate electron densities. These problems may arise owing to uncertainties in atomic data coefficients, to errors in the line intensity measurements, and to lack of high spatial and spectral resolution, as well as to some instrumental errors.

It has been shown by various investigations that using different density sensitive line ratios, for the same source, gives different values for the density. This is due in part to plasma inhomogeneity, which has been dealt with in a detailed manner in Chapter 4, but also to the sensitivity of inferred densities to changes in atomic parameters as discussed by various authors e.g. Dere and Mason (1981), Jordan (1972 and 1974), and Doschek (1984). Jordan (1974), for example, has investigated the effect of uncertainties in atomic data for CIII λ1176/λ977 where errors in electron excitation rate of only 25% can lead to orders of magnitude difference in the electron density deduced. Another example is in the case of the line ratio of two intersystem lines, e.g. O IV, in which an error of 20% in atomic parameters could lead to order of magnitude errors in the electron density (Feldman and Doschek 1979). Therefore, to develop comprehensive density diagnostics we require accurate calculations of atomic data, such as excitation rate coefficients ($cm^{-3}\ s^{-1}$), collision strengths, and spontaneous radiative decay rates for all the different lines under consideration. In addition, of course, instruments with better spatial, spectral, and temporal resolution must continue to be developed. In this Chapter

we will be discussing some of the serious effects of atomic and data noise on the inference of spectroscopic mean densities $<n_e>$. -i.e. on the determination of n_e for a homogeneous plasma. Clearly the effects on determining the distribution of n_e (i.e. $\zeta(n_e)$) in an inhomogeneous case will be even more serious. (cf. Craig and Brown 1986).

Obtaining very accurate electron densities in the EUV range has many problems. For example, some lines which are claimed to have the most accurate atomic data as well as the most accurate observational data, such as O IV and S IV around 1400Å and Si III around 1300Å, suffer from instrumental problems, appearing close in wavelength, and have several lines which may be used for density determination. In addition the actual density sensitivity to line ratios is not very large. For example in the case of the two intersystem lines discussed in Chapter 3, O IV 1407Å/1405Å, the line ratio increases only by a factor of 3 for a density range between 10^{10}-10^{11} cm^{-3}, and by only 1.6 for the range 10^{11}-10^{12} cm^{-3} (cf. Fig 3.3). On the other hand some sources of errors are found even in the case of much greater density sensitivity -such as the ratio of an intersystem to an allowed line in a different ion (e.g. OIV/C IV) in the technique developed by Feldman et al. (1977). Sources of error include inaccuracies of relative element abundances and instrumental calibration problems (Doschek 1984).

For these reasons and others, not only are very accurate atomic data important but so also are very accurate line intensity measurements. Otherwise plasma electron densities may be obtained which differ greatly from the real values, because of statistical biasing and the like.

In order to introduce the topic of this chapter, we will first define some of the statistical terminology that will be used: An estimator can be defined as a rule whereby the value of a parameter is inferred from the data. The estimator of a parameter n_e, say, is defined by $\hat{n}_e$, and its mean or expectation value by $E(\hat{n}_e)$. If there is a difference between the expectation value of the estimator and the true value of the parameter then it is said to be a biased estimator, e.g. if the true value of electron density is n_0, in this example the

bias = $E(\hat{n}_e)-n_0$. The bias in an estimator of any model parameter, which will usually depend on its true value, i.e.n_0, can be found by investigating the probability density distribution of the estimator, which is dependent on the true parameter values and on the data noise level (and distribution).

Our problem can be seen more clearly in the schematic figure (Fig. 6.1), where if a uniform error in the line ratio R_0 is introduced, then $\hat{n}_e$ is found to be nonuniformly distributed about n_0, and the inferred electron densities would tend to be biased toward higher density values. The opposite would be true for very low R values, and only in the narrow central part of the $R(n_e)$ curve is no bias expected.

It is the main purpose of this Chapter to discuss systematically how noise in atomic data and in line intensity measurements can affect the electron densities inferred. We first investigate the biased estimator of the electron density inferred from noisy line ratios by establishing the distribution of inferred n_e values for prescribed line ratios and noise levels of these line ratios. We will utilise the analytic line ratio representation used in Chapter 3, which approximates well to the line ratios under consideration. The study of the bias of the electron density estimator, which depends on the true values of n_0 and on the error distribution of the data, can be achieved by constructing the distribution function of electron density estimated from noisy data, using a numerical simulation. For simplicity we choose the error distribution in line ratio to be a normal (Gaussian) distribution about the true line ratio value (in reality the distribution of errors in R will be more complicated, being the ratio of two photon counts with Poisson noise and systematic errors). We can show (Sec. 6.3), from random sampling of noisy line ratio, the dependence of the inferred mean density on the signal to noise ratio, and hence the resultant bias of the density estimator. We can therefore study what observational (and similarly atomic data) accuracy is required to determine the value for electron densities, with prescribed precision.

The procedure, then, is to simulate uncertain atomic parameter values and intensity line ratio data for different electron densities. This can be done by generating a

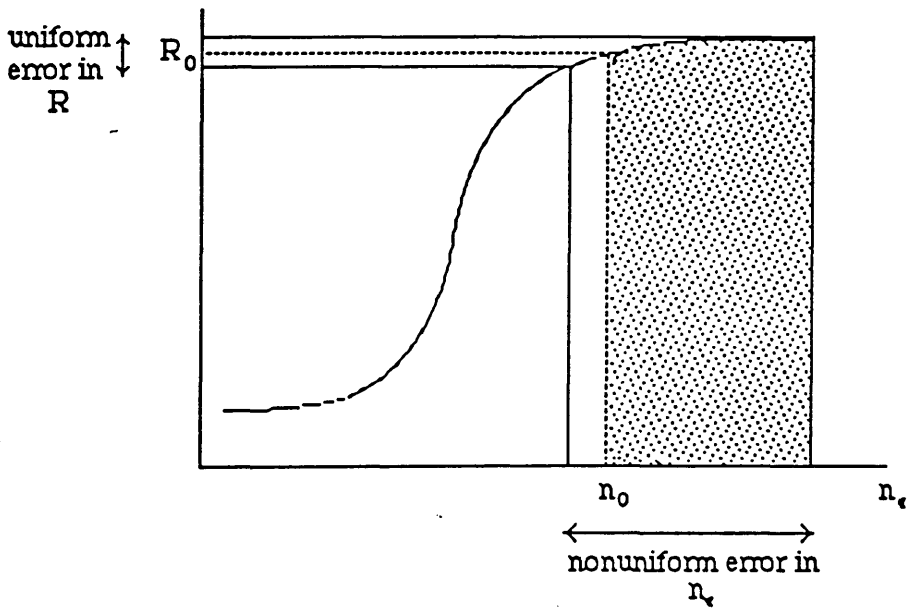

Fig. 6.1 An illustration describing how a uniform error in R may result in a non-uniform error in n_e.

Gaussian distribution of values around the 'true' line ratio R_0 and around true values of the different atomic parameters (n_α, Λ_α, and R_α) cf. Section 6.3. In this Chapter, we will only consider the case of noise in the line ratio parameter R_0, and defer discussion of the effects of noise in the other atomic parameters to a future work.

In section 6.4 we will investigate how to construct 90% confidence interval for the inferred electron density values. In addition, we will show how, from the resultant curves, the bias of the estimated density occurs and the amount of accuracy required in the observed line ratios, in order to obtain reasonable density values.

6.2.Representation and general formulation

If we assume an isothermal situation, the ratio of the intensity of two density sensitive lines formed in an optically thin plasma of uniform electron density n_e can be written as

$$R_{12}(n_e) = R_\alpha \frac{1 + n_e / n_\alpha \Lambda_\alpha}{1 + n_e / n_\alpha} \qquad (6.1)$$

This representation has been adopted in Chapter 3, and the definitions of the various parameters can be found there. Most of the density sensitive line ratios fall into one of two general cases discussed in a detailed manner in Chapter 3. As far as our representation (Equation 6.1) is concerned, these two cases can be simply described as follows. Firstly the case where the electron density increases with the line ratio, $\Lambda_\alpha<1$. As an example for this case we shall adopt O IV, discussed in Chapter 3. Secondly where the electron density decreases with R, $\Lambda_\alpha>1$, and Fe IX has been adopted for this case (cf. Chapter 3). For a detailed physical explanation of these two behaviours, the above Chapter 3 should be consulted. The parameter Λ_α can be expressed as follows

$$\Lambda_\alpha = \frac{n_{\alpha 2}}{n_{\alpha 1}} \qquad (6.2)$$

We note that the uncertainties due to the atomic coefficients arise in the three parameters; R_α, n_α and Λ_α. By measuring n_e in units of n_α, a dimensionless quantity ν will be obtained, viz

$$\nu = n_e / n_\alpha \tag{6.3}$$

Further, by defining the observable line ratio r as

$$r(\nu) = R_{21} / R_\alpha \tag{6.4}$$

and by setting

$$\lambda = \frac{1}{\Lambda_\alpha} \tag{6.5}$$

then the relation between the observable r and the inferred ν quantities can be rewritten as

$$r = \frac{1 + \lambda\nu}{1 + \nu} \tag{6.6}$$

or

$$\nu = \frac{r - 1}{\lambda - r} \tag{6.7}$$

Taking into consideration that $0 \le \nu \le \infty$, Equation (6.7) can be shown graphically for the two common cases of λ, either $\lambda \ge 1$ in which $1 \le r \le \lambda$ as in the O IV ion (Fig.6.2a), or $\lambda \le 1$ where $1 \ge r \ge \lambda$ as in Fe IX (Fig.6.2b).

It is the main purpose of this Chapter to find the best estimate of n_0, given the observation r, by choosing an estimator

$$\Diamond = \frac{r - 1}{\lambda - r} \tag{6.8}$$

It is clear that this estimator gives non-physical results for some values of r. Therefore it is necessary in some way to require that the estimator, $\Diamond$, be applied only to r values such that $1 \le r \le \lambda$ or $1 \ge r \ge \lambda$ as discussed above for the two cases. So that, the inferred value of $\Diamond$ is always physically acceptable. Estimator (6.8), however, is not

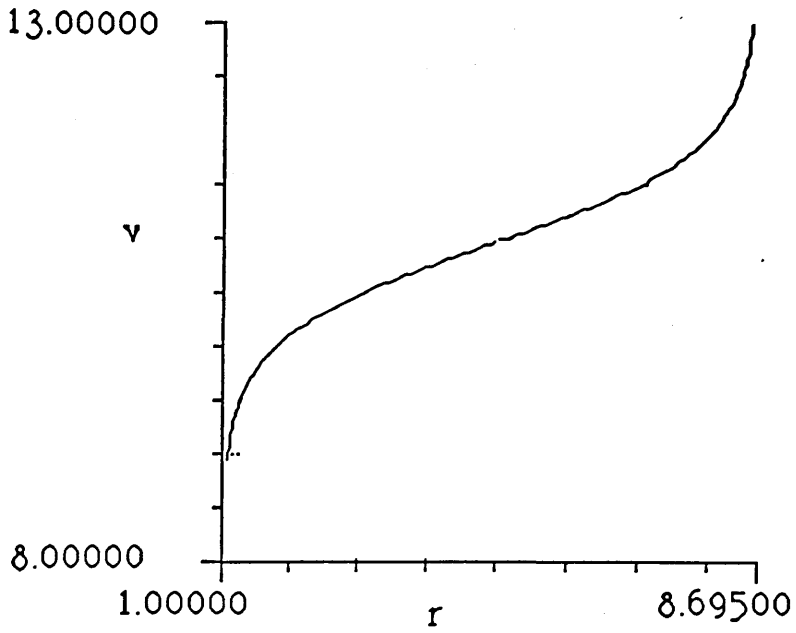

Fig.6.2a The range that should contain the value of r ($1 \leq r \leq 8.695$) in order to give a physically acceptable values of the dimensionless electron density (v), cf. equation 6.7. This curve applies to any line pair with the same λ values as O IV pair, where $\lambda=8.695$.

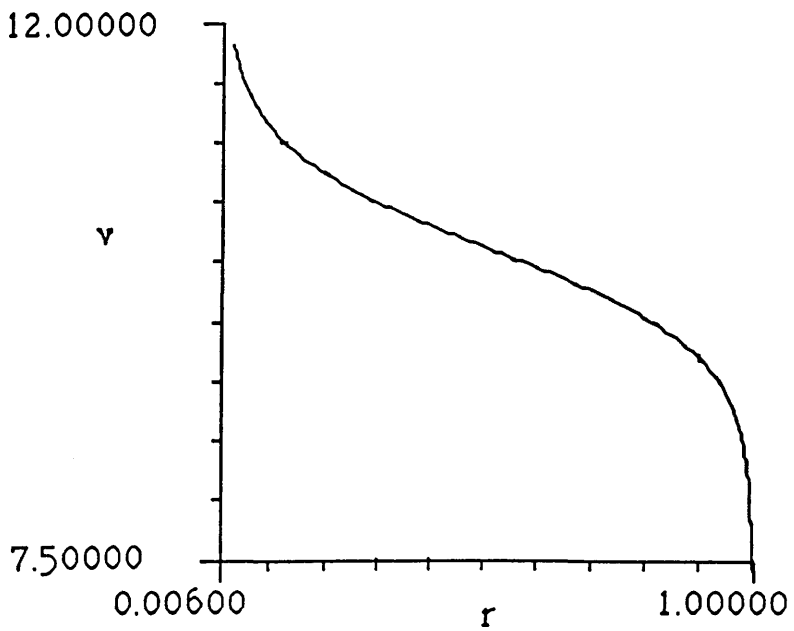

Fig. 6.2b. The range that should contain the value of r ($1 \geq r \geq 0.006$) in order to give a physically acceptable values of the dimensionless electron density (v), cf. equation 6.7. This curve applies to any line pair with the same λ values as Fe IX pair, where $\lambda=0.006$.

necessarily the best (i.e . it is certainly biased ($E(\Diamond) \neq \nu_0$) see Fig. 6.3. We will consider this further in the following section.

6.3.Estimator of plasma density and bias

In the case of a numerical treatment for the biased estimator of electron densities from noisy line ratios we proceed as follows. An approximate frequency distribution for n_0 can be found by means of a computer program to create a normal distribution about the line ratio r_0. This has been done for various values of ν_0 (ν_0 = 0.01, 1.0,100.0) and for a λ value of 8.695, using five thousand noise realisations, i.e. the normal distribution was discretised for numerical tractability into 5000 'bins'.

The generation of the noise on r_0 can be achieved by using a standard library computer program. The library (NAG) routine is one that picks a (pseudo) random number from a normal distribution whose mean and standard deviation are specified by the user. The value of the standard deviation of the normal distribution is a free parameter in the procedure and is given a range of values for each r_0 value.

For different values of r_0 we generate a normally distributed noise around each value with a mean r_0 and standard deviation σ. For each value of σ we create 5000 random number realisations, and then we calculate the mean value of $\Diamond$ for these realisations. By repeating the above procedure for different values of σ we obtain a curve of the expectation values of $\Diamond$, $E(\Diamond)$, as a function of σ/R_0 as in Figs 6.3.

It should be mentioned here that the estimated values of $\Diamond$ which fall outside the physical range (i.e. for which the perturbed r values fall outside the range $1 \geq r \geq \lambda$), are discarded. By doing so the maximum value of $\hat{n}_e$ will not lie outwith the chosen values 1×10^7 and 2×10^{14} cm^{-3} at the lower and higher ends of the line ratio/electron density curve. This discarding procedure is somewhat arbitrary but some such subjective choice must be made in any treatment of noisy data.

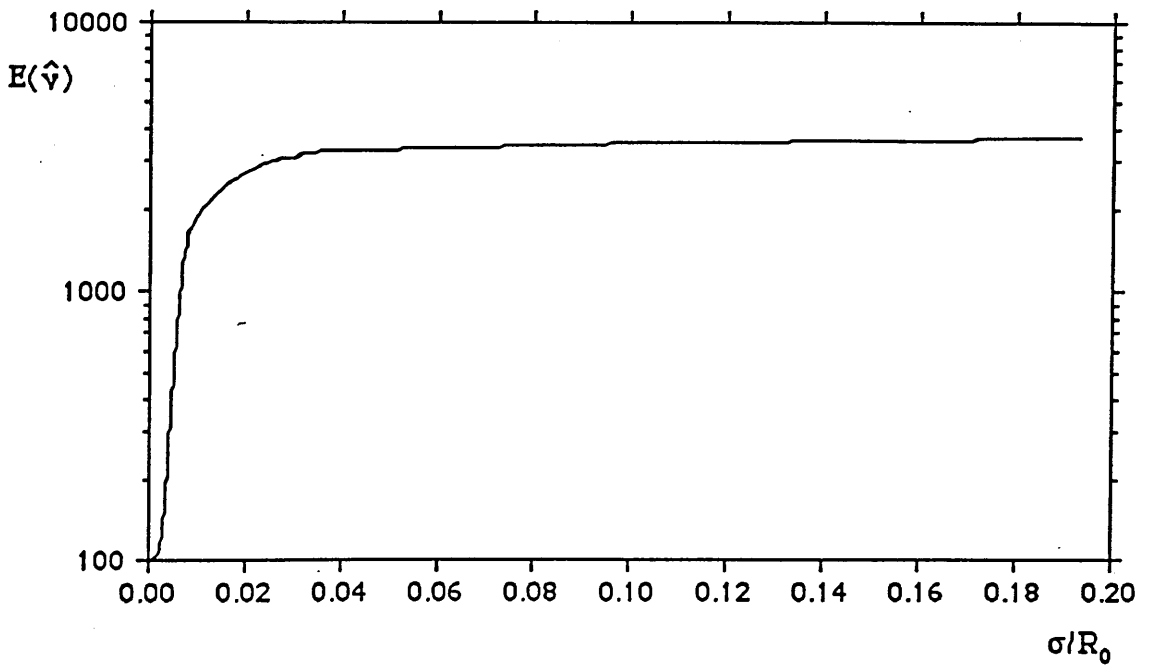

Fig.6.3a Expectation value of the estimator of the electron density plotted against σ/R_0, for ν_0 =100.0.

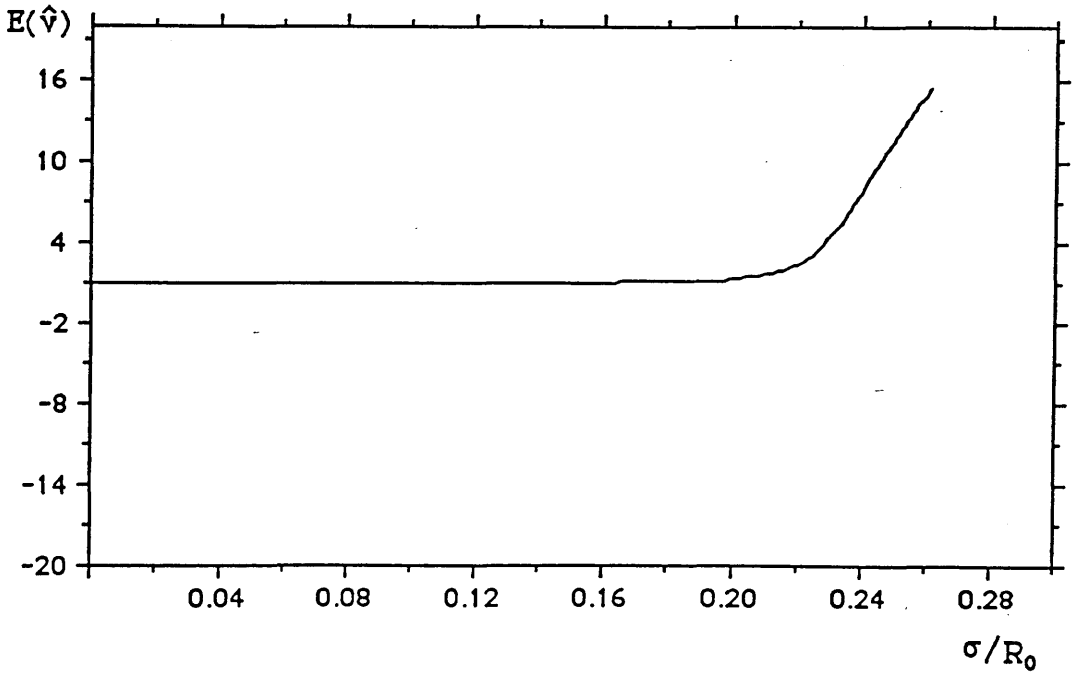

Fig.6.3b Expectation value of the estimator of the electron density plotted against σ/R_0, for ν_0 =1.0.

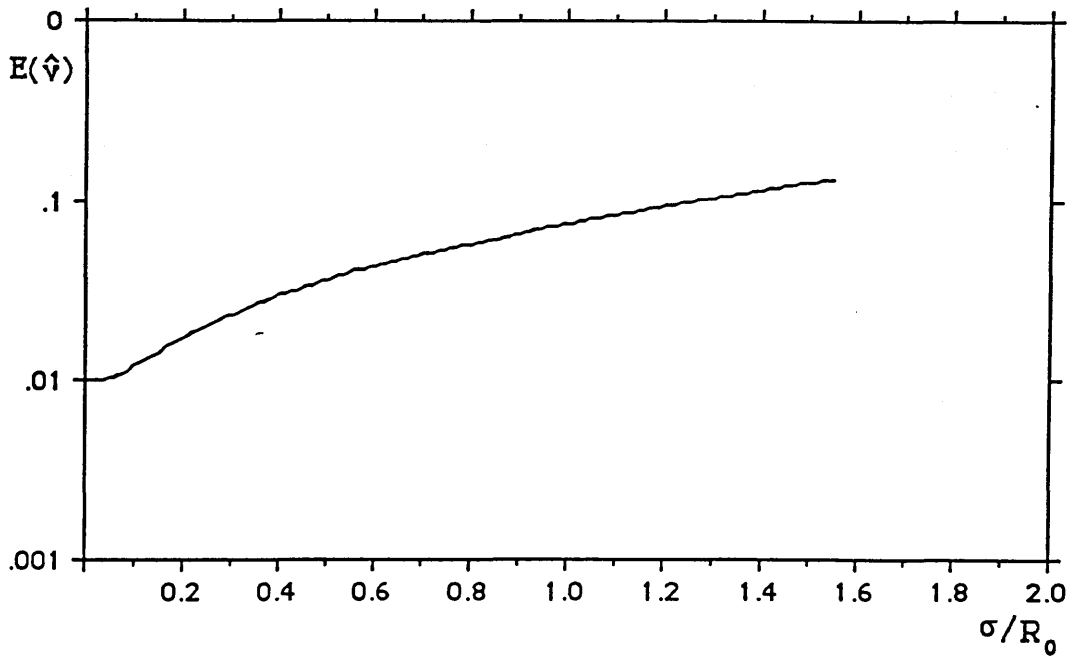

Fig.6.3c Expectation value of the estimator of the electron density plotted against σ/R_0, for ν_0 =0.01.

It is clear from the curves shown in Figs. 6.3, that the expectation value of $\Diamond$ is not equal to the true value v_0. Bias is greatest for values of v_0 near the end points of the line ratio-electron density curve (Fig. 6.1), e.g. v_0=0.01, or=100. On the other hand at the optimum density sensitive range of the curve the bias only becomes significant at much higher values of σ, since at this part of the curve (Fig. 6.1) a uniform error in R will approximately result in a uniform error in n_e, Fig. 6.3b. In the case where v_0=100, even for low noise levels the estimator $\Diamond$ is seriously biased toward high density. For example, a noise of 5% on R will give us an inferred electron density of $\sim 1.x10^{14}$ cm^{-3} instead of $n_e=8.738x10^{12}$ cm^{-3}, (cf. Fig 6.3a). It is evident from this example, that the estimated density is of a factor of 12 higher than the true value. Therefore, we need a very high degree of accuracy in order to obtain reasonable values of inferred electron density.

6.4. Confidence intervals

By a 90% confidence interval for v_0 we shall mean a rule by which an interval can be constructed so that the probability of the interval containing the true value v_0 is exactly 90%.

A confidence interval can be obtained by constructing a histogram for the frequency of $\Diamond$ at each value of v_0 for fixed σ, and then taking the 5% and 95% quantiles, as illustrated in the Fig. 6.4 (By constructing a confidence interval of 90% we obtain the results presented in Figs. 6.5, for different values of σ (0.001, 0.003, 0.006)). A confidence interval for electron density is found by drawing a line from the measured value of $\Diamond$ parallel to the v_0-axis. The upper and lower limits of the confidence interval are then indicated by the v_0 coordinates of the points of intersection of this line with the 5% and 95% quantile curves. As an example, in Figs 6.5, the 90% confidence interval is shown for $\Diamond$ =50. In Fig. 6.5a the (σ=0.001) confidence interval

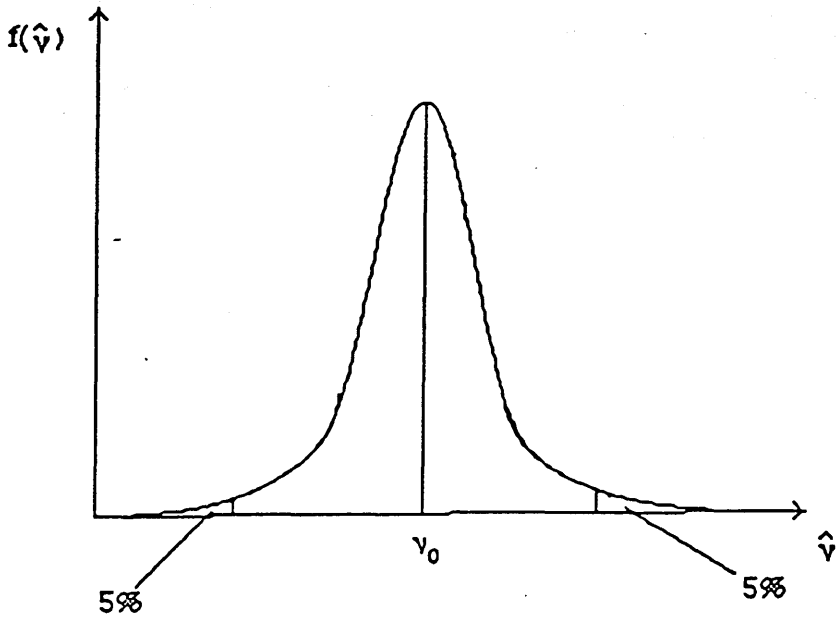

Fig. 6.4. An illustrative curve showing how confidence interval can be constructed, for each value of ν_0 and σ.

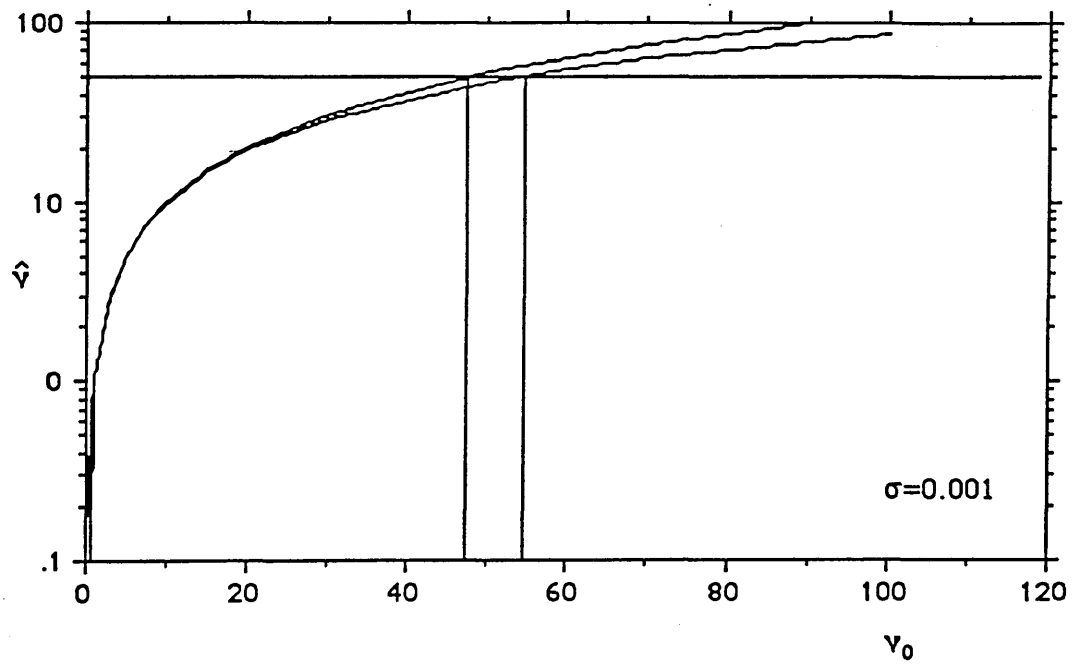

Fig. 6.5a Confidence interval for the inferred electron density ν_0 at the 90% level, for σ=0.001.

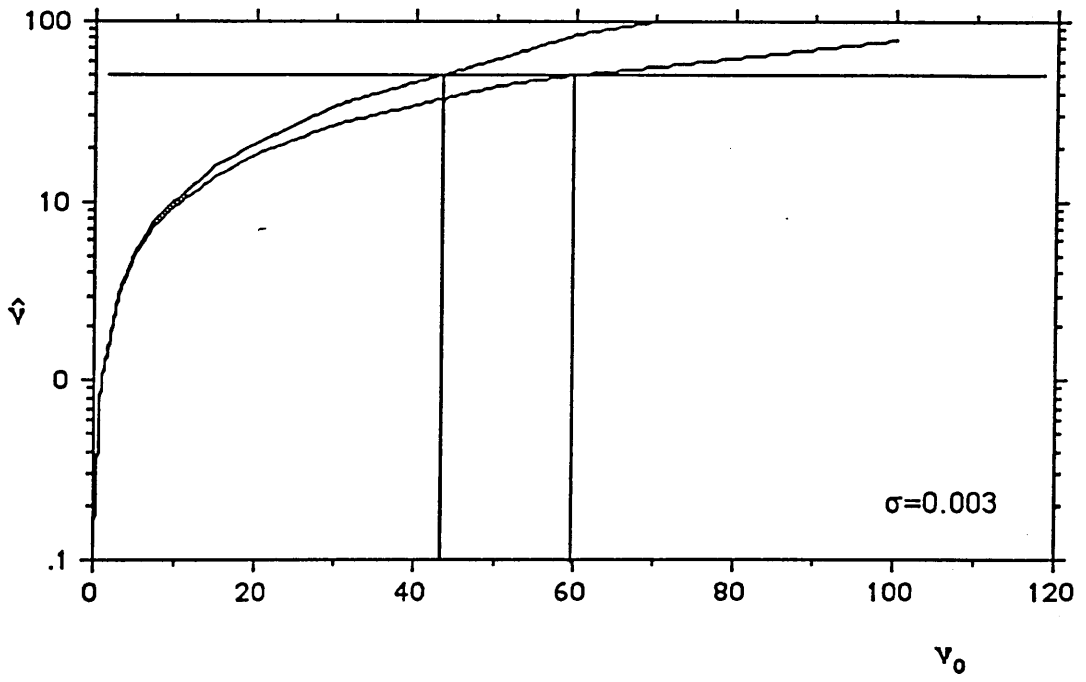

Fig. 6.5b Confidence interval for the inferred electron density ν_0 at the 90% level, for σ=0.003.

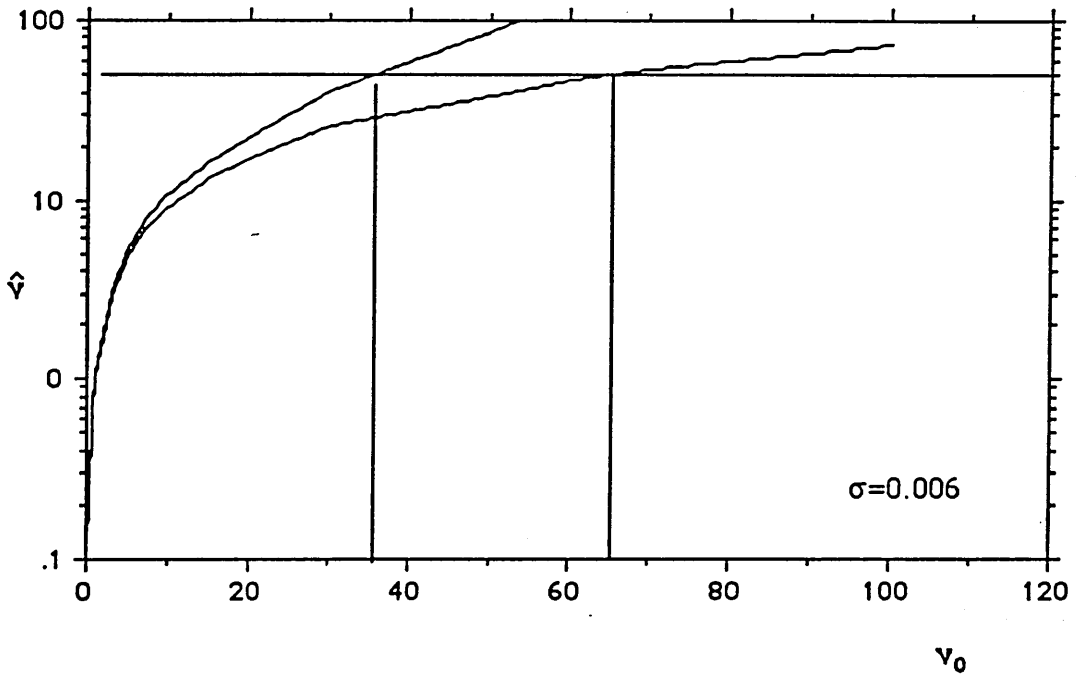

Fig. 6.5c Confidence interval for the inferred electron density ν_0 at the 90% level, for σ=0.006.

is [48, 55]. In Fig. 6.5b (σ=0.003) the confidence interval is [43.5, 59], and for the last considered case here (σ=0.006) , as in Fig. 6.5c, the confidence interval is [37,66].

The above figures indicate that for larger values of σ, the confidence interval curves tend to get broader, indicating that the expectation of the estimated density is certainly more biased. This is can be most conveniently represented in graphical form (Figs. 6.6). Here we plot the upper and lower 95 per cent confidence limits as a function of data standard deviation, σ, for different values of ν_0. It is clear from Fig. 6.6 that at any given σ the confidence interval for electron density rapidly broadens as ν_0 increases to higher values. Consequently the error on the data has to be very much smaller at higher values of electron densities to determine ν_0 with any reasonable accuracy.

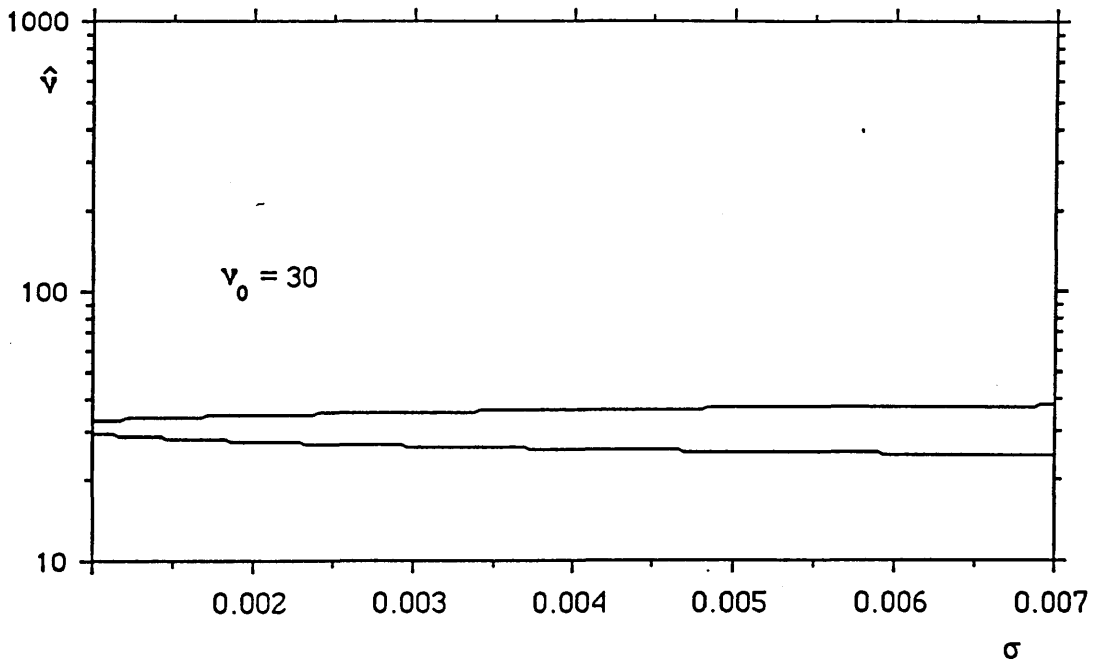

Fig. 6.6a Graphical representation of the confidence interval for a value of ν_0=30 (95 per cent confidence) as a function of σ.

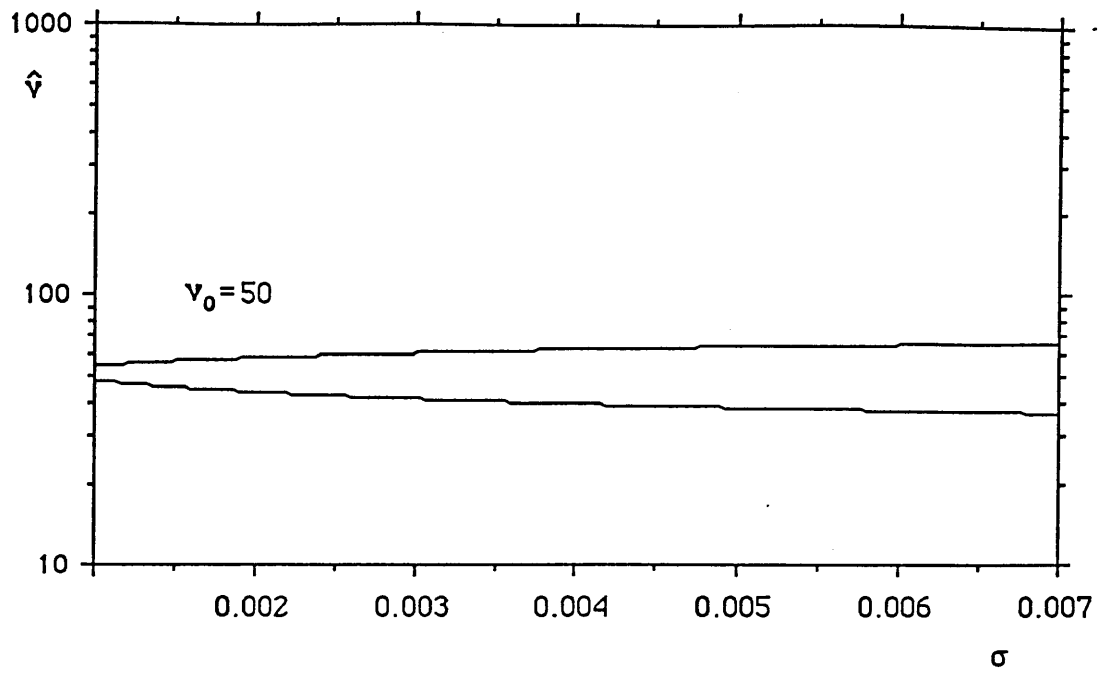

Fig. 6.6b Graphical representation of the confidence interval for a value of ν_0=50 (95 per cent confidence) as a function of σ.

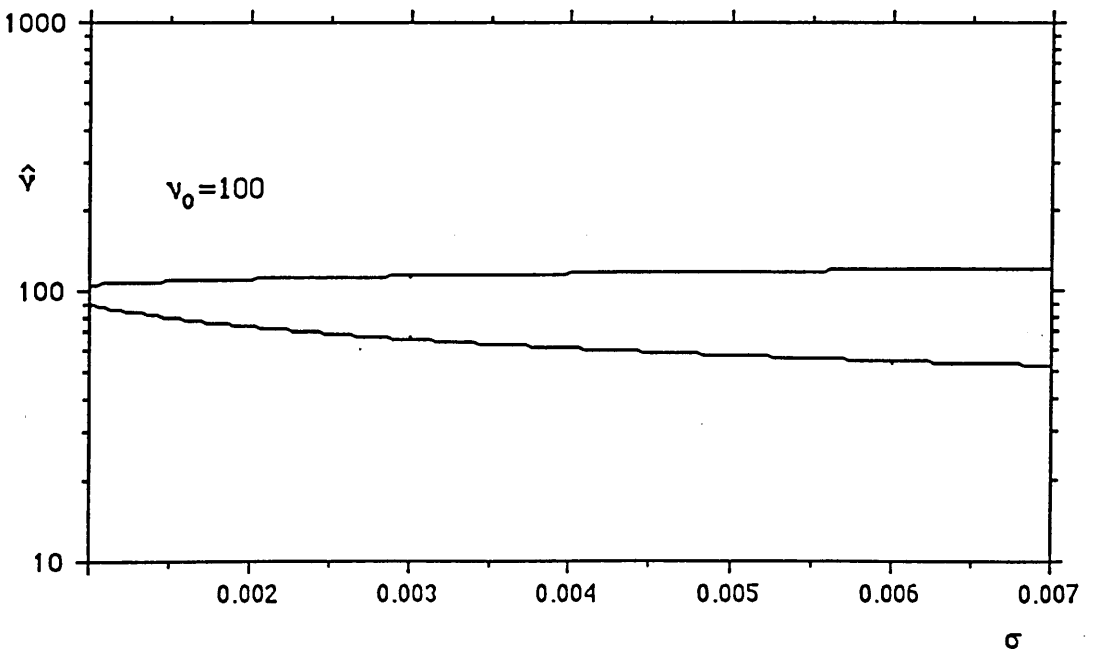

Fig. 6.6c Graphical representation of the confidence interval for a value of ν_0=100 (95 per cent confidence) as a function of σ.

On the other hand the confidence interval has been constructed for larger values of σ (0.01, 0.06, 0.4), shown in Figs. 6.7. It is obvious from these Figs that the confidence interval does not contain the true value (=100). For example, in Fig. 6.7a the (σ=0.01) confidence interval is [33.5, 78.5], in Fig. 6.7b (σ=0.06) the confidence interval is [5.5, 24], and for the last case (σ=0.4), Fig. 6.7c, the confidence interval is [1, 9]. Thus indicating the bias at large σ of the estimator $\hat{\nu}$.

It is evident from these results that, in addition to uncertainties in the electron densities, data errors can lead to a biased estimate of n_e. Therefore, it is necessary to consider the accuracy in measuring line ratios and in calculating the related atomic data.

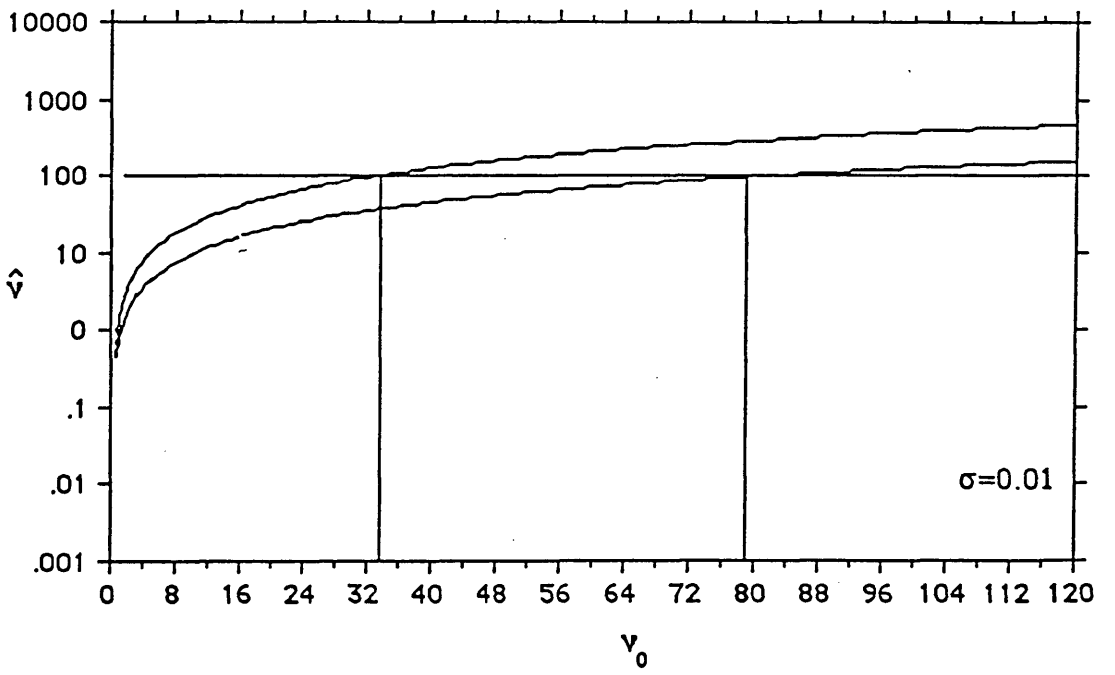

Fig. 6.7a Confidence interval for the inferred electron density ν_0 at the 90% level, for σ=0.01.

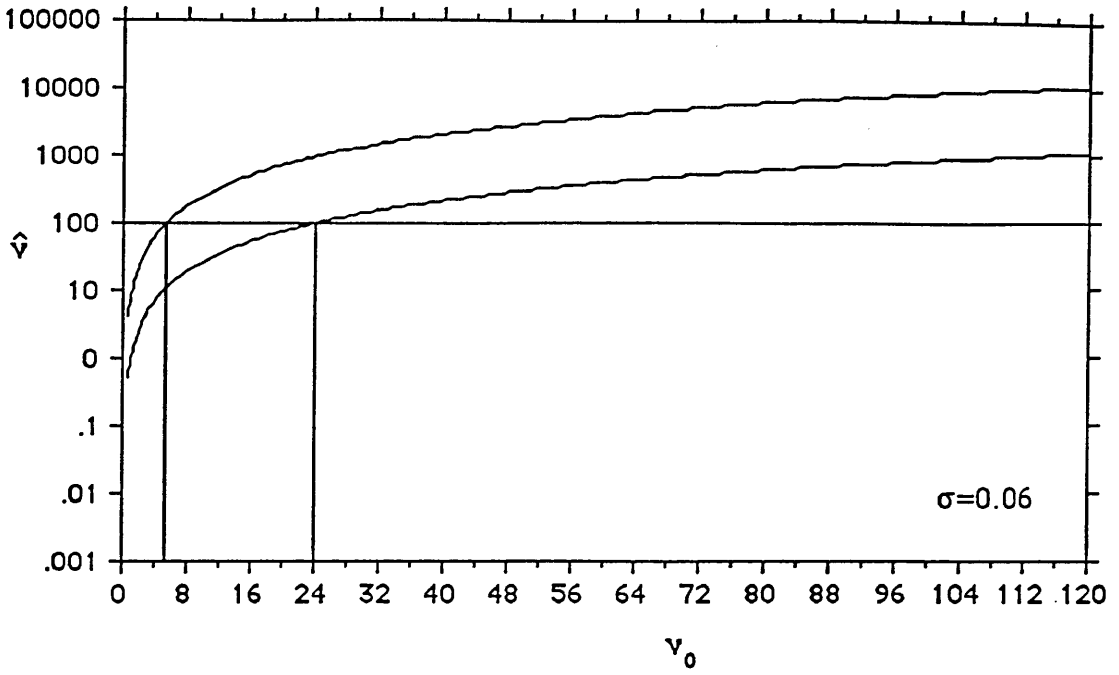

Fig. 6.7b Confidence interval for the inferred electron density ν_0 at the 90% level, for σ=0.06.

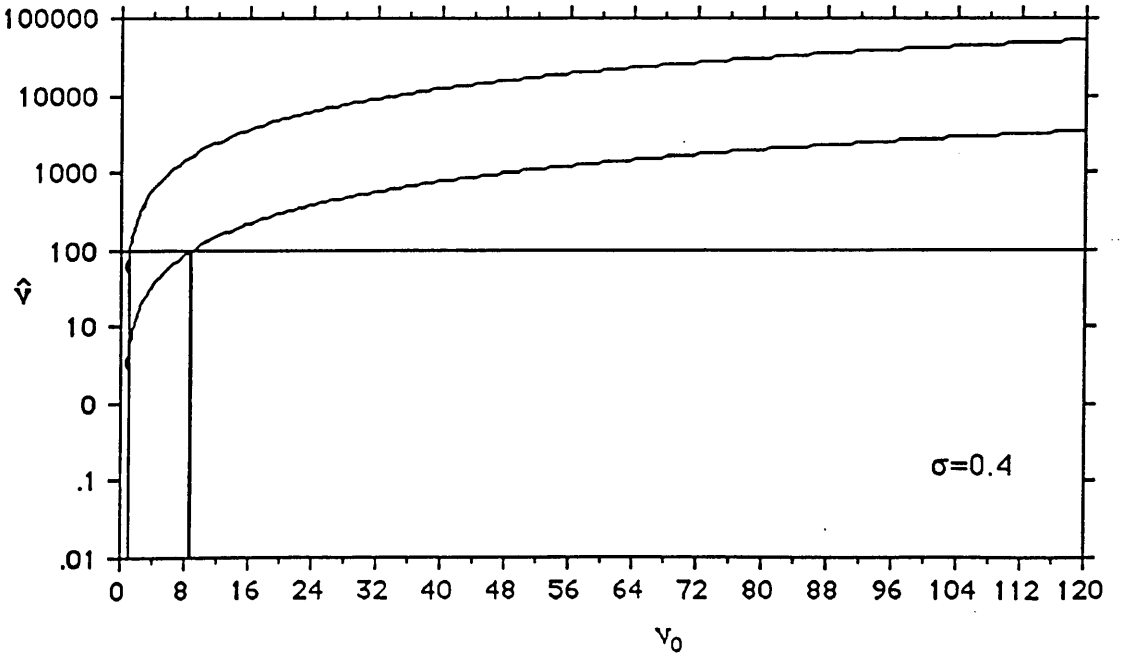

Fig. 6.7c Confidence interval for the inferred electron density ν_0 at the 90% level, for σ=0.4.

6.5. Conclusion

In this Chapter the importance of paying particular attention to the accuracy needed when observing density sensitive line intensities has been discussed, as well as accuracies in atomic data. We concentrated here on the noise on the line ratios, and how the inferred electron densities are very sensitive to even very small noise on the line ratios. This noise can result in a seriously biased estimator of electron densities.

Often it is important to establish the accuracy of a particular inference, in which case the confidence interval is appropriate for this purpose. We, therefore, have constructed a confidence interval for v_0, when σ is assumed to be known. At high values of σ, these intervals are both broader and skewed relative to those for smaller σ, which emphasises that the estimated density is certainly biased. This is also the case for larger values of v_0. Finally it should be emphasised that when data errors are present in line ratio measurements (or in atomic data parameters) even the mean of a very large number of measurements does not necessarily result in the true answer, i.e.a biased estimator does not converge on the true value.

CHAPTER 7

FUTURE WORK

7.1.Introduction

In this Chapter we would like to outline the possibilities for future research based on the work described in the preceding chapters of this thesis. Much of our work has been of an innovative nature and requires further investigation for the full potential of the methods developed to be realised.

The following few pages are an attempt to discuss briefly some of the possible extensions to this thesis, as well as some related points from the different chapters upon which we may elaborate.

7.2.Noisy data

The effect of noise on the line intensity measurements has been discussed in detail in Chapter 6. Various sources that may affect the inferred electron densities, apart from line ratios, also exist in the different parameters used in the reciprocal representation discussed in Chapter 3. These parameters include n_α, Λ_α and R_α, and their effects can be investigated in a similar way to that of the noisy line ratio. An investigation of the effect of noise on these parameters and how it biases the inferred electron density would be extremely useful. The results obtained could be compared with those of line ratio biasing in order to determine which of the above parameters has the most effect on the inferred electron density and hence, the necessary accuracy required. The above investigation can also be applied to the second case of line ratio/electron density curves, in which R decreases with increasing electron density, i.e. $\lambda > 1$.

7.3. Density Sensitivity Representations

In Chapter 5, we used a power law model of the form $n_e(T)=n_0(T_0/T)^{\beta+1}$ to explore the sensitivity of the density distribution $n_e(T)$ in an emission region, as inferred from line ratios. The parameters were found to be very sensitive to different line ratios. This model was tested using the only two line ratios for which the atomic parameters and data on the same source were available and thus the method would be better justified if

other observed line ratios could be found.

We have also explored the sensitivity of the density distribution $n_e(T)$ to line ratios, utilising an exponential formula to represent the ionisation equilibrium that appeared in equation (5.15). Another, and more accurate representation can be used for this purpose. The logarithmic representation will be investigated shortly, and a comparison with the empirical Gaussian function will be rather useful.

The ionisation equilibrium, that has been discussed in Chapter 5, may also be represented by a logarithmic empirical function, viz.,

$$f_{ion}(T)=10^{(A-B(\log T-\log T_m)^2)} \qquad (7.1)$$

where T_m is the temperature at which $f_{ion}(T)$ is a maximum. A and B are constants [obtained from a simple fitting procedure such that 10^A is the value of $f_{ion}(T)$ at the maximum temperature while B is a measure of the temperature 'width' of $f_{ion}(T)$ such that when $\log(T/Tm)=\frac{1}{\sqrt{B}}$, $f_{ion}=0.1\ f_{ion}(max)$].

In order to proceed with the investigation of the problem addressed in Chapter 5, this representation proved to be a convenient function for the purpose of representing the real curves of ionisation equilibrium which have been discussed by many authors, mentioned in the text of Chapter 5. The fitting of this formula is shown in Fig. 7.1 for OIV which provides a good fit to the real curve produced by Jordan (1969). Therefore, it would be rather useful to apply this function in equation (5.41) by means of which we can examine the sensitivity of the density distribution $n_e(T)$ as inferred from line ratios. Thus a comparison can be made, utilising the two different ionisation equilibrium representations.

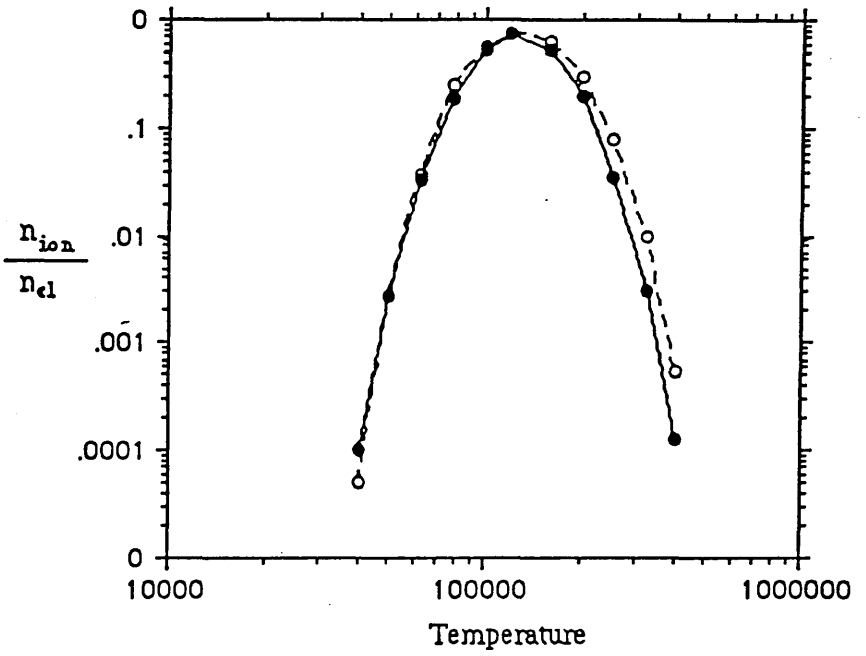

Fig. 7.1 The ionisation equilibrium (n_{ion}/n_{el}) of O IV as a function of temperature. The solid curve is produced by Jordan (1969) while the dotted curve is the empirical representation of equation (7.1).

A further, interesting possibility of elaborating the work in Chapter 5 is that of determining the spatial nature of an emitting region. Following Equations (5.37) and (5.38) we can obtain some very useful information, namely, the spatial distribution T(z) of an observed emission region as well as the length (L) of that region.

In Section 5.5, the possibility of determining the values of n_0 and β in the upper part of the transition region has been considered. An important extension is to investigate the lower part of the transition region in a similar way to the above.

In the transition region the curve for the variation of $\xi(T)$ with temperature has been obtained by a number of authors (e.g., Jordan 1976, Gabriel 1976). This curve, shown in Fig. 7.2, has a minimum value at around 10^5 K and indicates that the transition region can be divided into upper ($T > 2x10^5$) and lower ($2x10^4<T<2x10^5$) regions. In the higher temperature range the differential emission measure $\xi(T) \alpha T^{1/2}$. This form has been adopted in Chapter 5 to exemplify the $\xi(T)$ function in the upper part of the transition region. The $\xi(T)$ function in lower part of the transition region is of the form

$$\xi(T) \alpha T^{-4} \qquad (7.2)$$

This formula can be used and tested for a real emission region and the obtained values (n_0, β) compared with that of the different theoretical models existing for this part of the transition region.

In addition, by combining both formulae of the theoretical models of the lower and the upper parts of the transition region, we can construct a function to exemplify $\xi(T)$ for the whole transition region. Thus we can investigate the values of β and n_0 in an observed emission region, with temperature range $T_0=2x10^4$ to $T_1=1.6x10^6$ K, and within which the constructed expression for $\xi(T)$ is applicable.

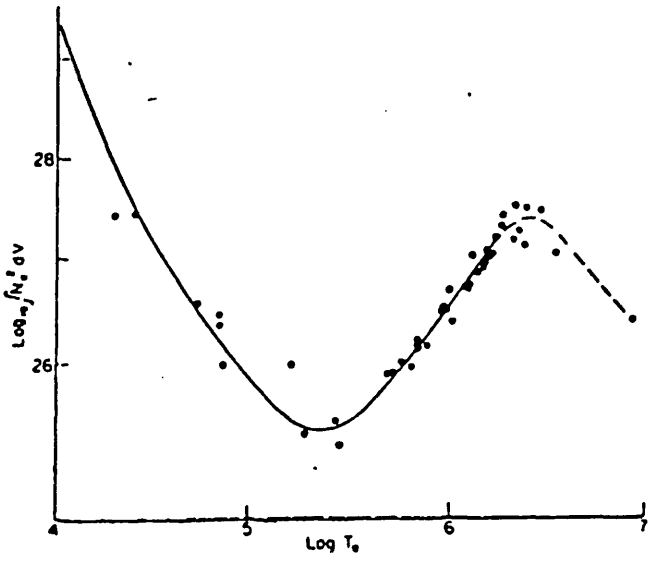

Fig. 7.2 Differential emission measure derived from absolute intensities of observed spectra.

GLOSSARY

SPECTROSCOPIC TERMINOLOGY

Introduction

This glossary is intended for the benefit of those readers who are new to the field of spectroscopy. It is not meant to be a comprehensive study but rather a short discussion of the more basic and relevant aspects of plasma radiation and atomic processes that occur in high temperature low density plasmas. These different processes result in the emission of radiation which provides useful information about the properties of the plasma under study. A great deal of work has been devoted to the study of the different aspects of plasma spectroscopy. The subject is as broad as plasma physics itself, and we shall make no attempt to cover the entire field here. Our intention is merely to give the reader a general idea about some of the atomic definitions that are often used in plasma physics, and mostly to define some of the spectroscopic terminology used in this thesis.

G.1.Plasma radiation

The plasmas we consider consist mainly of electrons and protons with atomic hydrogen, and atoms and ions of heavier elements present to a smaller degree. The collisions between the minor constituents are neglected, since they are rare compared to collisions involving the electrons and protons. Because electrons have much greater velocities and since the rate coefficients are the product of collision cross section with velocity, electrons are usually much more effective than protons in causing collisional transitions among the states of atoms and ions. When the density is low, a rather simple model, which acquires its name from its applicability to the solar corona, may be used. In coronal equilibrium the fundamental approximation is that all upward transitions are collisional and all downward transitions are radiative.

The interaction of electrons with other particles in the plasma results in the emission of radiation. In this thesis, the considered radiation is in the form of discrete spectral lines, rather than the continua of free-electron radiation which we will discuss shortly. It was the study of these spectral lines that originally led to the formation of the

quantum theory of atoms. The emitted radiation gives much useful information about the plasma, such as electron and ion temperature and density, and has been discussed in both Chapters 1 and 2. Because of their high velocity, electron interactions tend to dominate the collisional excitation and ionisation processes. Three electron transitions may occur during these interactions.

Bound-Bound transition (line radiation)

If the ions in the plasma are not completely ionised, emission of energy will occur in the form of excitation radiation. This occurs when an electron attached to such an ion can absorb energy, e.g. as a result of collision with a free electron, and thus this bound electron will be raised to an excited state. When this excited electron returns to a lower quantum state it will emit a photon of a given wavelength determined by the separation of the energy levels. This process is known as the spontaneous decay of an excited ion or atom to a lower level.

Free-bound transition (Radiative Recombination)

This atomic radiation occurs when an electron in the continuum recombines with an ion. Because the radiation corresponds to the radiative capture of a free electron into a bound level of an ion or atom this is called free-bound recombination. The upper level is continuous so the resulting radiation is continuous. However, there is some structure (edges) in the spectrum due to the discrete nature of the lower energy levels.

Free-Free transition (Bremsstrahlung)

Bremsstrahlung is a continuous radiation emitted by charged particles, mainly by electrons as a result of deflections by the Coulomb fields of the other charged particles present. Since the electron is free before its encounter with an ion and remains free subsequently, the transitions are called free-free, and since the initial and final states are continuous, the bremsstrahlung spectrum is also continuous.

The last two processes give rise to continuum radiation of intensity given by the sum of terms made up of products of the electron number density, the relevant ion number density and an atomic coefficient that depends on the structure of the ion and the electron temperature. The calculation of spectral line intensities, on the other hand, is more complicated since consideration should be given to the processes by which the upper level of the transition is populated.

G.2. Atomic Processes

In order to determine quantum state populations it is important to consider the detailed atomic processes populating and depopulating each state. There are several such processes.

Collisional Ionisation

When a free electron with kinetic energy greater than the ionisation potential of the target (atom or ion) strikes this target one of the things that may occur is that a bound electron can be knocked out and become free (ionisation). The probability is expressed numerically by the 'ionisation rate coefficient' S such that the product n_e x n x S is the number of ions suffering ionisation per second per cm^{-3}, where n_e is electron density, and n is ionic number density. The cross-section for this reaction σ, is often used to measure the importance of this process for a given plasma. However, it is also possible and, in fact, more convenient in plasmas, to use the ionisation rate coefficient S rather than cross section. These are related by $S=\langle\sigma.v\rangle$ where the average is taken over the velocity v distribution of the electrons which is generally assumed to be Maxwellian and therefore S is a function of electron temperature. Rate coefficients are generally expressed in $cm^3\ s^{-1}$.

$A^{+}+e \rightarrow A^{++}+2e.$

Collisional excitation

When a free electron of kinetic energy less than the potential energy of the target strikes the target a bound-bound transition from a level of lower energy to a level of higher energy will occur. A measure of this process is again the rate coefficient for this transition. The term collisional deexcitation is used for the inverse process. The rate coefficient of the collisional excitation and its relation to the collisional deexcitation is given in section 1.1.2 of this thesis.

For reviews of the electron collisional excitation the relevant references should be consulted, such as Gabriel (1972), Van Regemorter (1962). When accurate atomic data is required reference should be made to one of the atomic data Banks, e.g. Daresbury Laboratory of the Science Research Council.

Dielectronic recombination

When an electron collides with a charged atom with an energy slightly below the excitation threshold it may cause excitation and simultaneously be captured into a high bound state (since it does not have enough energy to escape from the Coulomb field). This occurs when the incident electron excites the parent ion initially in some level, 1 to level 2 by giving its energy to an electron in the bound level 1. The free electron then enters some high bound level denoted by 3. This is the first step of dielectronic recombination, and may be denoted as

$$A\ (z+1,\ 1) + e \rightarrow A\ (z,\ 2,\ 3)$$

where A is the ionic species and z is the charge of the ion.

The inverse process to capture is autoionisation where the ion makes a radiationless transition back into its ground level and an electron is ejected. Dielectronic recombination becomes effective when the excess energy of the ion is removed by a spontaneous radiative transition subsequent to the capture (stabilisation), before the system has time to autoionise, i.e.

$$A(z, 2, 3) \rightarrow A(z, 1, 3) + h\nu(1, 2) \text{ (stabilisation)}$$

Finally the captured electron cascades down to a lower level emitting a line known as a satellite line.

It has been shown by the calculations of Burgess (1964) that dielectronic recombination is important for solar atmospheric physics and should be considered in deducing coronal temperature from analyses involving ionisation ratios. Work on dielectronic recombination has been reviewed by Seaton and Storey (1976) and Burgess (1964, 1965).

Spontaneous radiative decay

Spectral lines arise from the spontaneous radiative decay of an electron from an upper to a lower bound level. The coefficient used to describe the rate of this process is the spontaneous transition probability. It is given by the symbol A_{ji} and measured in s^{-1}. The rate of spontaneous radiative decay (per cm^{-3} per sec.) may be used in determining the intensity of a spectral line, which is given by the product $n_j A_{ji}$ where n_j represents the population density of ions with charge z in the excited level j.

The radiative lifetime τ is the reciprocal of the sum of all the radiation coefficients affecting the level in question, viz.,

$$\tau_j = \frac{1}{\sum_{n=i} A_{ji}}$$

The values of the A_{ji} coefficients depend on the details of the atomic structure of the atoms or ions and their calculation and measurement are important for atomic physics. Calculations of this coefficient was reviewed at the Bureau of Standards in Washington (cf. Fuhr and Wiese 1969, Wiese et al. 1966)

Radiative Recombination

Radiative recombination is a two body process and takes place when a free electron in the field of a positive ion makes a radiative transition to a bound level thus forming an ion or atom of charge one less than the initial charge, i.e.

$$n(z)+e \rightarrow n(z-1)+h\nu$$

The photon carries a way the kinetic energy of the electron before recombination plus the ionisation energy of the final bound level, i.e.

$$h\nu=X-E_j-\varepsilon$$

where X is the ionisation potential of the ion in its ground state in eV, E_j is the energy of the final bound level j from the ground state and ε is the kinetic energy of the electron. Thus the recombination continuum spectrum is characterised by discontinuities due to the ionisation energies of the relevant bound levels.

The inverse process of radiative recombination is photo-ionisation, and the rate of the occurrence of this process is proportional to the radiative flux.

G.3.Different Spectroscopic Terminology

Metastable levels:

Metastable levels are also known as long life time levels. They are defined as the levels in which the collisional deexcitation processes are comparable to the radiative decay rates, and they are more highly populated than the ground levels. The lifetime of a metastable excited state is typically greater than 10^{-6} sec.. A more practical definition in terms of collision phenomena might be a state whose natural lifetime is comparable with the mean collision time of the particle in a specified plasma. For example, the $2\ ^1S$ state of helium, whose natural lifetime is 38 ms, is metastable in a typical helium discharge where the mean collision time is of the order of microseconds, but it is not considered metastable in the plasma of a planetary nebula, where the mean collision time is about 3

hours. On the other hand, the $2\,^3S$ state of helium whose natural lifetime is about 10^6 seconds, is metastable in both plasmas.

Allowed lines:

Allowed lines are the strongest emission lines, they are known as electric dipole transitions with $\Delta L=\pm1$ and $\Delta J=0, \pm1$ (without spin change) where L is the orbital quantum number and J is the internal quantum number, and whose upper levels are excited by electron collisions from the ground state. In these sort of transitions the radiative decay rates always greatly exceed the collisional decay rates, therefore collisional deexcitation is negligible.

Forbidden lines : These are defined as the lines for which the transition disobeys the quantum selection rules (e.g. j=0 to j=0). They may also be defined as the lines that result from transitions of electric quadrupole (and higher) and magnetic dipole (and higher). The corresponding transition probabilities $A_{j'-j}$ are about 10^5 times smaller than for electric dipoles. Fig. G.1 shows a forbidden line at 22.1 Å for O VII.

Intersystem or intercombination lines:

If a decay happens from a metastable level indirectly, by transfer first to another level, then the resultant transition is known as an intercombination transition. Intersystem lines usually result from a combination of singlet and triplet terms, and are weak compared to the electric dipole transitions. As an example, in the case of He-like ions (Fig.G.1) the ^3S metastable level can decay indirectly, by transfer first to the 1s2p $^3P_1$ level, followed by the intercombination transition to the ground level (McWhirter 1984). Fig. G.1 , shows energy levels for He-like ions, demonstrating an intersystem transition. Following Gabriel (1972), this line and the others (the resonance line, the quadrupole line, and the forbidden line) have been designated Y, W, X , and Z, respectively. In Fig. G.2. one of the He-like ions (O VII) spectrum recorded by McKenzie et al. (1980) is given showing an intercombination line at 21.8 Å.

Satellite lines.

Some excited states of X-ray transitions are produced not by collisional excitation, but instead directly by dielectronic capture. These lines arise primarily as a consequence of dielectronic recombination of He-like ions but can also be due to innershell excitation of the corresponding Li-like ions. They are mainly used as a diagnostic method for the determination of electron temperature. As has been shown above, the dielectronic recombination process is made up of three stages, viz., capture, stabilisation, and cascade. It is the stabilisation process that can give rise to the satellites.

Statistical weight : The number of electrons that can occupy a level without violating Pauli's exclusion principle. ($\omega=2J+1$).

Steady state : The population of each atomic level is constant in time and hence determined by the balance of processes populating or depopulating it. But, in flares and prominences the population of the levels varies with time. The steady state can be reached in roughly $10^{12}/n_e$ sec, which is about 1/10 sec. for a typical Tokamak plasma.

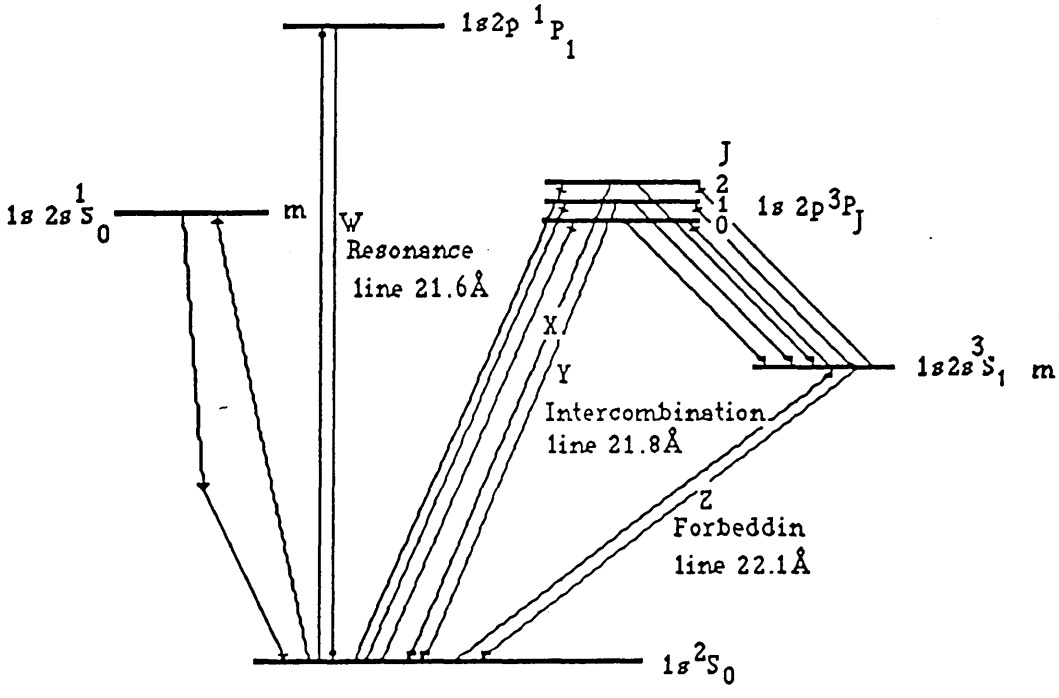

Fig. G.1. Energy levels for a helium-like ion (O VII), showing the different lines discussed in the text.

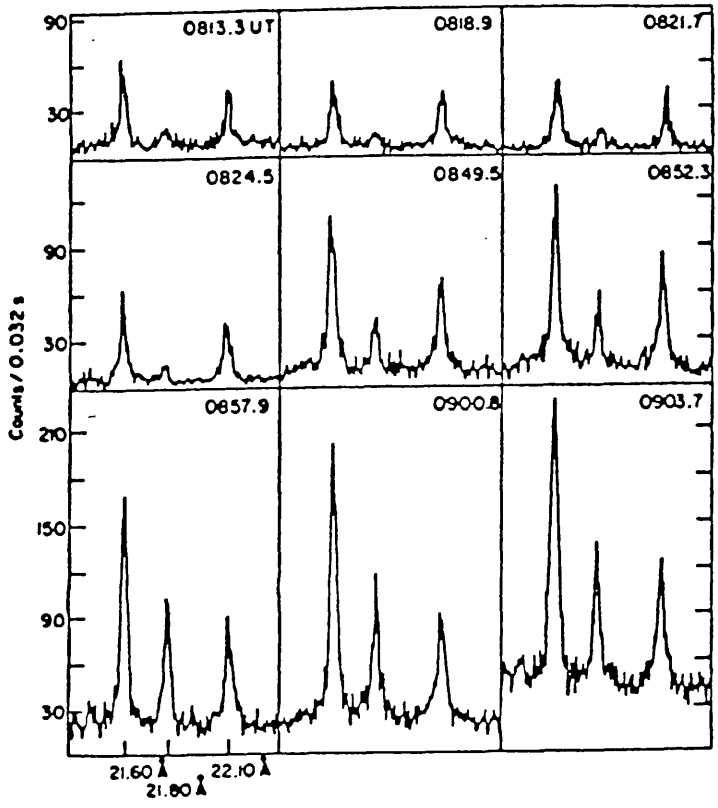

Fig. G.2. The O VII line spectrum near 22Å at various times during the flare 10 June 1979. The different lines at 21.6Å, 21.8Å, and 22.1Å are resonance line, intercombination line and forbidden line respectively (McKenzie 1980).

APPENDIX A

In Chapter 4, we showed that the plasma emitting all observed line ratios must contain substantial density inhomogeneity within them, and that their true mean electron densities are less than the spectroscopic mean densities inferred from one line ratio (cf. Figures 4.3). We proceeded further to discuss how in the case of observed spectroscopic mean density and total emission measure, ξ_{tot}, it is possible to obtain the very useful measure of source inhomogeneity, arising for example due to unstable plasmas. This fact of inhomogeneity is evident in many solar phenomena such as solar flares, and also in laboratory plasmas.

Observations of the inferred values of $<v>$, ξ_{tot} and the total volume V, can be utilised to illustrate this fact explicitly. For the model we adopted, which approximates the distribution of an isothermal plasma in hydrostatic equilibrium, both the normalised emission measure and the spectroscopic mean density can be rewritten as, cf. equations (4.30) and (4.31).

$$\frac{v_0^2(1-\alpha^2)}{2\ln(1/\alpha)} = \frac{\zeta_{\omega}}{n_\alpha^2 V} = \mu \qquad (A.1)$$

and

$$\frac{(\Lambda_\alpha - 1)\,(1-\alpha)\,v_0 + \ln[(1+v_0)/(1+\alpha v_0)] - \Lambda_\alpha^2 \ln[(\Lambda_\alpha + v_0)/(\Lambda_\alpha + \alpha v_0)]}{\Lambda_\alpha \ln[(\Lambda_\alpha + v_0)/(\Lambda_\alpha + \alpha v_0)] - \ln[(1+v_0)/(1+\alpha v_0)]} = <v> \qquad (A.2)$$

It is our aim in this appendix to find the value of the important inhomogeneity parameter, α, employing the above equations. That is, we want to find a solution of (A.1) and (A.2) for v_0 and α for a given observed values of both μ and $<v>$; this was achieved numerically utilising a computer program constructed at Glasgow University 3988 ICL main frame. The program constructed for this purpose is presented, and a description of how it works is given below.

Observationally we obtain the two values, μ and $\langle v \rangle$, which comprise the R.H.S. of (A.1) and (A.2) respectively. we then have two equations in the two unknowns α and v_0. By selecting an arbitrary value of α, lying between zero and one since $\alpha = n_1/n_0$, a value v_0 is determined, from equation (A.1), viz

$$v_0 = \left(\frac{\mu . 2 \ln(1/\alpha)}{(1-\alpha^2)} \right)^{1/2} \qquad (A.3)$$

Utilising this equation, (A.2) becomes a function of α only and can be expressed as follows

$$\Psi(\alpha) \equiv \Phi_{\Lambda_\alpha}(\alpha, \left(\frac{\mu . 2 \ln(1/\alpha)}{(1-\alpha^2)} \right)^{1/2}) = \langle v \rangle \qquad (A.4)$$

in which this equation is a single algebric equation which can be solved by a simple numerical method. For this purpose Newton-Raphson has been adopted in order to get the correct value of α, which in principle can be of the form;

$$\alpha_{i+1} = \alpha_i - \frac{\Psi(\alpha_i) - \langle v \rangle)}{\frac{\Psi(\alpha_i + \frac{\Delta\alpha}{2}) - \Psi(\alpha_i - \frac{\Delta\alpha}{2})}{\Delta\alpha}} \qquad (A.5)$$

This process is carried out automatically in a computer program which for completeness is presented below. This value of $\langle v \rangle$ is plotted against α, for different values of μ, giving the curve shown in Chapter 4, Figs. 4.6.

```
                PROGRAM GAOT6
IMPLICIT DOUBLE PRECISION(A-H,O-Z)
REAL XPLOT,YPLOT
CALL PAPER(1)
CALL PSPACE(.2,.9,.3,.8)
CALL MAP(-.1,2.,-.1,1.)
PRINT*,'LAMBDA'
READ*,D
```

```
9   PRINT*,'INPUT AMTEO'
    READ*,AMTEO
    PRINT*,'1=SCALES;BORDER;ANNOTATION;0=CURVE ONLY'
    READ*,II
    IF(II.EQ.1)CALL BORDER
    IF(II.EQ.1)CALL SCALSI (.4,.2)
    IF(II.LT.1)GOTO 3
    CALL CTRMAG(19)
    CALL CTRFNT (2)
    CALL PLOTNC(1.7,.9,76)
    CALL CTRFNT(0)
    CALL CTRMAG(13)
    IF(D.GT.1)CALL PLOTCS(1.75,.9,'=176')
    IF(D.LT.1)CALL PLOTCS(1.75,.9,'=.115')
    CALL CTRMAG(19)
    CALL CTRFNT (2)
    CALL PLOTNC(.15,.5,109)
    CALL CTRFNT(0)
    CALL CTRMAG(12)
    CALL PLOTCS(.2,.5,'=0.1')
    CALL PLOTCS(.6,.5,'0.5')
    CALL PLOTCS(1.3,.5,'2.0')
    CALL CTRMAG(13)
    IF(D.LT.1)CALL PLOTCS(-.6,-.7,'Fig.7(a)')
    IF(D.GT.1)CALL PLOTCS(-.6,-.7,'Fig.7(b)')
    CALL CTRORI (90.0)
    CALL CTRMAG (19)
    CALL CTRFNT(2)
    CALL PLOTNC(-.4,0.5,97)
    CALL CTRFNT(0)
    CALL CTRORI (0.0)
    CALL CTRMAG(17)
    CALL PLOTCS(0.8,-0.3,'<n>/n')
    CALL SUFFIX
    CALL TYPECS('*')
    CALL NORMAL
3   DO 10 I=1,200
    OBSPMD=(I-1.)**2/40000.*(2-AMTEO**.5)+AMTEO**.5-.001
    AMIN=.001
```

```
      AMAX=.999
5     A=.5*(AMAX+AMIN)
      ANU0=(AMTEO*2.*DLOG(1./A)/(1.-A**2))**.5
      X=DLOG((1.+ANU0)/(1.+A*ANU0))
      Y=DLOG((D+ANU0)/(D+A*ANU0))
      ANU=((D-1.)*(1.-A)*ANU0+X-D**2*Y)/(D*Y-X)
      IF(ANU.GT.OBSPMD) AMIN=A
      IF(ANU.LT.OBSPMD) AMAX=A
      IF((AMAX-AMIN).GT.1D-6)GOTO5
      XPLOT=OBSPMD
      YPLOT=A
      IF(I.EQ.1)CALL POSITN(XPLOT,YPLOT)
      CALL JOIN(XPLOT,YPLOT)
10    CONTINUE
      PRINT*,'NEW AMTEO=6;  EXIT=0'
      READ*,KK
      IF(KK.EQ.6)GOTO9
      CALL GREND
      STOP
      END
```

References

Acton, L.W., Culhane, J. L., Gabriel, A.H., Wolfson, C. J. , Rapley, C. G., Phillips, K.J.H., Antonucci, E., Bentley, R.D., Hayes, R.W., Joki, E.G., Jordan, C., Kayat, M.A., Kent, B., Leibacher, J.W., Nobles, R.A., Parmar, A.N., Strong, K.T., Veck, N.J.: 1981 Astrophys. J.(Lett.) **244**, L137

Aller, L., Ufford, C. W., Van Vleck, J. H.: 1949, Astrophys. J. **109**, 42

Almleaky, Y.M., Brown, J.C., Sweet, P.A. (ABS): 1989, Astron. Astrophys.**224**, 338

Arnaud, M., Rothenflug, R.: 1985, Astron. Astrophys. Suppl. Ser. **60**,425

Athay, G.: 1976, The solar chromosphere and corona: Quiet sun, Boston: Reidel

Behring, W.E, Cohen, L., Feldman, U, Doschek, G.A.: 1976, Astrophys.J. **203**, 521

Behring, W.E, Cohen, L., Feldman, U.:1972, Astrophys.J. **175**, 493

Bely-Dubau, F., Gabriel, G.A., Volunte', S.:1979, Mont. Not. Roy. Astron.Soc.**186**, 405

Bhatia, A.K., Mason,H.E.: 1980, Mont. Not. Roy. Astron. Soc. **190**, 925

Brown, W.A., Mason, H.E., Burnner, M.E., Acton, L.W.: 1986, Astrophys.J. **301**, 981

Burgess, A.: 1964, Astrophys. J. (Lett.) **139**, 776

Burgess, A.: 1965, Astrophys. J. **141**, 1588

Burton,W.M., Ridgeley, A.: 1970, Solar Phys. **14**, 3

Cheng, C.C., Tandberg-Hanssen, E. 1986, Astrophys. J. **309**, 421

Cohen, L., Feldman, U., Doschek, G.A.:1978, Astrophys.J.Supp. **37**, 393

Cook, J.W., Nicolas, K.R.: 1979, Astrophys.J. **229**, 1163

Craig, I.J.D., Brown, J.C.: 1976, Astron. Astrophys. **49**, 239

Craig, I.J.D., Brown, J.C.: 1986, Inverse problems in Astronomy-*A guide to inversion strategies for remotely sensed data*, Adam Hilger; Bristol.

Culhane, J.L., Acton, L.W.: 1974, Annu. Rev. Astron. Astrophys.**12**, 359

Dere, K.P., Mason, H.E.:1981, NASA-Skylab Active Region Workshop Monograph

Dere,K.P., Bartoe, J.-D.F., Brueckner, G.E., Cook, J.W., Socker, D.G.: 1987, Solar Phys. **114**, 223

Dere,K.P., Mason, H.E.,Widing, K.G., Bhatia,A.K.:1979, Astrophys.J.Supp.Ser.**40**, 341

Doschek, G.A., Feldman, U., Cowan, R.D.: 1981, Astrophys. J. **245**, 315

Doschek, G.A., Feldman, U., Dere, K.P.: 1977, Astron. Astrophys.(Lett.) **60**, L11.

Doschek, G.A., Feldman, U., Rosenberg, F.D.: 1977, Astrophys.J.**215**, 329

Doschek, G.A., Feldman, U., VanHosier, M.E., Bartoe, J.-D F.: 1976, Astrophys.J.Supp. **31**, 417

Doschek, G.A., Feldman, U.: 1977, Astron. Astrophys.(Lett.) **58**, L13.

Doschek, G.A., Feldman, U.: 1977, Astrophys.J.(Lett.) **212**, L143.

Doschek, G.A.: 1977, J.Opt.Soc.Am. **67**, 726

Doschek, G.A.: 1984, Astrophys.J.**279**, 452

Doschek, G.A.: 1985, in Autoionisation, edited by A. Temkin (PLenum Press Corp., New York), Chapter 6.

Doschek, G.A.: 1988, in Astrophysical and Laboratory Plasma, edited by R.Brown and J.Lang (33 Scotish Universities Summer School in Physics), 237

Dufton, P.L., Berrington, K.A., Burke, P.G., Kingston, A.E.: 1978, Astron. Astrophys. **62**, 111

Dufton, P.L., Hibbert, A., Kingston, A.E., Doschek, G. A.: 1983, Astrophys. J. **274**, 420

Dupree, A.K.: 1978, Adv. Atom. Molec. Phys. **14**, 393

Durrant, C.J.: 1987, *The Atmosphere of the Sun*, Adam Hilger; Bristol and Philadelphia.

Dwivedi, B.N., Raju, P.K.: 1980, Solar Phys. **68**, 111

Feldman, U., Doschek, G.A., Rosenberg, F. D. : 1977, Astrophys.J. **215**, 652

Feldman, U., Doschek, G.A., Widing, K.G.: 1978, Astrophys.J. **219**, 304

Feldman, U., Doschek, G.A.: 1977, Opt.Soc.Am. **67**, 726

Feldman, U.: 1981, Physica. Scripta **24**, 681

Feldman, U.: 1983, Astrophys.J. **275**, 367

Firth, J.G., Freeman, F.F., Gabriel, A.H., Jones, B.B., Jordan, C., Negus, C.R., Shenton, D. B., Turner, R.F.: 1974, Mont. Not. Roy. Astron. Soc.**166**, 543

Flower, D.R., Nussbaumer, H.: 1975a, Astron. Astrophys. **45**, 145

Flower, D.R., Nussbaumer, H.: 1975b, Astron. Astrophys. **45**, 349

Flower, D.R., Nussbaumer, H.: 1975c, Astron. Astrophys. **42** 265

Flower, D.R.: 1977, Astron. Astrophys.**56**, 451

Gabriel , A.H., Jordan, C.: 1969, Mont. Not. Roy. Astron. Soc. **145**,241

Gabriel , A.H., Jordan, C.: 1972, Case studies in atomic collision physics, vol. 2, North Holland, Amsterdam, p.209

Gabriel , A.H.: 1976, Phil. Trans. Roy. SOc. London **281**, 339

Gabriel, A.H., Mason, H.E.: 1982, 'Applied Atomic Collision Physics', vol.1, eds. H.S.W.Massey, E.W.McDaniel and B. Bederson.

Hanssen, E.T., and Emslie, G.: 1988, The physics of solar flares, Cambridge Univ. Press, Cambridge

Hayes, M., Shine, R.A.: 1987, Astrophys. J. **312**, 943

Hayes, M.: 1982, Mont. Not. Roy. Astron. Soc. **199**, 49

Hayes, M.: 1983, J. Physics. **B16**, 285

Henry, R. J. W.: 1981, Phys. Reports, **68**, 1

Jacobs, V.L., Davis, J., Kepple, P.C., Balaha, M.: 1977a, Astrophys.J. **211**, 605

Jacobs, V.L., Davis, J., Kepple, P.C., Balaha, M.: 1977b, Astrophys.J. **215**, 690

Jacobs, V.L., Davis, J., Rogerson, J. E. , Balaha, M.: 1979, Astrophys.J. **230**, 627

Jacobs.V.L., Davis, J., Robertson, J.E., Balaha, M., Cain, J., Davis, M.: 1980, Astrophys.J. **239**,1119

Jordan, C.: 1969, Mont. Not. Roy. Astron. Soc. **142**,501

Jordan, C.: 1970, Mont. Not. Roy. Astron. Soc. **148**,17

Jordan, C.: 1971, in High lights in Astronomy (C. de Jager, ed.), p.519, D.Reidel, Dordrecht, Holland.

Jordan, C.: 1974, Astron.Astrophys. **34**, 69

Jordan, C.: 1976, Phil. Trans. Roy. SOc. London **281**, 391

Jordan, C.: 1979, in Hanle, W. and Kleinpoppen, H. (eds.), *Progress in atomic spectroscopy*, Plenum, New York.

Kurochka, L. N., Maslennikmova, L. B. : 1975 Soviet Astro. -A J18, 526

Kurochka, L. N.: 1969 Soviet Astro. -AJ **13**, 64

Lambert, D. L. : 1978, Mont. Not. Roy. Astron. Soc. **182**, 249

Lambert, D. L., Luck, R. E. : 1978, Mont. Not. Roy. Astron. Soc. **183**, 79

Loulergue, M., Nussbaumer, H.: 1974, Astron. Astrophys. **34**, 225

Loulergue, M., Nussbaumer, H.: 1976, Astron. Astrophys. **51**, 163

Malinovesky, M.: 1975, Astron. Astrophys. **34**, 101

Mason, H.E., Doschek, G.A., Feldman, U., and Bhatia, A.K.: 1979, Astron.Astrophys. 73, 74

McKenzie, D.L., Broussard, R.M., Landecker, P.B., Rugge, H.R., Young, R.M., Doschek, G.A., Feldman, U.: 1980, Astrophys.J. **238**, L 43

McWhirter, R.W.P., Summers, H.P.: 1984, Applied Atomic Collision Physics **2**, 51

McWhirter, R.W.P.: 1965, Pure and Applied Physics **12**, 201

Munro, R.H, Dupree, A.K., Withbroe, G.L.: 1971, Solar Phys. **19**, 347

Nicolas, K. R, Bartoe, J.-D. F., Brueckner, G. E, Van Hooser, M. E: 1979, Astrophys. J. **233**, 741

Nussbaumer, H., and Storey, P.J.: 1979, Astron.Astrophys. **71**, L5

Nussbaumer, H., Storey, P.J.: 1982, Astron. Astrophys. **115**, 205

Osterbrock, D.E.: 1974, Astrophysics of gaseous Nebulae, Freeman, San Francisco

Pagel, B.E.J.: 1973, Space Sci. Rev. **15**, 1

Patchett, B.E., Harrison, R.A., Sawyer, E.C., Aschenbach, B., Culhane, J.L., Gabriel, A.H., Huber, M.C.E., Jordan, C., Kjeldseth-Moe, O., Mason, H.E., McWhirter, R.W.P., Parkinson, J.H., Poland, A.I., Priest, E.R., Schmitt, J.H.M.M., Thomas, R.J., Timothy, J.G., Tondello, G., Trumper, J.: 1988, in A.I.Poland and V. Domingo (Eds.), The SOHO Mission, ESA SP-1104.

Pottasch, S.R.: 1963, Astrophys. J. **137**, 945

Raju, P.K., Dwivedi, B. N.: 1979, Pramana **13**, 319

Saha, H.P., Trefftz, E.: 1982, Astron.Astrophys. **116**, 224

Sandlin, G.D., Brueckner, G.E., Tousey, R.: 1977, Astrophys.J. **214**, 898

Seaton, M.J.: 1975, Adv. At. Mol. Phys. **11**, 83

Stencel, R.E., Linsky, J.L., Brown, A., Jordan, C., Carpenter, K.J., Wing, R.F., Czyzak, S.: 1981, Mont. Not. Roy. Astron. Soc. **196**,47P

Sturrock, P.A.: 1980, solar flares, Colorado Assoc. Univ. Press, Boulder.

Svesteka, Z.: 1976, Solar Flares, D.reidel, Dorchrecht, Holland

Tanaka, K., Watanabe, T., Nishi, K., Akita, K.: 1982, Astrophys. J.(Lett.) **254**, L59

Tandberg-Hanssen, E, and Emslie, A. G.:1988, The Physics of Solar Flares, Cambridge Univ. Press, Cambridge

Thompson, A.M., Sweet, P.A.: 1988, Preprint

Van Regemorter, H.: 1962, Astrophys. J. **136**, 906

Widing, K.G., Cook, J.W..: 1987, Astrophys. J. **320**, 913

Widing, K.G., Hiei, E.: 1984, Astrophys.J. **281**, 426

Widing, K.G., Spicer, D.S.: 1980, Astrophys. J. **242**, 1243

Widing, K.G.: 1982, Astrophys. J. **258**, 835

Widing, K.G.: 1982, Astrophys. J. **258**, 835

Wilhelm, K., Axford, W.I., Curdt, W., Gabriel, A.H., Grewing, M., Huber, M.C.E., Jordan, S.D., Lemaire, P., Marsch, E., Poland, A.I., Richter, A.K., Thomas, R.J., Timothy, J.G., Vial, J.-C: 1988, in A.I.Poland and V. Domingo (Eds.), The SOHO Mission, ESA SP-1104.

Zirin, H.: 1988, *The Astrophysics of the Sun*, Cambridge University Press, Cambridge.